
Measuring the Tidal Response of Structure Formation using Anisotropic Expanding Cosmological Simulations

Andreas Stefan Schmidt



München 2018

Measuring the Tidal Response of Structure Formation using Anisotropic Expanding Cosmological Simulations

Andreas Stefan Schmidt

Dissertation
an der Fakultät für Physik
der Ludwig–Maximilians–Universität
München

vorgelegt von
Andreas Stefan Schmidt
aus Hof

München, den 19.10.2018

Erstgutachter: Prof. Dr. Simon D.M. White

Zweitgutachter: PD Dr. Klaus Dolag

Tag der mündlichen Prüfung: 26.11.2018

Contents

| | |
|---|-------------|
| Zusammenfassung | xi |
| Abstract | xiii |
| 1 Introduction | 1 |
| 1.1 Theoretical and Computational Physics | 1 |
| 1.1.1 Use in astrophysics | 2 |
| 1.2 Cosmology | 3 |
| 1.2.1 Cosmology equations | 8 |
| 1.2.2 Cosmic microwave background | 10 |
| 1.2.3 Dark matter halos | 13 |
| 1.2.4 Redshift-space distortions | 14 |
| 1.3 N-Body simulations | 15 |
| 1.3.1 Gravitational force calculation | 15 |
| 1.3.2 GADGET4 | 19 |
| 1.4 Purpose of this work | 20 |
| 2 Theoretical background | 23 |
| 2.1 Correlation functions and power spectrum | 23 |
| 2.2 Large-scale tidal field | 25 |
| 2.3 Response function | 30 |
| 2.3.1 Measuring the response function | 32 |
| 2.3.2 Response predictions | 32 |
| 2.4 Halo shapes and alignments | 35 |
| 3 Code modifications | 39 |
| 3.1 Modified particle mesh in GADGET4 | 39 |
| 3.2 Modified tree in GADGET4 | 40 |
| 3.2.1 Elliptical potential | 40 |
| 3.2.2 Elliptical potential approximation - Series expansion | 41 |
| 3.2.3 Force equations | 42 |
| 3.2.4 Tests | 44 |
| 3.3 Modified time stepping | 48 |

| | | |
|----------|--|------------|
| 3.4 | Modified initial conditions | 49 |
| 3.5 | Modified halo finder | 53 |
| 4 | Simulation setup | 59 |
| 4.1 | Initial conditions | 59 |
| 4.2 | Simulation set | 61 |
| 4.2.1 | Convergence PM-only | 61 |
| 4.2.2 | Convergence - TreePM | 64 |
| 4.3 | Halo finding | 68 |
| 5 | Results | 71 |
| 5.1 | PM-only simulations | 71 |
| 5.1.1 | Response Function | 71 |
| 5.2 | TreePM simulations | 75 |
| 5.2.1 | Response function | 75 |
| 5.2.2 | Halo shapes and alignment | 78 |
| A | TreePM Expansion Factors | 91 |
| A.1 | Potential Expansions Factors | 91 |
| B | Supplementary Plots | 93 |
| | Acknowledgments | 102 |

List of Figures

| | | |
|-----|---|----|
| 1.1 | Example of a rotation curve | 6 |
| 1.2 | SDSS Map of the nearby Universe | 7 |
| 1.3 | Expansion of the Universe | 9 |
| 1.4 | The all-sky CMB map from Planck | 11 |
| 1.5 | TT power spectrum from Planck | 12 |
| 1.6 | Visualization of Tree structure | 18 |
| 2.1 | Thin slice of a density field from simulations | 26 |
| 2.2 | Time evolution of anisotropic scale factors | 29 |
| 3.1 | Acceleration Error Projection Image | 45 |
| 3.2 | Acceleration Error Cumulative Sum | 46 |
| 3.3 | Direct Summation acceleration comparison | 47 |
| 3.4 | Response function of the Initial Condition | 51 |
| 3.5 | Response function IC testing | 52 |
| 3.6 | Sample of FoF structure | 54 |
| 3.7 | Density image of most massive halo | 55 |
| 3.8 | Sample of FoF and SUBFIND structure | 56 |
| 3.9 | Subhalo mass function comparison | 58 |
| 4.1 | PM convergence - one-dimensional powerspectrum | 62 |
| 4.2 | PM convergence - response function | 63 |
| 4.3 | Parameter comparison | 65 |
| 4.4 | Power spectrum comparison with Millennium | 67 |
| 4.5 | Comparison between mass resolutions | 69 |
| 5.1 | Comparison of the one-dimensional power spectrum with and without tidal field | 72 |
| 5.2 | Response function PM-only | 73 |
| 5.3 | Response function - Time evolution | 75 |
| 5.4 | Response function - TreePM | 77 |
| 5.5 | Subhalo Massfunction | 79 |
| 5.6 | Reduced inertia tensor ratio | 81 |
| 5.7 | Axes ratio $\log(M_{\text{sub}}/M_{\odot}) \geq 12.57$ | 82 |

| | | |
|------|--|----|
| 5.8 | Median axis ratio | 83 |
| 5.9 | Angle distribution for four mass bins | 84 |
| 5.10 | Mean of the alignment angles | 85 |
| 5.11 | Median angle for all axes | 86 |
| 5.12 | Probability density function of the x/z - cosine | 87 |
| B.1 | Cumulative distribution of $\cos(\Theta)$ additional mass bins | 94 |
| B.2 | Difference for the cumulative distribution of $\cos(\Theta)$ | 95 |

List of Tables

| | | |
|-----|---|----|
| 4.1 | Initial Conditions - Basic Properties | 60 |
| 4.2 | Cosmological parameters | 60 |
| 4.3 | Simulation parameters | 61 |
| 4.4 | TreePM convergence runs | 64 |
| 4.5 | Halonumbers | 68 |

Zusammenfassung

In dieser Arbeit untersuchen wir den Einfluss eines großskaligen Gezeitenfeld auf die Entstehung von Strukturen im Universum. Hierzu führen wir N-Body Simulationen in einem „seperatem Universum“ aus, welches ein großskaliges Gezeitenfeld enthält, was zu einer anisotropen Ausdehnung führt. Zuerst modifizieren wir den *particle mesh* (PM) Poisson-Solver des kosmologischen Simulations Codes GADGET4. Mit diesem Code simulieren wir die Entwicklung von 16 Realisierungen des anfänglichen Dichtefeldes mit und ohne Gezeitenfeld. Diese werden dann dazu genutzt um die *Responsefunktion* zu messen, welche parametrisiert wie das Gezeitenfeld die Strukturentwicklung im linearen und nicht linearen Bereich beeinflusst. Zusammen mit der Response auf großskalige Überdichten wird das nicht lineare Bispektrum im squeeze limit komplett beschrieben. Im Gegensatz zur Funktion für die Überdichten finden wir, dass die Response für das Gezeitenfeld bei $z = 0$ den theoretischen Wert der Störungsrechnung auf großen Skalen selbst im nicht linearen Bereich nicht überschreitet. Bei höhere Rotverschiebungen werden Artefakte aus den Anfangsbedingungen sichtbar, jedoch scheint die Funktion immer noch den theoretischen Wert nicht zu übersteigen. Um mit unseren Messungen zu vergleichen haben wir ein einfaches Halo-Modell entwickelt, welches den Einfluss des Gezeitenfeldes in Betracht zieht.

Der erste Simulationssatz nutzt unmodifizierte Anfangsbedingungen. Nachdem dies der Grund für Artefakte sein kann entwickeln wir ein Schema, welches das großskalige Gezeitenfeld berücksichtigt. Dieses benutzt lagrangesche Störungstheorie zweiter Ordnung (2LPT) und reproduziert die korrekte Responsefunktion zu jeder Rotverschiebung. Um den Einfluss des Gezeitenfeldes auch auf kleineren Skalen zu messen und die Abweichung des Halomodells zu ergründen, verändern wir den “Tree” in GADGET4.

Mit Hilfe der vollen TreePM Kraftberechnung simulieren wir acht Realisierungen, welche mit dem veränderten 2LPT Code erzeugt werden. In diesen Simulationen messen wir die Responsefunktion G_K bis auf Skalen von $k \leq 20h \text{ Mpc}^{-1}$. Weiterhin bestimmen wir die eulerische Response R_K in diesem Bereich. Mit der höheren Kraftauflösung sind wir in der Lage den Effekt auf dunkle Materie Halos zu untersuchen. Mit einem modifizierten Friends-of-Friends (FoF) und SUBFIND Algorithmus erzeugen wir Halo und Subhalo Kataloge. Dies erlaubt es uns die Intrinsic-Alignment-Amplitude A für das großskalige Gezeitenfeld zu messen, welche eine Kontamination für schwache Gravitationslinsen Durchmusterungen darstellt. Ebenfalls betrachten wir die Form der Halos, sowie deren Ausrichtung mit Bezug

auf die Achsen des Gezeitenfeldes. Hier finden wir lediglich einen schwachen Einfluss auf die Form der Halos, allerdings ein klares Signal das sich die Halos nach dem Gezeitenfeld ausrichten. Dieses Signal zeigt eine leichte Abhängigkeit von der Halomasse, sodass sich massivere Halos mehr zu den Achsen des Gezeitenfeldes ausrichten.

Abstract

In this thesis we investigate the influence of a large-scale tidal field on the formation of structure in the Universe. For this we run N-Body simulations in a “separate universe” which includes a large-scale tidal field that leads to an anisotropic expansion of the background. First we modify the *particle-mesh* (PM) poisson solver of the cosmological simulation code GADGET4. Using this modified code we simulate the evolution of 16 realizations of an initial density field with and without a large-scale tidal field. These are used to measure the *response function* which parameterises how the tidal field influences structure formation in the linear and nonlinear regime. Together with the response to a large-scale overdensity, this completely describes the nonlinear matter bispectrum in the squeezed limit. We find that, contrary to the density response, the tidal response does not exceed the large-scale perturbation-theory prediction even on nonlinear scales at $z = 0$. For higher redshifts it still seems to stay below the linear prediction but possible artifacts from the initial conditions become visible. We develop a simple halo model that takes into account the effect of the tidal field and compare it with our direct measurement from the anisotropic N-body simulations.

Our first set of simulations uses unmodified first-order initial conditions. Since this might be the cause of artifacts, we develop a corrected scheme for initial conditions with a large-scale tidal field. These use second-order Lagrangian perturbation theory (2LPT) and reproduce the correct response function at any redshift. To expand the response measurements to smaller scales and to investigate the difference with the halo model, we modify the “Tree” in GADGET4 for the anisotropic expansion factor.

Using the full TreePM force calculation we run eight different realizations, generated using the modified 2LPT code. From these simulations we obtain the growth-only response function G_K up to scales of $k \leq 20h \text{ Mpc}^{-1}$ as well as the Eulerian response function R_K . With the higher force resolution we are able to investigate the effect of the large-scale tidal field on dark matter halos. We compute the halo and subhalo catalogs with an adjusted Friends-of-Friends (FoF) and SUBFIND algorithm. With this we can measure the intrinsic alignment amplitude A for our large-scale tidal field which is an important contamination in weak lensing surveys. Further we compare the shapes of halos and their alignment with respect to the tidal field. While we only find a very small effect on the shapes, the halos are clearly aligned with the tidal field. This alignment shows a slight dependency on halo mass where the alignment seems stronger for more massive halos.

*"I may not have gone where I intended to go,
but I think I have ended up where I intended to be."*
Douglas Adams

Chapter 1

Introduction

In this thesis we want to investigate the effect of a large-scale tidal field on the largest structure in the Universe. For this we use N-body simulations with and without a large-scale tidal field. These were used to measure the change in power spectra and the difference in the shape and alignment of dark matter halos. For this we want to give a short introduction to the most important subjects the thesis relies on. In the first section we give a brief general introduction with some historical milestones for computational physics, while we also list reasons for the use in astrophysics. The used cosmology and ways to measure the corresponding parameters are described in the second section (section 1.2) which also includes a subsection about dark matter halos (section 1.2.3). In the section about cosmology we also describe a short history of our Universe in the current model. Since we use N-body simulations in this work, a short introduction to these kind of codes is given in section 1.3 where the first part describes the different ways to compute gravity, and the second part is specific to the code used in this thesis. The last section (section 1.4) describes the purpose of this work and shows the different possible applications.

1.1 Theoretical and computational physics - A short introduction

In our quest for knowledge about the Universe and its evolution we rely on two or three pillars, depending on the definition. Observations of the universe in the electromagnetic spectrum and gravitational waves are the first of those. These provide data which are then compared with the second pillar, theoretical work and simulations which can be seen as the third pillar. All three parts together allow us to get an understanding of the evolution and composition of the universe. Although observations are essential, this work focuses on simulations and theoretical work. Specifically observations are discussed solely in the context of their ability to support or falsify a theory. Generally, all theories have to propose ways to falsify themselves.

A famous example for this is general relativity a purely theoretical work which is un-

dergoing numerous experiments and observations in order to probe its validity. One of the more interesting experiments was done during a solar eclipse in 1919 and repeated in 1922. During the eclipse the position of stars, which were close to the sun at the time, were observed from Brazil and at the west coast of Africa (1919) and in California (1922). The apparent positions of the stars changed as the light passed through the gravitational field of the sun and was bent according to the equations of general relativity. This effect is known as gravitational lensing and can also be observed in some galaxy clusters where it is used to determine the total mass of the lensing system.

Beginning in the 1940's the first computers were used to simulate physical processes starting with ballistic and nuclear explosion simulations in Los Alamos. The first Monte-Carlo and hydrodynamical simulations were also performed there. Later, the equation-of-state calculation was carried out using computer systems, and again a bit later they were used to investigate the 3-body problem. In addition they allowed the formulation of the gravity assist method which was later used, for example, to accelerate the Voyager probes such that they could leave our solar system. This method is now commonly used for probes that head towards the outer or inner most parts of our solar system to save fuel and weight. The use of computers also led to a better understanding regarding the four fundamental forces and their interconnection (with the exception of gravity which cannot yet be connected to the other fundamental forces), for example, by giving insight in the renormalization of the Electroweak theory. In the 1980's, the fast multipole method (see also Section 1.3.1) was developed by Rokhlin (1985), which is the backbone to compute long-range forces in modern N-Body codes. Ever since, the computational power increased, which has made the computer an essential tool in physics and astrophysics for the complex problems that arise.

1.1.1 Use in astrophysics

One of the main problems in astrophysics is the long time scale on which changes occur¹. Observations only show snapshots and the assumption has to be made that a series of "unconnected" observations of independent systems show an evolution with time. To ease this problem, simulations are used which rely on approximations of physical processes. An "famous" result, that is supported purely by N-body simulations, is the finding that dark matter halos can be described by a universal density profile with only two free parameters. We will describe this profile with a bit more detail later on in section 1.2.3.

While pure N-Body simulations help understanding the collisionless components of the Universe, like dark matter, the next step to further understand the evolution of our Universe is to include the gas component that leads to galaxies. We know that gas can be treated as fluid and the same techniques can be used as in standard hydrodynamic codes. For these,

¹There are some exceptions to this, such as parts of solar physics or supernova explosions.

subgrid models have to be used to represent physical processes, that cannot be resolved, since the range of scales involved is enormous, spanning multiple orders of magnitude. To simulate from first principles one would start at least on the atomic level ($\sim 10^{-10}\text{m}$) while the length scale of interest in the simulations can be of the order of hundreds of Megaparsecs ($\text{Mpc} \approx 3.1 \cdot 10^{22}\text{m}$) in cosmological runs or a few hundred kiloparsecs ($\text{kpc} \approx 3.1 \cdot 10^{19}\text{m}$) in isolated galaxy simulations. This is with the current codes and technology, not feasible even with the largest supercomputers to date. To circumvent this, most processes below a certain scale are approximated by empirical or physically motivated models that are valid at and above (to a certain extent) the resolution limit. One of the prominent examples for this is star formation, which is mostly stochastic and depends on the mean density and temperature of the resolution element. This effectively mirrors the observed Schmidt relation (Schmidt, 1959). The mass of the star is then drawn according to the mass function. Stellar feedback is also modeled as heating the surroundings depending on the mass of the star but for the bulk of models only contains supernova explosions. Another energy source in galaxies is the central black hole which is modeled as a sink particle that accretes surrounding gas and grows while also heating the medium (e.g. Springel et al., 2005a). In the recent years the models have grown more complicated to incorporate different physical processes like shielding through dust, kinematic feedback from black holes, metal enrichment and so on.

In many cases different models are able to reproduce the same observations which leaves the problem that we can not find a unique model that works but are left with a variety of them. This limits the gain of knowledge for the influence of processes that are below the resolution and one should be careful when interpreting simulation data. For example, this can be seen by comparing the Illustris (Vogelsberger et al., 2014) and EAGLE (Schaye et al., 2015) simulations which differ both in the hydro-dynamical solver used and in some subgrid models most notably the black hole feedback model. Yet both are successful in reproducing observables and can therefore be used to study certain aspects of galaxy evolution.

1.2 Cosmology

Following this brief introduction, we describe the central points of the cosmological model used throughout this work. As of the writing of this thesis, the model which is accepted by most researchers is the flat Lambda Cold Dark Matter (ΛCDM) model. The first evidence for an expanding universe was given by Hubble (1929) measuring the distance D to nebulae (galaxies) using pulsating stars called Cepheids and their velocity v , or more precisely their redshift $z \equiv \delta\lambda/\lambda$ defined as change of observed wavelength $\delta\lambda$ divided by the wavelength λ in the reference system. He found that more distant objects appear to have higher redshifts which translate to higher velocities away from the observer. From these observations he derived the now famous Hubble law:

$$v = H_0 D, \quad (1.1)$$

with a constant H_0 .

Going to higher distances, Cepheids are no longer bright enough, and other standard candles, whose brightness is known, have to be used. One of the brightest events in the universe are supernovae, the violent deaths of stars. These can outshine their host galaxies and are visible over vast distances. For our purpose there are two classes of Supernovae, namely Type II and Ia. Those can be refined further depending on their spectrum. While Type II supernovae are the end stage of a massive star that was recently on the main sequence of hydrogen burning, the Type Ia are nuclear explosions coming from a carbon oxygen white dwarf (the remnant of a star) that was accreting mass from a companion until it reached the critical mass of $\sim 1.4 M_\odot$. Since this is a specific mass, the brightness at a fixed distance to the star should be exactly the same for all explosions within a minor error margin. This can then be used to estimate the distance to the star or more importantly, its host galaxy. A good reference on how to estimate distances using Supernovae is Perlmutter & Schmidt (2003) and we will only touch on the subject. To get an accurate measurement one has to calibrate their observational equipment which might introduce some uncertainties. Furthermore there are two possible scenarios for a supernova Type Ia which depends on the companion star. If the companion is a main sequence star (single degenerate progenitors), accretion will increase the mass of the white dwarf until it reaches the critical mass and the explosion has the expected energy. However, if the second star is also a compact object, namely another white dwarf, then the supernova will happen as result of a merger event of the two stars (double degenerate progenitors). The mass of both white dwarfs does not necessarily add up to the critical mass but can be up to slightly below twice that. This then changes the amount of energy available and therefore the brightness of the supernova rendering the peak brightness useless for measuring the distance. A workaround for this is not to use the peak alone, but to include the decline of the light-curve. Calculating the ratio between the brightness of the peak and at a given time, say 15 days after maximum, can then be used to renormalize to the standard candle value (Pskovskii, 1977; Phillips, 1993). Using these supernovae two recent projects showed the accelerated expansion of the Universe (Riess et al., 1998; Perlmutter et al., 1999) and were awarded with the Nobel Prize in physics. The dark energy driven accelerated expansion is a key component of the cosmological model and measuring the velocity as function of distance allows us to measure it.

As the name Λ CDM suggests, dark matter is another important ingredient in the model. The first hint of matter that does not interact with electro-magnetic radiation was given by Fritz Zwicky through observations of the Coma cluster (Zwicky, 1933, 1937). The velocities measured in the cluster did not match the expected velocities derived from the visible matter. Therefore he concluded that there had to be a form of dark matter that is not visible in the optical spectrum. Part of this matter is hot gas that can be observed in X-ray, but the hot gas component alone does not fully explain the high velocities that are observed in the cluster. A similar experiment can be done for our own Galaxy, the Milky Way. Measuring the rotational speed of gas clouds using the 21cm line of hydrogen, stars, and globular clusters allows for a measurement of the mass that is enclosed in the given radius. A typical

rotation curve is shown in Figure 1.1 which was made by Matthew Newby for the Milkyway@home webpage (<https://milkyway.cs.rpi.edu/milkyway/science.php>). These and other observations shaped the picture of an expanding universe including a dark component that dominates over the normal matter.

The recent measurements of the Planck satellite support this model with precise measurement of the Cosmic Microwave Background (CMB) Radiation (Planck Collaboration et al., 2015), but also highlight some tension for the parameters used to describe the model. The largest discrepancy, which might hint to yet unknown physics, is found in the Hubble parameter (H) (Riess et al., 2016; Mörtsell & Dhawan, 2018). Using Bayesian hierarchical models, Feeney et al. (2018) try to alleviate this tension, arguing that standard Gaussian least square approximations are not working for this dataset. This still favors the Λ CDM cosmology even though it only included Supernova and CMB data. The tension over H mainly arises between distance estimates derived from Supernova Type Ia (Riess et al., 1998; Perlmutter et al., 1999) and the Planck data.

Another way to infer the Hubble parameter and angular diameter distance is to measure the baryon acoustic oscillations (BAO) which are the remnants of sound waves in the primordial plasma before the photons decoupled from the matter. During that time the plasma behaved like a nearly perfect fluid and was governed by sound physics. Therefore, we can calculate the harmonic peaks that will be reflected in the power spectrum of the cosmic microwave background (CMB; see also Section 1.2.2). Due to the interaction between the gravitational pull and the photon pressure at the position of every anisotropy, oscillations are introduced that can be described as sound waves. The size of the sound horizon is given by

$$s = \int c_s dt, \quad (1.2)$$

where $c_s = \dot{p}_\gamma / \dot{\rho}_\gamma$ is the adiabatic sound speed. This scale “freezes” at the surface of last scattering, the origin of the CMB, and then only increases at the rate of the expansion of the universe. Hence the size of the BAO feature at a smaller redshift can be used to measure the expansion of the universe. The size of BAO’s can be measured using the correlation function which, simply put, counts neighbours at a given distance. Due to the nature of galaxy formation, which happens mostly in dense knots, and is therefore clumpy, there is a high correlation on small separations while the correlation decreases gradually with distance to nearly no correlation of the largest scales. The signal of the BAO is a bump in the correlation function at the sound horizon scale as there is an increased number of tracers.. This signal is found in large surveys, e.g the Sloan Digital Sky Survey (Eisenstein et al., 2005, SDSS), which found a sound horizon of ~ 150 Mpc for the universe today. SDSS is one of the most prominent and successful galaxy surveys to date and showed the filamentary structure in the galaxy distribution on large scales and how it changed along the time axes. One map obtained by SDSS is shown in Figure 1.2 which represents the galaxy distribution in the nearby Universe.

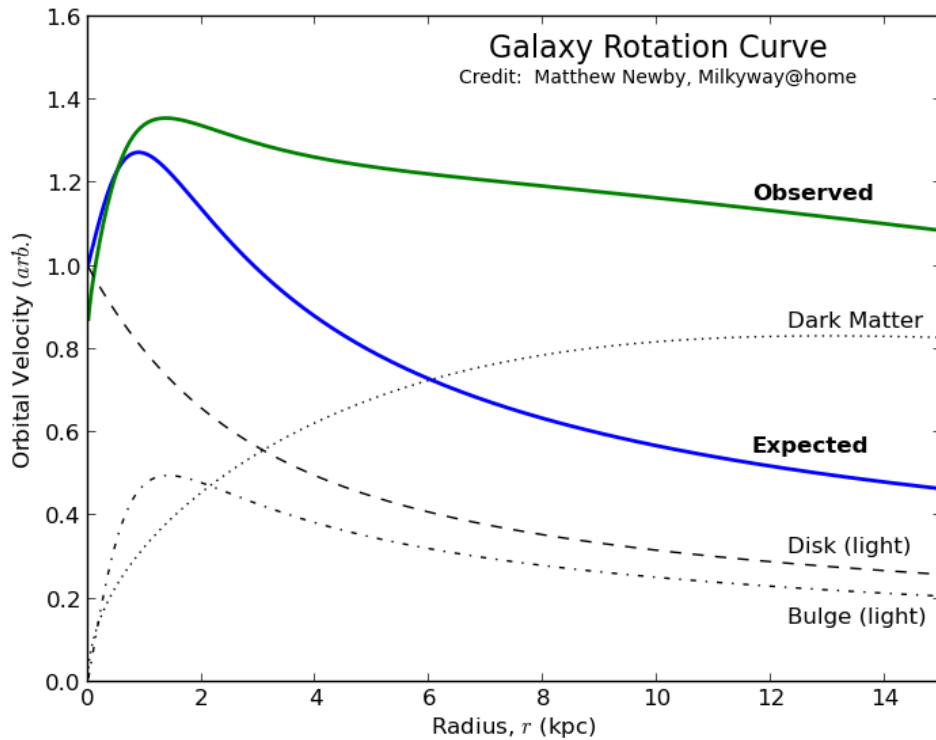


Figure 1.1: Rotation curves that are expected for the disk and bulge component (black dashed and dashed dotted lines), as well as the combination of both (blue line). The green line shows the observed rotation curve which is flat in the outer regions. The difference in expected and observed rotation curve suggests an additional component that becomes dominant in the outer regions of a galaxy. This part is shown as dotted line, which shows the expected function for the dark matter. The image is taken from <https://milkyway.cs.rpi.edu/milkyway/science.php> (13.06.2018) and was made by Matthew Newby, Milkyway@home.

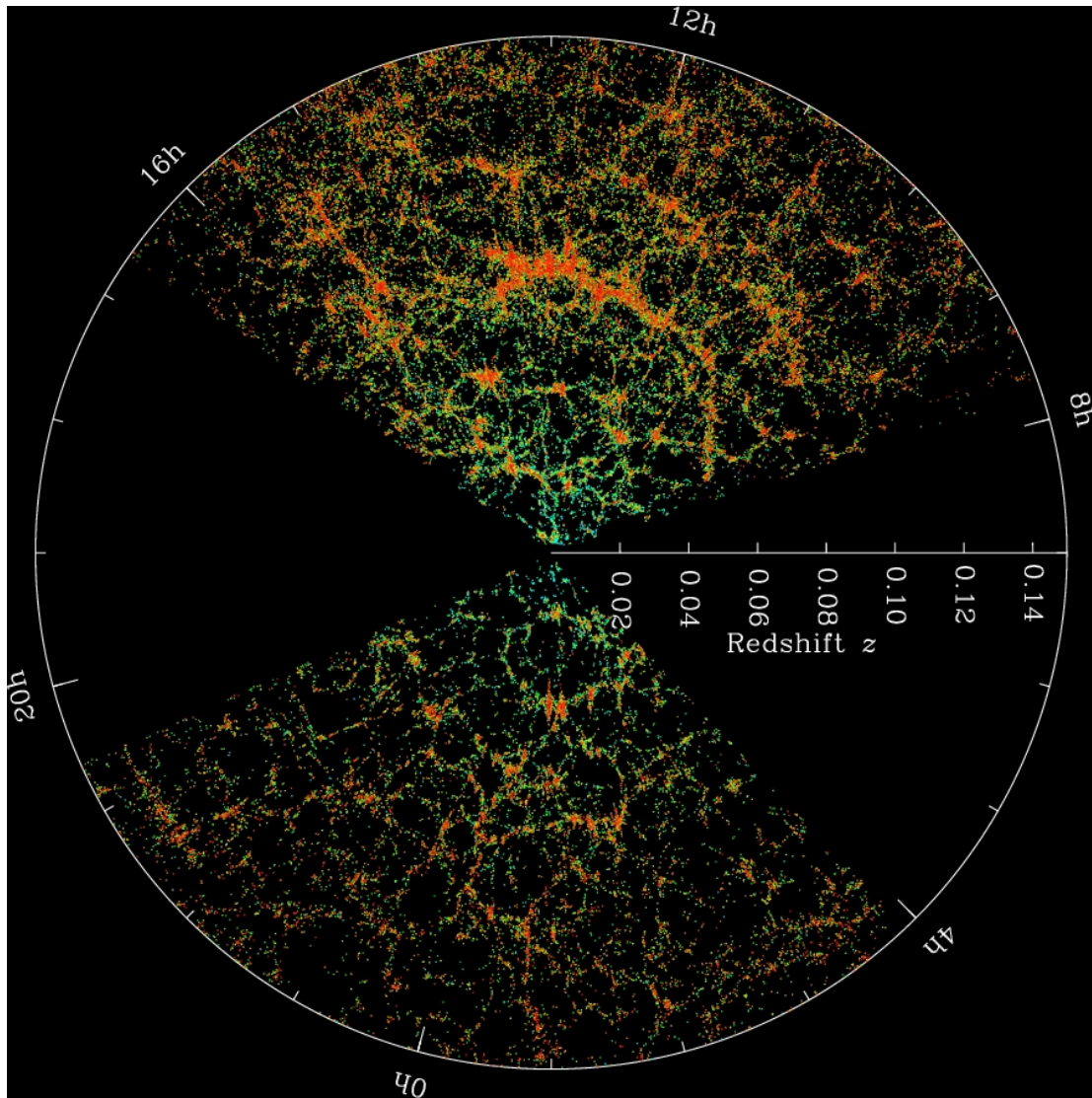


Figure 1.2: The galaxy distribution for the nearby Universe from SDSS. The color represents the g-r band color of the galaxy. Image Credit: M. Blanton and SDSS, <https://www.sdss.org/science/orangepie/>, 03.09.2018

Short History of the Universe We will now take a short turn and review the history of the expansion and the different stages of the Universe. Figure 1.3 shows a schematic view of the expansion history of our Universe in the currently accepted cosmological model (flat Λ CDM) with time running from left to right and height depicting the size of the Universe. Far left, we start with the Big Bang, followed shortly by the inflation phase, where the universe expands exponentially. This phase blew quantum fluctuations up to macroscopic anisotropies that will work as seeds for structure formation. From shortly after inflation until $z \sim 3600$ the Universe was dominated by the radiation density. At $z \sim 1100$ the Universe cooled enough that protons and electrons could combine to neutral atoms allowing the photons to decouple from the baryons and escape. This results in the surface of last scattering, which can be observed today in the microwave wavelength regime (CMB). From a short time before that, the dark matter was able to decouple from the plasma and the small perturbations introduced by quantum dynamical effects which had a higher density grew by attracting the matter. This then later acts as a trough for the baryonic component which eventually formed stars and galaxies. After the last scattering surface, the dark ages began where the medium was neutral and almost no visible light existed. The universe further cooled, and around $z \sim 11$ the first stars and galaxies form, which led to an increase in UV photons that start to ionize the surrounding medium. This marks the beginning of the epoch of reionization, which lasts until $z \sim 6$ where the full Universe again got ionized (Becker et al., 2001). The difference to the earlier epoch however is the density of the Universe, which is now low enough so that scattering events between matter and photons are rare, leaving the Universe transparent. At around $z \sim 0.5$, the dark energy density became dominant and the Universe entered into an accelerated expansion phase.

1.2.1 Cosmology equations

To understand how the measurements of the CMB radiation or Supernova light-curves allow us to estimate the cosmological model, we need the equations that are describing the Universe in our current theory. Those equations are the field equations from Einstein's general relativity (GR): (Einstein, 1915, 1917)

$$R_{\mu\nu} - \frac{1}{2}Rg_{\mu\nu} + \Lambda g_{\mu\nu} = 8\pi GT_{\mu\nu}, \quad (1.3)$$

with the Ricci tensor $R_{\mu\nu}$, curvature scalar R , cosmological constant Λ , the gravitational Constant G , the energy-momentum tensor $T_{\mu\nu}$ and the space-time metric $g_{\mu\nu}$.

Friedmann found in 1922 that the steady state solution from Einstein for a non-empty Universe, was not stable (Friedmann, 1922). The full set of equations describing the dynamics of the Universe were presented by Friedmann in 1924 and Lemaître in 1927 (Friedmann, 1924; Lemaître, 1927). In GR, gravity is described by a space-time metric $g_{\mu\nu}$ with indices running over the time and space coordinates. The Friedmann equations assume a homogeneous and isotropic universe, which is called the cosmological principle and holds on large scales. We start with the Friedmann-Lemaître-Robertson-Walker (FLRW) metric

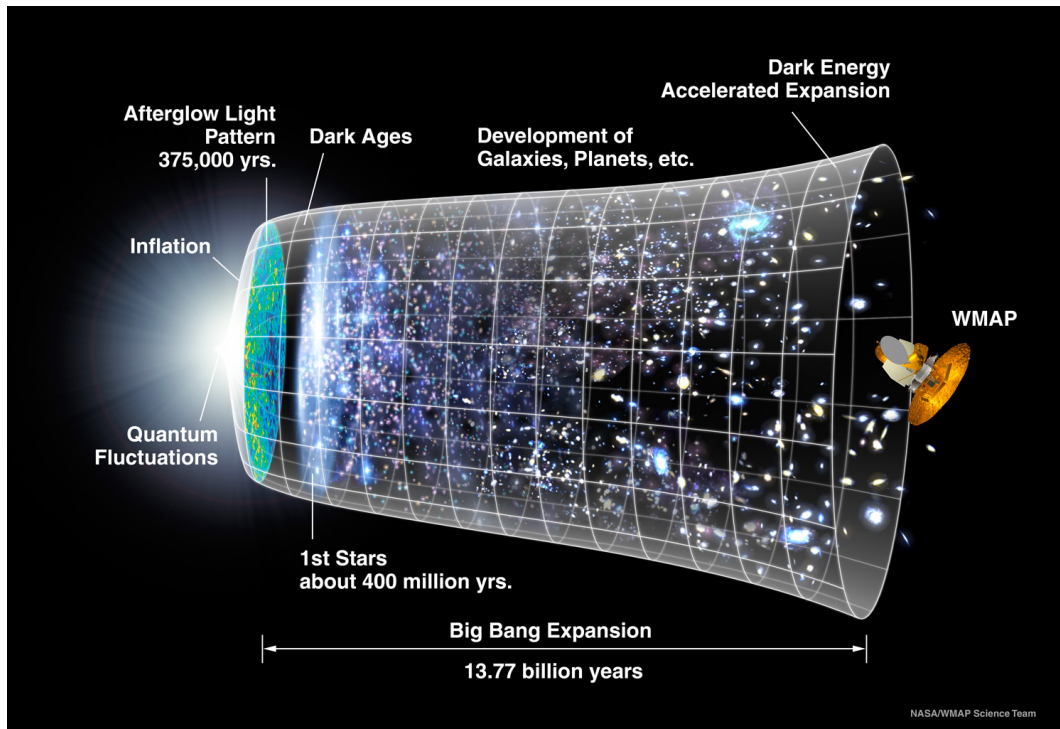


Figure 1.3: A schematic view of the expansion of the universe from the Big Bang (left) to today (right) with the height depicting the size (created by NASA/WMAP Science Team published 21.12.2012). During inflation the universe expanded exponentially, which also increased the size of quantum fluctuations which are the seeds for structure later on. The universe expanded and cooled down allowing protons and electrons to combine into neutral atoms which then allowed photons to escape. This is known as the decoupling at $z \sim 1100$ (375000yrs after the Big Bang). Subsequently the universe entered the dark ages where most of the universe was neutral. After roughly 400 million years, the first stars and galaxies form and the photons produced by them start ionizing the surrounding medium marking the beginning of the epoch of reionization ($z \sim 11$) which ends roughly around $z \sim 6$. Around $z \sim 0.5$ the universe became dominated by dark energy which begins accelerating the expansion.

$$c^2 d\tau^2 = c^2 dt^2 - a^2(t) \left[\frac{dr^2}{1 - kr^2} + r^2 d\theta^2 + r^2 \sin^2(\theta) d\phi^2 \right], \quad (1.4)$$

with the four coordinates t, r, θ, ϕ ; $a(t)$ being the scale factor; $k \in [-1, 1]$ describing the curvature and $d\tau$ the infinitesimal line element. Using the cosmological principle, we can find an analytic simplification of the Einstein field equations equation (1.3):

$$\left(\frac{\dot{a}}{a} \right)^2 = \frac{8\pi G\rho}{3} - \frac{k}{a^2} + \frac{\Lambda}{3}, \quad (1.5)$$

$$\frac{\ddot{a}}{a} = -\frac{4\pi G}{3}(\rho + 3p) + \frac{\Lambda}{3}, \quad (1.6)$$

which are called the Friedmann equations, a set of coupled differential equations. More commonly the Friedmann equations are written using the density parameters Ω_i defined as

$$\Omega_i = \frac{\rho_i}{\rho_{crit}} = \frac{\rho_i}{\frac{3H^2}{8\pi G}} = \frac{8\pi G\rho}{3H^2}, \quad (1.7)$$

with the critical density ρ_{crit} , the density following from equation (1.5) for which the universe without cosmological constant ($\Lambda = 0$) has no curvature ($k = 0$), and the Hubble parameter $H = \dot{a}/a$ with which we can rewrite equation (1.5) as

$$\frac{H^2}{H_0^2} = \Omega_{r,0} a^{-4} + \Omega_{m,0} a^{-3} + \Omega_{k,0} a^{-2} + \Omega_{\Lambda,0}, \quad (1.8)$$

where the subscript 0 denotes the present day value, Ω_r , Ω_m , Ω_k and Ω_Λ are the density parameters for radiation, matter, curvature and the cosmological constant, respectively. One easy solution to this is found for setting $\Omega_\Lambda = 0$ and $\Omega_m = 1$ which describes the Einstein-deSitter universe (Einstein & de Sitter, 1932).

1.2.2 Cosmic microwave background

The measurements of the cosmic microwave background (CMB) radiation using the Planck satellite allow for the computation of a variety of parameters describing our Universe including those used in the Friedmann equations equations (1.5)–(1.6). The CMB is the image of the young universe, roughly 375000 years after the Big Bang and marks the furthest look-back time in the electromagnetic spectrum. At this time the density and temperature of the Universe dropped enough, so that the mean free path of the photons increased and electrons and protons combined to neutral atoms. This allowed the photons to escape the plasma and these are the photons we see today as CMB. The structure seen in the CMB represents the density field at the time of (re-)combination, which was sourced by quantum fluctuations, which were blown up and frozen during the time of inflation. These small anisotropies are the seeds for the structure that, at a later time, emerged. The temperature map of the CMB in Figure 1.4 shows the difference to the mean as measured

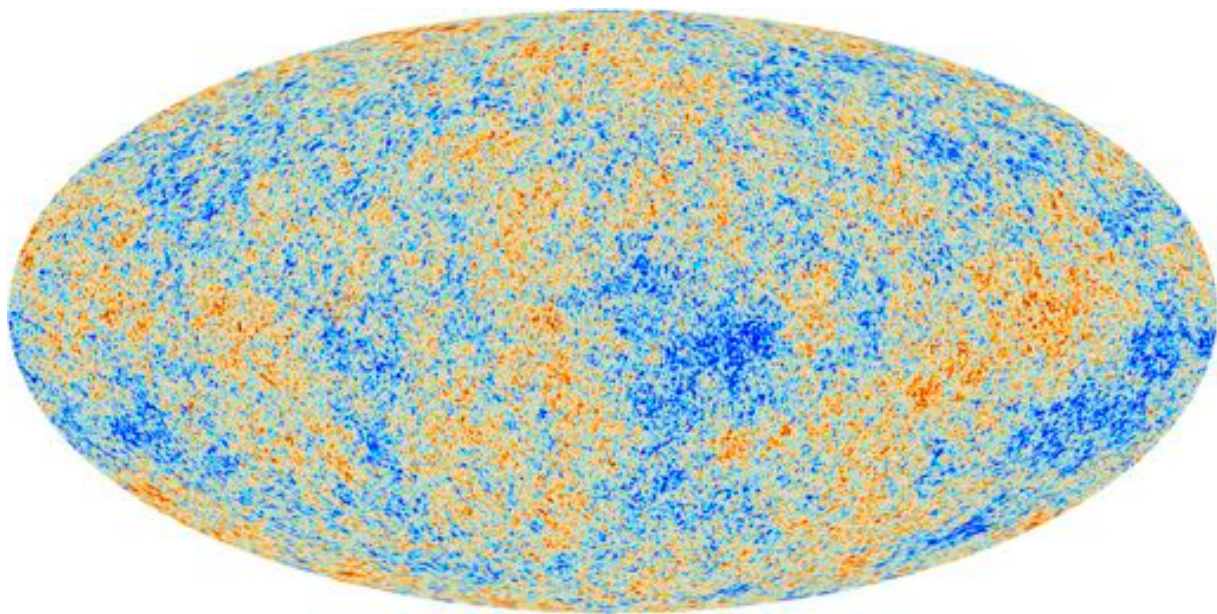


Figure 1.4: All-sky map as seen by the Planck satellite showing the temperature difference from the mean of the cosmic microwave background. Small anisotropies can be seen in the temperature that represent tiny fluctuations in the density. Copyright: ESA, Planck Collaboration, taken from https://www.esa.int/spaceinimages/Images/2013/03/Planck_CMB (13.06.2018)

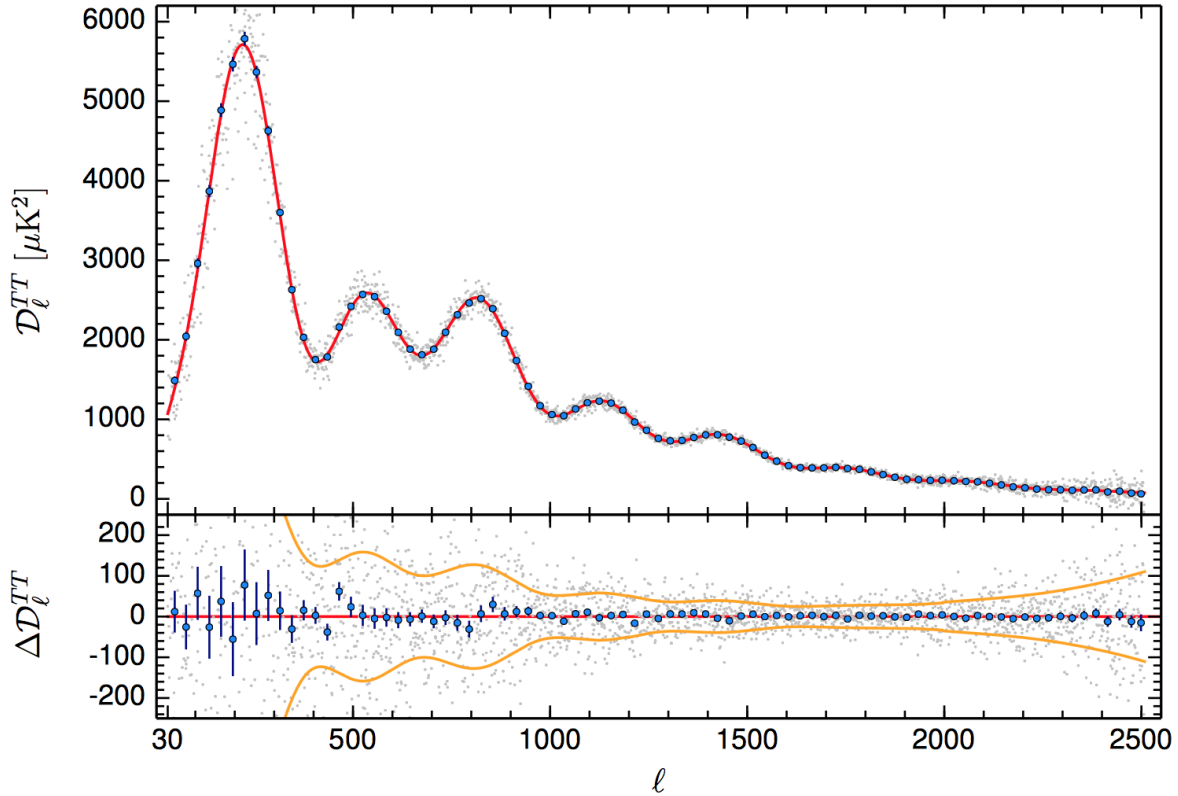


Figure 1.5: The temperature temperature power spectrum D_l^{TT} from the Planck observations taken from Planck Collaboration et al. (2016). Blue points represent binned data with a bin size of $\Delta l = 30$. The grey points are the unbinned data and the red line is the theoretical ΛCDM fit to the data. The y axis is defined as $D_l^{TT} = (l(l+1)/(2\pi))C_l$. The lower panel shows the residuals with respect to the best ΛCDM fit from the Planck data. The 68% errorbar for the unbinned data is shown as yellow line.

by the Planck satellite and pictures the small fluctuations in the very early Universe. To extract the cosmological parameters from the CMB, the main approach is to use the angle averaged power spectrum C_l . For this the data is transformed using spherical harmonics Y_{lm} as:

$$T(\hat{n}) = \sum_{l=0}^{l_{max}} \sum_{m=-l}^l a_{lm} Y_{lm}(\hat{n}), \quad (1.9)$$

where $T(\hat{n})$ is an arbitrary function defined on a sphere and the coefficients a_{lm} are given by the integral of the function with the complex conjugate of Y_{lm} :

$$a_{lm} = \int_{4\pi} T(\hat{n}) Y_{lm}^*(\hat{n}) d\Omega. \quad (1.10)$$

The angle averaged power spectrum is then obtained by the average over m for each wave length l

$$C_l = \frac{1}{2l+1} \sum_{m=-l}^l |a_{lm}|^2. \quad (1.11)$$

There remains a slight problem as the physics is given by the ensemble average $\hat{C}_l = \langle C_l \rangle_{ensemble}$ while we can only observe a single realization C_l . This introduces a wavelength dependent error in the measurement, called cosmic variance

$$\Delta \hat{C}_l = \sqrt{\frac{2}{2l+1}} \hat{C}_l. \quad (1.12)$$

The most recent temperature-temperature (TT) power spectrum of the CMB from Planck Collaboration et al. (2016) is shown in Figure 1.5.

From the peaks in Figure 1.5, we can infer that there are oscillations in the early universe. These are caused by gravity pulling and radiation pressure pushing the matter. The peaks are the different modes at the extrema of the oscillations forming a harmonic series which depends on the distance sound can travel (the sound horizon) at the time of the CMB emission. The position of the peaks depends mainly on the curvature and only slightly on the dark energy / cosmological constant. From the ratio of the first and second peak we can estimate the amount of matter, while the second to third peak ratio contains information about the dark matter content in the universe. We point the interested reader to the lecture notes and talks by Wayne Hu (<http://background.uchicago.edu/~whu/>) who gives excellent introductions and explanations.

1.2.3 Dark matter halos

A large fraction of the Universe is composed of dark matter, which only interacts by gravity and, depending on the theory, might interact via the weak force. This matter decoupled at earlier times from the photons and grew the small overdensities originating from the quantum fluctuations. This then formed the seeds for the baryonic structure in the Universe. As far as we know, every galaxy and galaxy cluster contains a dark matter halo, a ellipsoidal overdensity of dark matter (often also approximated by a spherical distribution) that contributes a significant part of the potential in the outer regions of a galaxy. The density profile of these dark matter halos can be described by a Navarro-Frenk-White (NFW) profile (Navarro et al., 1996; Navarro et al., 1997)

$$\rho = \frac{\rho_0}{\frac{r}{R_S} \left(1 + \frac{r}{R_S}\right)^2}, \quad (1.13)$$

with R_S being a scale radius, $\rho_0 = \rho_{crit} \delta_{char}$ and δ_{char} is a characteristic overdensity that is related to other commonly used parameters by

$$\delta_{char} = \frac{\Delta_{vir} \Omega_m}{3} \frac{c^3}{\ln(1+c) + \frac{c}{(1+c)}}, \quad (1.14)$$

where $c = r_{vir}/r_S$ is the concentration parameter and Δ_{vir} is the virial overdensity used e.g. $\Delta_{vir} = 200$. The virial radius r_{vir} is the radius of a sphere within which the virial theorem applies and is normally determined using a spherical top-hat model with the condition

$$\rho(< r_{vir}) = \Delta_c \rho_{crit}, \quad (1.15)$$

where ρ_{crit} is the critical density of the Universe as defined in equation (1.7). The variable $\Delta_c = 18\pi^2 + 82(\Omega(z) - 1) - 39(\Omega(z) - 1)^2$ defines the time-dependent overdensity with $\Omega(z) = H_0^2 \Omega_0 (1+z)^3 / H(z)^2$. In an Einstein-de Sitter (EdS) model we have $\Delta_c = 18\pi^2 \approx 178$. More generally, one needs to solve the equation for Δ_c for the given cosmology upon which Ω_0 and $H(z)$ are dependent.

For practical purposes, one uses a $\Delta_c = 200$ or the value for the EdS universe. If one is interested in clusters, the overdensity threshold is often taken to be larger, for example $\Delta_c = 500$. With this, other properties such as the virial mass and circular velocity of the dark matter halo can be easily calculated.

The NFW profile is not a perfect fit but approximates dark matter halos reasonably well. Using a more general profile like the Einasto profile

$$\rho = \rho_{-2} \exp\left(\frac{-2}{\alpha} \left(\frac{r}{r_{-2}}\right)^\alpha - 1\right), \quad (1.16)$$

with ρ_{-2} , r_{-2} being the density and radius where the logarithmic slope $d \ln(\rho)/d \ln(r) = -2(r/r_{-2})^\alpha$ is -2 , and α , the degree of curvature, is fitted to the profile of the halo. This then describes the density profile of the halo more accurately than the NFW profile, due to the additional parameter.

1.2.4 Redshift-space distortions

Observations in cosmology can be done in physical, comoving, or redshift space. Mapping galaxies in 3D space the radial distance is measured by the redshift to the object. Using this and the two angular coordinates ϕ, Θ we can define the redshift space. Observing the galaxy distribution within redshift space, one finds that it appears distorted if their positions are plotted. This effect is caused by the peculiar velocities that introduce a Doppler shift which adds to the cosmological expansion and therefore to the redshift. The observed redshift is a combination of the Hubble flow

$$r(z_s) = \int_0^{z_s} \frac{c dz}{H(z)}, \quad (1.17)$$

and the peculiar velocity v_p . Using the parallel component of the peculiar velocity $v_{p,\parallel}$ the observed redshift can be written as

$$1 + z_{\text{obs}} = (1 + z_s) \left(1 - \frac{v_{p,\parallel}}{c}\right)^{-1}. \quad (1.18)$$

The second term then leads to distortions which are called redshift-space distortions (RSD) and they manifest in two ways. The smaller effect is known as the Kaiser effect which is

caused by the coherent motion of the galaxies that fall into the cluster. This normally leads to a flattening in redshift space. The dominant effect is the 'Fingers of God' effect which leads to an elongation towards the observer. This effect is caused by random peculiar velocities that are close to the virial velocity of the cluster. This velocity changes the measured redshift of the galaxies in the cluster which also leads to a deviation from the Hubble law and therefore the calculated distance. This has to be taken into account when measuring the distance via redshift.

1.3 N-Body simulations

N-Body simulations are a powerful tool to understand the formation and evolution of objects governed by gravitational forces. As an analytic solution is only known for the two-body system, we have to approximate the evolution of larger systems using finite timesteps and a set of differential equations describing the position and velocity of all particles within the system. Depending on the way the gravitational force is calculated, this can be extremely computational expensive. In the following, we give an overview of the way gravity in an N-body system can be calculated, and present the code used throughout this work. This is meant as an introduction and not a deep-dive into the fundamentals of N-Body computation, but should also give a overview of different techniques.

1.3.1 Gravitational force calculation

A interesting question in doing non-relativistic N-Body simulations is the choice of how to compute the gravitational force. In the following, a short overview of a few different methods is given with a focus on the simpler methods, namely the direct summation, particle-mesh, tree, and tree-particle-mesh methods. Some other methods are described shortly but not in great detail.

Direct summation

The most direct way is to take the well known equation for the Newtonian gravitational force (Newton, 1687)

$$F(\vec{r}) = \frac{Gm_i m_j}{|\vec{r}|^2} \frac{\vec{r}}{|\vec{r}|}, \quad (1.19)$$

where $|\vec{r}|$ is the distance, and \vec{r} the vector between the two point masses m_i and m_j . For an N-Body simulation, all contributions from the particles have to be summed and the force on particle j becomes

$$F_j(\vec{r}) = Gm_j \sum_i \frac{m_i}{|\vec{r}_{ij}|^2} \frac{\vec{r}_{ij}}{|\vec{r}_{ij}|}, \quad (1.20)$$

which gives the exact Newtonian force, but its computation time scales as N^2 , where N is the number of particles. This scaling makes the direct summation unfavorable in large N simulations on CPU's. To avoid a singularity at $r \rightarrow 0$, a small number ϵ the gravitational

softening is added to the distance. Recently, there was a shift from using CPU's to compute the gravitational force to exploiting the high processor count on graphics processing units (GPU's). These are tailored to do the same calculation over and over again in a very efficient and parallel way. The raw computational power of GPU's was made available by a recent generation using either the CUDA or OpenCL programming language. This can be used to move the direct summation from the CPU to the GPU as the gravitational computation can be heavily parallelized. This in turn allows for more computations per time unit and makes larger N-Body runs with the direct summation method attractive again.

Particle-Mesh

The main disadvantage of direct summation is the large time consumption and high computational costs. This led to the development of algorithms that approximate the Newtonian force. A fast and rather cheap method to compute the gravitational potential and force is the particle-mesh (PM) method (Hockney & Eastwood, 1981). Here, the particles are binned onto a mesh using an assignment method which basically defines a “shape” of the particle. For this binning, the Cloud-in-Cells (CIC) (Hockney & Eastwood, 1981) assignment is widely used. For a CIC, the particle is assigned to the eight neighboring cells of size s in 3D with a weight w that is computed by the distance per axis ($\Delta x_i = x_{p,i} - x_{c,i}$) to the center (at \vec{x}_c) of those neighbors using

$$w = \prod_i (s - \Delta x_i). \quad (1.21)$$

A computationally more efficient approach to this is to compute only the distance to the center of the parent cell in each axis and use this information to compute the weight for all cells. One could also see this as the particle being distributed to the eight corners of the cubic cell. Other common choices are the nearest neighbor assignment (NGP), the simplest one, where the particle is only assigned to the closest cell and the triangular shaped clouds (TSC) method which involves 27 grid points. This gives the density field on the mesh which is then transformed to Fourier space using discrete Fourier transforms. Most modern PM codes use the FFTW library² to carry out the Fourier transform.

The advantage in Fourier space is that the computation of the gravitational potential from the density is a simple multiplication with the Green's function

$$\hat{G}(\vec{k}) = -4\pi G k^{-2}. \quad (1.22)$$

Having the potential on the mesh with N_G cells, one has to account for potential smoothing effects due to the mass assignment and the force interpolation. In the CIC case, a deconvolution has to be carried out, using

$$D = \text{sinc}^2\left(\frac{k_x L}{2N_G}\right) \text{sinc}^2\left(\frac{k_y L}{2N_G}\right) \text{sinc}^2\left(\frac{k_z L}{2N_G}\right), \quad (1.23)$$

²<http://www.fftw.org>

with the boxsize L and $k_{x,y,z}$ are the components of the k vector. The ratio L/N_G defines the size of a cell and therefore the resolution of this method. The final deconvolution is D^2 due to the smoothing effects and force interpolation. The mesh containing the potential in Fourier space is transformed back into real space and the force is then calculated using a finite differencing method, e.g. the four-point differencing rule

$$\left. \frac{\partial \phi}{\partial x} \right|_{ijk} = \frac{N_G}{L} \left(\frac{2}{3}(\phi_{1,j,k} - \phi_{i-1,j,k}) - \frac{1}{12}(\phi_{i+2,j,k} - \phi_{i-2,j,k}) \right), \quad (1.24)$$

where ϕ_{ijk} is the potential on the grid cell with index i, j, k . With this, one has the force on the mesh, and the final step is an interpolation of the force to the position of the particles which should use the same kernel as the mass assignment to be consistent. There are some disadvantages of this method. One is that the resolution is limited by the number of mesh-cells $\Delta x = L/N_{mesh}$ such that some regions of interest are below the resolution limit. Hence, in a cosmological context, PM simulations are mainly used for large-scale measurements where large volumes are needed, but small scales (e.g. galaxies) are not important. Another problem is the existence of anisotropic force errors.

In cosmological simulations the dynamical range is very large and the limited resolution in the PM method poses a problem if the scales of interest are small. Due to this, a few hybrid methods were developed to increase the dynamic range. A rather intuitive approach is to increase the number of mesh-cells in regions of high density in an adaptive way, which is then called Adaptive Particle-Mesh (A-PM). Another method is to combine the PM method with direct summation in the particle-particle-particle-mesh method (P³M) and the adaptive form A-P³M which creates smaller cells in high-density regions. The main idea behind the P³M, and most other methods that combine with the PM, is to split the potential into a long- and a short-range part. The long-range part is calculated using the particle-mesh while the short-range on the scale of a mesh cell is done using direct summation.

TreePM and fast-multipole-method

A slightly different hybrid approach as the codes above is to approximate the short range force with a Multipole expansion of the potential which is called TreePM (Bagla, 2002). For this the simulation volume is normally divided into cubes such that only nearby particles have to be treated separately and particles farther away are grouped together and treated like a single particle. For each node, the multipole moments are calculated, namely the monopole

$$M = \sum_i m_i, \quad (1.25)$$

and the quadrupole tensor

$$Q_{ij} = \sum_l m_l [3(x_l - s)_i(x_l - s)_j - \delta_{ij}(x_l - s)^2], \quad (1.26)$$

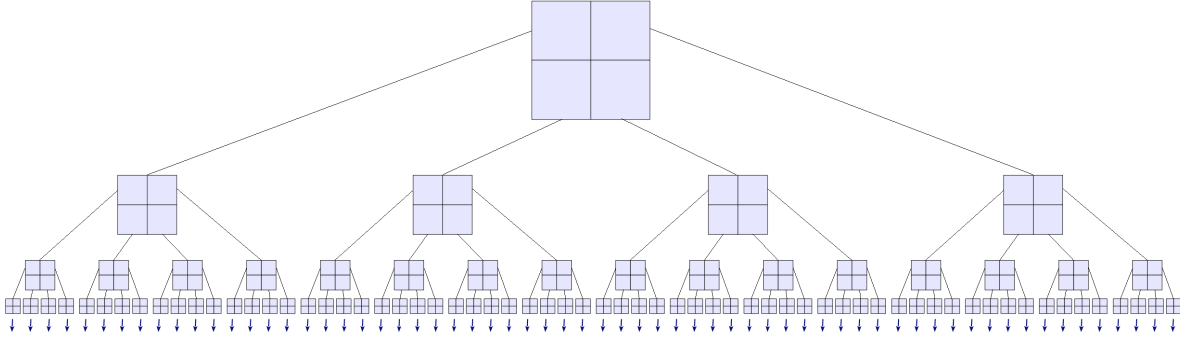


Figure 1.6: Visualization of the Node structure for an oct-tree taken from Springel (2005). The top node contains the full volume while the branches contain sub-volumes until the last node, which are called leaves, only contains single particles.

where s is the distance, of the center of mass of the grouped particles in the distant, to the origin. The dipole moment vanishes exactly after the sum over all particles in a group is done. This can be expanded to the Fast-Multipole-Method (FMM) which takes higher order moments into account. The potential in this expansion can then be written as

$$\phi = -G \left(\frac{M}{|r-s|} + \frac{1}{2} \frac{(r-s)^T Q (r-s)}{|r-s|^5} \right). \quad (1.27)$$

In the FMM the next higher order moments of the multipole expansion are also evaluated and added to the potential. For the short range part, the standard approach in most public codes is to use an opening angle (Θ) criterion to check if a cell/node is far enough away to approximate it as point source. The simplest of these criteria was introduced by Barnes & Hut (1986). A cell with size l and distance d is opened if $d > l/\Theta$. Reducing the opening angle leads to more cell openings and hence a force that is more accurate. This criterion has some problems, especially with cells where the center of mass is close to the edges of the cell (Salmon & Warren, 1994). This can be avoided by including the distance s from the geometric center to the center of mass such that the cell is opened if

$$d > \frac{l}{\Theta} + s.$$

Next to the fixed criterion, there is also the possibility to employ a relative opening criteria which takes the acceleration into account. A node is then opened if

$$\frac{GM}{r^2} \left(\frac{l}{r} \right)^2 \leq |\vec{a}| \alpha,$$

with M being the total mass of the node, l being the extent, r the distance, $|\vec{a}|$ the size of the total acceleration of the previous time step and α is a tolerance factor (“ErrTolForceAcc” in GADGET4). This relative opening angle can lead to issues for small node masses where

it can grow large, as happens close to the convergence radius of the multipole expansion which results in large errors. To limit this effect, a maximum allowed opening angle should be defined and for angles larger than it the computation falls back to the geometrical approach as in the Barnes-Hut algorithm.

1.3.2 Gadget4

For this work, GADGET4 an updated version of the public SPH/N-Body code GADGET2 (Springel, 2005), which is heavily used by a variety of authors is adopted.

The gravitational dynamics in GADGET4 can be described using the Hamiltonian (Springel, 2005)

$$H = \sum_i \left(\frac{1}{2m_i} \frac{\vec{p}_i^2}{a(t)^2} \right) + \frac{1}{2} \sum_i \frac{m_i \phi(\vec{x}_i)}{a(t)}, \quad (1.28)$$

with the peculiar potential $\phi(\vec{x}_i)$ defined through the interaction potential φ which is calculated using periodic boundary conditions by

$$\nabla^2 \varphi(\vec{x}) = 4\pi G \left(-\frac{1}{L^3} + \sum_{(n_1, n_2, n_3)} \tilde{\delta}(\vec{x} - \vec{n}L) \right), \quad (1.29)$$

where L is the box length, $\vec{n} = (n_1, n_2, n_3)$ the integer triplet, and $\tilde{\delta}$ is the single particle density distribution which is the Dirac δ -function convolved with a softening kernel to avoid the singularity for $\Delta x \rightarrow 0$. The peculiar potential is then given as

$$\phi = \sum_j m_j \varphi(\vec{x} - \vec{x}_j). \quad (1.30)$$

In “standard” (TreePM) mode, the potential as defined in equation (1.30) and therefore the force is split in Fourier space using a Gaussian cut-off

$$\phi_k \sim \mathbf{k}^{-2}, \quad (1.31)$$

$$\phi_k^{\text{long}} = \phi_k \exp(-\mathbf{k}^2 r_s^2), \quad (1.32)$$

$$\phi_k^{\text{short}} = \phi_k (1 - \exp(-\mathbf{k}^2 r_s^2)), \quad (1.33)$$

with r_s being the cut-off radius. For $r_s \ll L$ the real space solution for the short range potential is known and can be written as

$$\phi^{\text{short}} = -G \sum_i \frac{m_i}{r_i} \text{erfc} \left(\frac{r_i}{2r_s} \right), \quad (1.34)$$

with the condition that r_i is the smallest distance of particle i to point x . Using the complementary error function “erfc”, the tree has to be walked only in a spatially small region which reduces computational costs. Further, in this way to split the potential, there is no

need for corrections as a result of the periodic boundary conditions.

The long range potential is computed in Fourier space by first binning the particles onto a mesh using an assignment (usually CIC) constructing the density field. This is then transformed into Fourier space by a discrete Fourier transform where it is multiplied by the Green's function (equation 1.22) which has to be modified by the Gaussian truncation. Due to the CIC assignment, one has to correct for smoothing effects in the potential and the interpolation for the force. This is done by a deconvolution of the CIC Kernel using equation (1.23).

To arrive at the force in real space, this potential is transformed back by an inverse Fourier transform and the force is approximated on the mesh using finite differencing of the potential. GADGET4 uses a four-point differencing rule which then offers $\mathcal{O}((L/N_G)^4)$ accuracy. To find the force at the position of the particles, the force on the mesh is interpolated to the position, again using the same assignment method as in the construction of the density field.

1.4 Purpose of this work

The following part of the introduction is based closely on Schmidt et al. (2018).

In this work we are interested in the effect of a large-scale tidal field onto structure formation. To investigate this we modified the force calculation in the most recent version of GADGET4 to allow for an expansion factor that is different for the three principle axes. The effect from the tidal field can be measured by a property called response which we will describe in section 2.3. We first measure the response in the linear regime, where a theoretical prediction exists, expanding the measurement in the mildly nonlinear regime using a particle-mesh (PM) only simulations. With these simulations we can not measure the effect on small scales due to the limited resolution. To address this we run full TreePM simulations that are able to resolve these scales and allow to measure the response in the nonlinear regime. Comparing the response function with a simple halo model, we found a shift in scale, which hints towards an effect on the shape and alignment of halos with respect to the tidal field. To further quantify this we compute the reduced inertia tensor to estimate the shapes and alignment. In the following we want to give a short motivation to this response measurement.

Modern large-scale galaxy surveys offer a precise measurement of the density distribution of galaxies and matter, using a variety of probes like baryon acoustic oscillations (BAO), redshift space distortions (RSD), and gravitational lensing. With this data they aim to understand the cause of the accelerated expansion, and the physics of the early universe (e.g. Inflation), as well as to measure the curvature of the universe and the nature of primordial fluctuations.

This information is normally inferred from n-point statistics that compress the information contained in the underlying field. The simplest of these statistics is the two-point correlation function $\xi(\vec{x})$ with its Fourier counterpart, the power spectrum $P(k) \propto \langle \delta(\vec{k})\delta(\vec{k}') \rangle$. Given the initial conditions provided by the cosmic microwave background (CMB), this provides a possibility to constrain the time-evolution of structure in the universe. At early times, when linear perturbation theory accurately describes the structure evolution of large scales, the power spectrum does fully specify the underlying field. However at late times, when structure formation becomes nonlinear, at least in the standard Λ CDM model, perturbation theory breaks down and cannot fully describe the structure seen in galaxy surveys.

To unleash the full potential of large-scale galaxy surveys, a better understanding of the nonlinear evolution is necessary. In finite volume surveys there are effects from large-scale perturbations which are not directly observable. These fluctuations, even though they have small amplitudes, modify structure on smaller scales due to the nonlinear mode coupling that needs to be included in the analysis. There are two leading effects that come into play. The first is due to a coherent large-scale over- or underdensity in which the survey volume is embedded. The effect of a change in overdensity has been well studied using “separate universe simulations,” N-body simulations with a modified set of cosmological parameters implementing the gravitational effect of the large-scale overdensity (e.g. Frenk et al., 1988; McDonald, 2003; Sirko, 2005; Martino & Sheth, 2009; Gnedin et al., 2011; Li et al., 2014; Wagner et al., 2015b). The second effect is a large-scale tidal field, which will make the local statistics anisotropic. The effects from such a field have not been studied in the quasi-linear and nonlinear regime, while for the linear regime an expression for the influence has been obtained from second-order perturbation theory (Akitsu et al., 2017; Barreira & Schmidt, 2017a) and has been further studied in this regime by Li et al. (2017), and Akitsu & Takada (2017). The change in the angle dependent 3D power spectrum is quantified by a *response function* which is independent of wavenumber in the linear regime.

Akitsu et al. (2017) showed that large-scale tides produce an anisotropic redshift space power spectrum which mimics RSD from peculiar velocities and the Alcock-Paczynski distortion. To linear order the large-scale tidal field, being a quadrupole, does not impact the angle averaged one-dimensional power spectrum and only weakly affects the angle-averaged redshift space power spectrum. To measure the effects of tidal field directly, the angle dependent three-dimensional power spectrum $P(\vec{k})$ has to be used. The anisotropy of the power spectrum also contains information on super-horizon perturbations (Byrnes et al., 2016) or statistical anisotropies in the two-point correlation function originating from physics of inflation (Jeong & Kamionkowski, 2012). To disentangle these primordial effects from the late-time effects of tidal fields requires an accurate understanding of the latter. Further, the tidal response is an important ingredient in the covariance of the nonlinear matter power spectrum (Bertolini et al., 2016; Bertolini & Solon, 2016; Mohammed et al., 2017; Barreira & Schmidt, 2017a,b). Finally, Barreira et al. (2017) recently derived the super-sample covariance of weak lensing power spectra using the response function approach. They showed that the super-sample covariance contains significant contributions

from the tidal field response. Hence, these have to be included in any cosmic shear analysis.

In the linear regime, we find that the measured response follows the theoretical prediction, but in the mildly nonlinear regime, we find a substantial suppression of the response with respect to this linear prediction. This trend was further found in the TreePM runs while the response also showed that the tidal field has an effect on the shape and alignment of halos with respect to the tidal field. Finally measuring the reduced inertia tensor for halos we find a clear difference in the distribution of shapes and angles between the major axis and the principle axis of the tidal field.

Here and throughout this work the unit Mpc denotes comoving Megaparsec.

Chapter 2

Theoretical background

The following chapter gives the broad background for the properties and functions which interest us in this work.

2.1 Correlation functions and power spectrum

At early times, where most of the structure is linear, the two-point statistics contain the full information of the field. In the following, we shortly describe the two-point correlation function and the power spectrum. A more in depth discussion can be found in Peebles (1980) and Baugh (2000), among other books and lecture notes.

The simplest of the possible correlation functions is the two-point correlation function $\xi(\vec{x})$ which measures the number of tracers, or more precisely, the clustering at a given distance in spherical shells. The probability to find a pair of galaxies for a given separation d between the volume elements dV_1 and dV_2 , is

$$dP = \bar{n}^2(1 + \xi(d))dV_1dV_2, \quad (2.1)$$

with the mean galaxy (tracer) density \bar{n} . The simplest way to measure the correlation function is to count galaxy pairs and compute the number to the expected value from a random sample with a Poisson distribution

$$1 + \xi = \frac{\langle DD \rangle}{\langle RR \rangle}, \quad (2.2)$$

where D describes the data and R the random points.

Its Fourier counterpart is called the power spectrum $P(\vec{k})\hat{\delta}(\vec{k}-\vec{k}') \propto \langle \delta(\vec{k})\delta(\vec{k}') \rangle$, where $\delta = (\rho - \bar{\rho})/\bar{\rho}$ describes the overdensity and $\hat{\delta}$ is the delta function. It is related to the correlation function by the Fourier transform

$$\xi(x) = \frac{1}{(2\pi)^3} \int P(k)e^{-i\vec{k}\vec{x}}d^3k. \quad (2.3)$$

This implies that, if we measure the two-point correlation function, we also know the power spectrum and vice-versa. The issue arises if we take a look at the error contributions in the correlation function for a real data set. If we don't expect clustering, the expectation value $\langle \xi \rangle = 0$ and $\langle \xi^2 \rangle = N_{pairs}^{-1}$ where N_{pairs} is the found number of pairs. Given this, the Poisson error is given by

$$\frac{\Delta \xi}{1 + \xi} = \frac{1}{\sqrt{N_{pairs}}}, \quad (2.4)$$

which gives a lower limit to the actual error. As the power spectrum is the Fourier transform of the correlation function, one would assume it would be sufficient to carry out the transform after ξ is obtained. However this leads to errors, as the sample is limited. Considering a CDM power spectrum which for large k goes like $P \sim k^{-3}$ and the transform of the correlation function under the assumption of isotropy is

$$\xi(x) = \frac{1}{(2\pi)^3} \int P(k) \frac{\sin(kx)}{kx} k^2 dk, \quad (2.5)$$

we see that errors at large x , where ξ is affected most by errors, also contribute to smaller scales in the power spectrum. Therefore, estimating the power spectrum directly is the better option. Given a density field sampled by tracers, the contrast in Fourier space is $\hat{\delta}(\vec{k}) = N^{-1} \sum_{i=1}^N e^{i\vec{k}\cdot\vec{x}_i}$. This is under the assumption that the field sampled by the tracers can be represented as a Dirac delta function. Given a random sample without correlation, the Fourier phases of the individual terms are independent, and we find for the variance

$$\langle \hat{\delta}(\vec{k}) \hat{\delta}^*(\vec{k}) \rangle = N^{-1}, \quad (2.6)$$

which is the shot-noise term which has to be subtracted to arrive at the real power spectrum

$$P(k) = \frac{1}{m} \sum |\hat{\delta}(\vec{k})|^2 - \frac{1}{N}, \quad (2.7)$$

with a sum over all modes m with a given wave number k . For galaxy surveys, this is only part of the final result, as they normally cover irregular shapes which have to be taken into account. This is done using a window function describing the shape of the observed volume. This window function has to be convolved with the density contrast to arrive at the actual observed field. We can use the Fourier convolution theorem

$$\hat{f}\hat{\delta} = \hat{f} * \hat{\delta} = \int \hat{f}(\vec{k}') \hat{\delta}(\vec{k}' - \vec{k}) d^3k', \quad (2.8)$$

to calculate this. For a large enough volume compared to the mode $(2\pi/k)$, the Fourier phases are uncorrelated and the observed power spectrum becomes the true one multiplied with the window function

$$P_{obs} = P |\hat{f}(\vec{k})|^2. \quad (2.9)$$

This leads to a smoothing and a change in amplitude of the power spectrum.

From the comparison of the galaxy distribution obtained by surveys such as the SDSS (see Figure 1.2) and simulations of the underlying dark matter field (e.g. Millennium simulation), we can find a connection between the two. Nevertheless, we need to account for the possibility that light (galaxies) is not a perfect tracer of the underlying matter field. Therefore, an additional linear parameter called bias b is introduced which accounts for this on large scales with small density perturbations. The overdensity of galaxies δ_g is then related to that of matter δ_m by

$$\delta_g = b\delta_m, \quad (2.10)$$

and the power spectrum by

$$P_g(k) = b^2 P_m(k). \quad (2.11)$$

Also, from simulations of galaxy formation we see that this model is not sufficient at intermediate and small scales. Further, it is found that the bias is scale-dependent which increases the complexity of the model. To overcome this cosmological simulations of galaxy evolution are used to measure the bias directly and allow for a comparison with the models used in observations.

2.2 Large-scale tidal field

The following describes the equations used to simulate a portion of the universe which is embedded in a large-scale tidal field and is published in Schmidt et al. (2018).

Consider an FLRW metric perturbed by a long-wavelength potential perturbation Φ , which is defined as the perturbation to the 00 component of the metric. Its leading locally observable effects are described by the corresponding tidal tensor

$$\partial_i \partial_j \Phi(\vec{x}, t) = 4\pi G \rho_{\text{bg}} \Pi_{ij}, \quad (2.12)$$

$$\Pi_{ij} = K_{ij,L} + \frac{1}{3} \delta_L \delta_{ij} = \frac{\partial_i \partial_j}{\nabla^2} \delta_L, \quad (2.13)$$

where $\delta_L, K_{ij,L}$ are the long-wavelength density and tidal perturbation corresponding to Φ , respectively. Now consider the case where the wavelength of this mode is much larger than the size of the simulation box. Then, we can approximate Π_{ij} as spatially (but not temporally) constant. If $\Pi_{ij} \propto \delta_{ij}$, equivalently $K_{ij,L} = 0$, the long-wavelength density perturbation can be absorbed in modified cosmological parameters, as derived in Baldauf et al. (2011); Dai et al. (2015) and applied to simulations in Sirko (2005); Gnedin et al. (2011); Li et al. (2014); Wagner et al. (2015b). That is, even in the presence of the long-wavelength perturbation δ_L , the background metric within the simulation retains its FLRW form,

$$ds^2 = -dt^2 + a^2(\tau)(1 + Kr^2/4)^{-2} \delta_{ij} dx^i dx^j, \quad (2.14)$$

where K is the curvature, and both $a(\tau)$ and K are modified by the long-wavelength density perturbation.

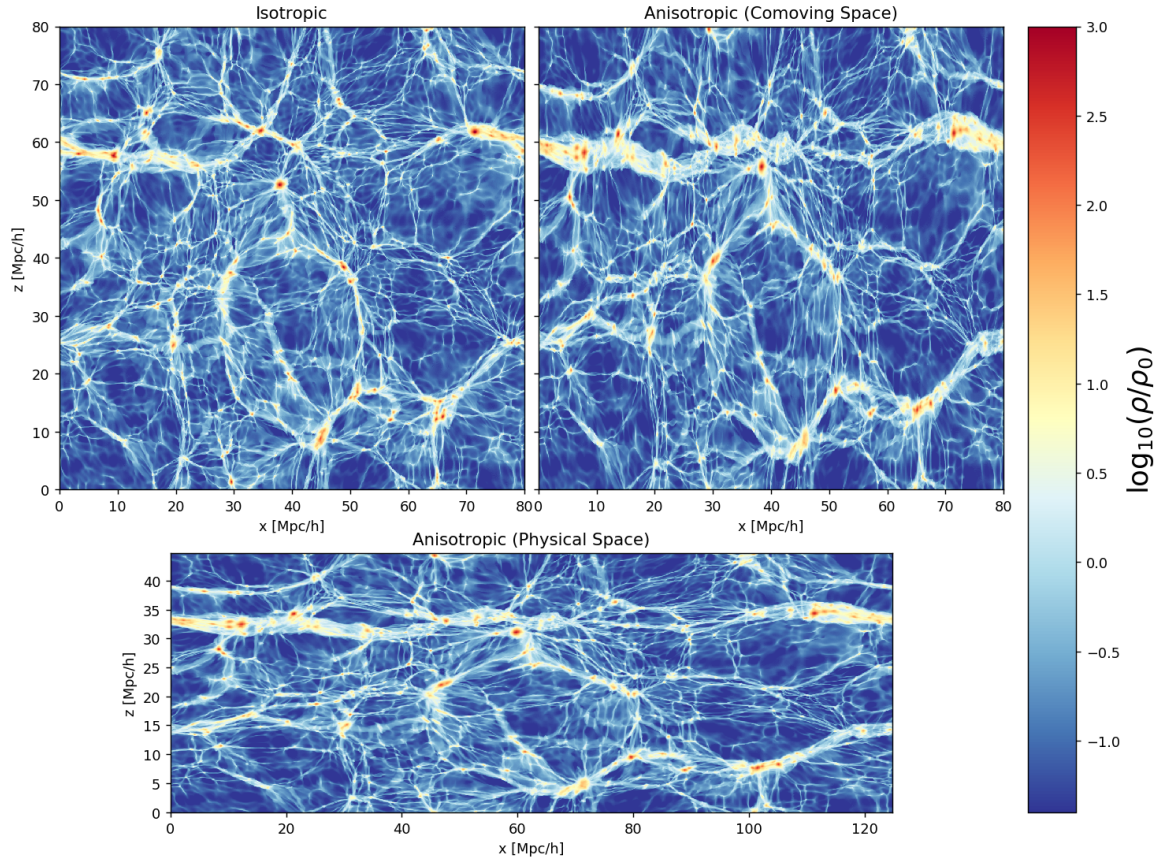


Figure 2.1: Thin slices of the density field of a sample simulation with a boxsize of $80 \text{ Mpc } h^{-1}$ and a strong tidal field with $\lambda = (-0.5, 0, 0.5)$. The left upper panel shows a standard simulation without large-scale tidal field. The right upper panel shows the same initial conditions evolved using a strong tidal field in comoving space. Here we see that most halos seem more elliptical than spherical and some structures are merged that are still separated in the standard case along certain axes. We also see that the structures appear aligned vertically in the x-z projection. The lower panel shows the tidal field simulation in physical space, where the axes are rescaled according to the anisotropic scale factors. In physical space most halos appear elongated in the stretched direction (x-axis) and on larger scales there is a clear alignment of structure with the tidal field. The color represents the overdensity as given by the colorbar on the right.

In this work, we are interested in the case $K_{ij,L} \neq 0$. Consider a homogeneous but anisotropic expanding spacetime,

$$ds^2 = -dt^2 + A_{ij}(t)A^j_k(t)dx^i dx^k, \quad (2.15)$$

where we will also write

$$A_{ij}(t) = a_{\text{bg}}(t)\alpha_{ij}(t), \quad (2.16)$$

where α_{ij} is a symmetric matrix encoding the scale factor perturbation and a_{bg} is an isotropic “background” scale factor which we will specify later. Equation (2.15) is formally the metric describing a Bianchi I spacetime. As shown in Ip & Schmidt (2017) however, a Bianchi I spacetime is *not* equivalent to an FLRW spacetime with a tidal perturbation. Indeed, in order to source the α_{ij} in equation (2.16), a significant large-scale anisotropic stress is necessary, which is not present in standard N-body simulations containing only non-relativistic matter.

However, since motions in large-scale structure are non-relativistic, one can still use equation (2.15) to *simulate* the effect of a long-wavelength tidal field. The spatially homogeneous metric equation (2.15) offers the advantage of being compatible with the periodic boundary conditions employed in N-body simulations. For this, we choose $\alpha_{ij}(t)$ to match the time-time-component of the metric in the comoving (Fermi) frame of the particles induced by a long-wavelength tidal field $\Pi_{ij}(t)$. This approach is related to the “fake separate universe” approach considered by Hu et al. (2016) and Chiang et al. (2016) for isotropic isocurvature perturbations due to dark energy and/or neutrinos.

In order to derive this matching for a general time dependence of the long-wavelength tidal field, we consider the geodesic deviation. Particle trajectories can be written as

$$\vec{x} = \vec{q} + \vec{s}(\vec{q}, t), \quad (2.17)$$

where all coordinates are comoving with respect to a_{bg} , \vec{q} is the initial position and $\vec{s}(\vec{q}, 0) = 0$. For non-relativistic particles in a perturbed FLRW spacetime with scale factor a_{bg} , the displacement obeys

$$\ddot{\vec{s}} + 2H_{\text{bg}}\dot{\vec{s}} = -\nabla_x \Phi(\vec{q} + \vec{s}), \quad (2.18)$$

where $H_{\text{bg}} = \dot{a}_{\text{bg}}/a_{\text{bg}}$, and ∇_x indicates the gradient with respect to the comoving coordinate equation (2.17). Taking the derivative of this equation with respect to \vec{q} yields the evolution of the geodesic deviation $M_{ij} \equiv \partial_{q,j}s_i$:

$$\ddot{M}_{ij} + 2H_{\text{bg}}\dot{M}_{ij} = -(\delta_j^k + M_j^k) \partial_{x,k} \partial_{x,i} \Phi. \quad (2.19)$$

Now consider the motion of comoving test particles in an unperturbed anisotropic spacetime equation (2.15). In terms of physical coordinates, their acceleration is

$$\ddot{r}_i = \frac{d^2}{dt^2}(a_{\text{bg}}\alpha_{ij}) x^j, \quad (2.20)$$

where x^j is the comoving coordinate with respect to the metric equation (2.15), which is constant for comoving observers. On the other hand, in terms of a fictitious FLRW spacetime described by $a_{\text{bg}}(t)$, we have $r_i = a_{\text{bg}}(q_i + s_i)$, so that this trajectory corresponds to a Lagrangian displacement of

$$\begin{aligned}\ddot{r}_i &= \frac{d^2}{dt^2} [a_{\text{bg}}(q_i + s_i)] \\ &= \ddot{a}_{\text{bg}}(q_i + s_i) + 2\dot{a}_{\text{bg}}\dot{s}_i + a_{\text{bg}}\ddot{s}_i.\end{aligned}\quad (2.21)$$

Equating the previous two equations, and using the relation $\alpha_{ij}x^j = q_i + s_i$, we obtain

$$\ddot{s}_i + 2H_{\text{bg}}\dot{s}_i = [2H_{\text{bg}}\dot{\alpha}_{ik} + \ddot{\alpha}_{ik}] (\alpha^{-1})^k_j (q^j + s^j). \quad (2.22)$$

Taking the derivative $\partial/\partial q^j$, and comparing with equation (2.19), immediately yields

$$\partial_{x,i}\partial_{x,j}\Phi = -[2H_{\text{bg}}\dot{\alpha}_{ik} + \ddot{\alpha}_{ik}] (\alpha^{-1})^k_j. \quad (2.23)$$

Thus, when restricting to non-relativistic matter, any given large-scale tidal perturbation $\Pi_{ij}(t)$ (Equation 2.13) can be treated as an effective anisotropic metric, with anisotropic scale factors determined by an ordinary differential equation (ODE). So far, the ‘‘background’’ scale factor $a_{\text{bg}}(t)$ was merely a bookkeeping factor without physical relevance. We now identify it as the scale factor of the background cosmology with respect to which the tidal perturbation Π_{ij} is defined. We then obtain

$$\frac{d}{dt} (a_{\text{bg}}^2 \dot{\alpha}_{ij}) = -\frac{3}{2} \Omega_{m0} H_{\text{bg},0}^2 a_{\text{bg}}^{-1}(t) \alpha_i^k \Pi_{ki}(t), \quad (2.24)$$

where we have rephrased the matter density $\rho_{\text{bg}} \propto a_{\text{bg}}^{-3}$ by using the Friedmann equation for a_{bg} and defining the density parameter Ω_{m0} .

Now, we can use the freedom of rotating the simulation box with respect to the global coordinates, in such a way that α_{ij} becomes diagonal:

$$A_{ij}(t) = \begin{pmatrix} a_1 & 0 & 0 \\ 0 & a_2 & 0 \\ 0 & 0 & a_3 \end{pmatrix} = a_{\text{bg}}(t) \text{diag}(\alpha_1(t), \alpha_2(t), \alpha_3(t)).$$

For simplicity we denote the diagonal elements of α_{ij} as $\alpha_{1,2,3}$. With this, equation (2.24) becomes (see also Stücker et al., 2018)

$$\begin{aligned}\dot{\alpha}_i &= a_{\text{bg}}^{-2} \eta_i, \\ \dot{\eta}_i &= -\frac{3}{2} \Omega_{m0} H_{\text{bg},0}^2 a_{\text{bg}}^{-1}(t) \alpha_i(t) \Pi_{ii}(t),\end{aligned}\quad (2.25)$$

where $i \in \{1, 2, 3\}$, and there is no summation over i . Equation (2.25) describes a set of ordinary differential equations that can be solved, for a given tidal field Π_{ki} , using standard methods. For this paper, we will always consider trace-free tidal perturbations

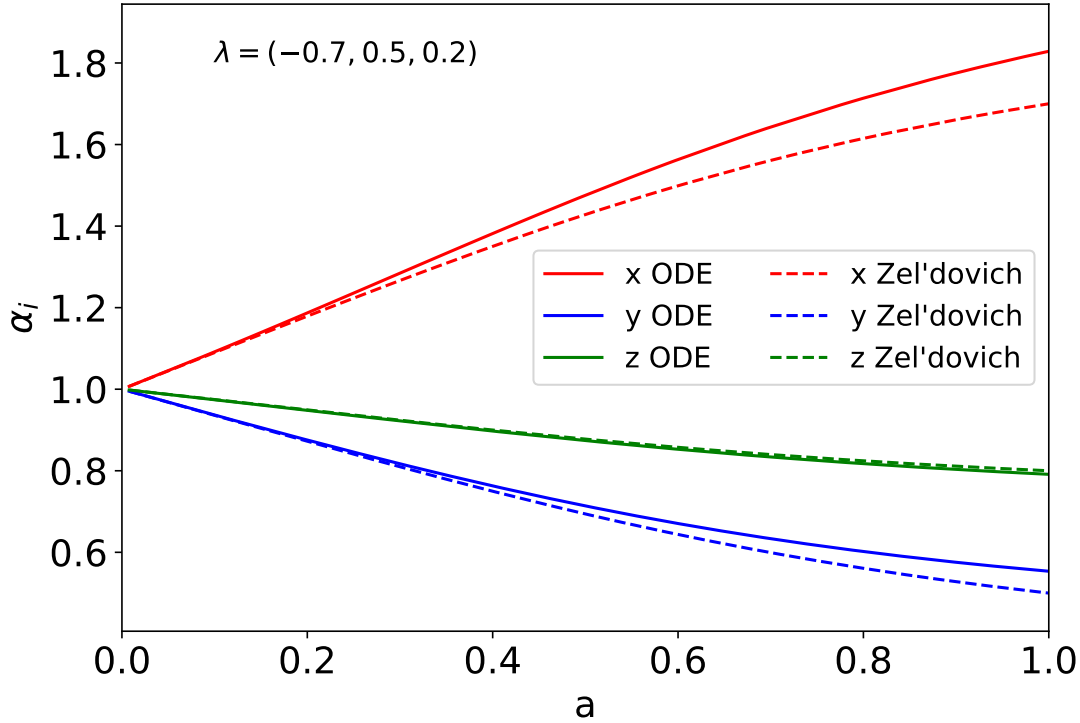


Figure 2.2: The evolution of the relative scale factors α_i for an anisotropic region with deformation tensor eigenvalues $\lambda = (-0.7, 0.5, 0.2)$. The solid line represents the solution from the ordinary differential equation equation (2.25), while the dashed lines represent the Zel'dovich approximation. The different axes are color coded according to the legend.

$\Pi_{ij} \rightarrow K_{ij,L} \propto D(t)$ which follow linear evolution. We integrate the full nonlinear equations of motion equation (2.25),¹ although this does not change the results significantly for the small amplitudes of $K_{ij,L}$ considered in this paper. Further, we parametrize the tidal tensor through (again, no summation over i is implied)

$$\Pi_{ii} = K_{ii,L} + \frac{1}{3}\delta_L = D(t)\lambda_i, \quad (2.26)$$

where λ_i is the amplitude today of the eigenvalues of the tidal tensor, and throughout we consider the case $\delta_L = 0 \Leftrightarrow \lambda_1 + \lambda_2 + \lambda_3 = 0$. If not noted otherwise we refer to λ_i as the eigenvalue at $z = 0$. equation (2.24) simplifies further if we treat the tidal perturbation Π_{ij} as a small parameter, decompose

$$\alpha_{ij} = \delta_{ij} + \hat{\alpha}_{ij}, \quad (2.27)$$

¹We use the ODE solver included in the GNU scientific library (gsl) <https://www.gnu.org/software/gsl/>.

A standalone version of the algorithm to calculate the evolution of α_i, η_i for a tidal field can be found at <https://bitbucket.org/Avalon89/toolset/overview>

and work to linear order in $\Pi_{ij}, \hat{\alpha}_{ij}$. This leads to

$$\frac{d}{dt} \left(a_{\text{bg}}^2 \hat{\alpha}_{ij} \right) = -\frac{3}{2} \Omega_{m0} H_{\text{bg},0}^2 a_{\text{bg}}^{-1}(t) \Pi_{ki}(t). \quad (2.28)$$

For reference, assuming a flat matter-dominated (Einstein-de Sitter) universe and adiabatic scalar perturbation such that $\Pi_{ki}(t) = \Pi_{ki}(t_0) a_{\text{bg}}(t)$, one simply obtains

$$\hat{\alpha}_{ij} \stackrel{\text{EdS, linear}}{=} -\Pi_{ij}(t). \quad (2.29)$$

In the isotropic case $\hat{\alpha}_{ij} = \hat{\alpha} \delta_{ij}$, we find that $\hat{\alpha} = -\delta_L/3$, as follows from mass conservation at linear order in the standard, isotropic separate universe picture. We reiterate that our implementation and results are based on equations (2.24)–(2.25), which do not assume small tidal fields.

Figure 2.1 shows a visualization of the effect of a large-scale tidal field K_{ij} on the structure in a small simulation box with 80 Mpc h^{-1} . We show the results both in comoving and in physical space. In the comoving frame (upper panel), we see that the halos are stretched and squeezed forming ellipsoids, that are preferentially aligned in the vertical direction (x-z plane) while in the Eulerian frame (lower panel), where the box is rescaled according to the anisotropic scale factors α_i , some halos appear spherical while the larger halos show an elongation in the stretched direction (x-axis). This figure shows the result of the N-body implementation which we will describe later.

In Figure 2.2, we show an example of the evolution of the three scale factors. Note that λ_i are chosen to be quite large here for illustration. As expected, at early times the Zel'dovich approximation $\alpha_i(t) = 1 - \lambda_i D(t)$ (dashed lines) works well, while for later times the deviation from the numerical solution of the ODE's (solid lines) becomes significant. Figure 2.2 shows that a negative λ_i is stretching (increasing the expansion) while a positive λ_i is squeezing the simulation box (reducing the expansion).

For the remainder of the thesis we will drop the subscript L and denote $K_{ij,L} \rightarrow K_{ij}$ and $\delta_L \rightarrow \delta$.

Also, for small values of λ , we can use the Zel'dovich approximation and for $\lambda_{x,y,z;1} = -\lambda_{x,y,z;2}$ (where the index $(\dots; i)$ denotes a different set) the change in a is symmetric around a . This property is used later to reduce noise in the measurement of the response. For too large values, this symmetry does not hold and cannot be applied to lower the noise level.

2.3 Response function

We follow the procedures of Barreira & Schmidt (2017a), who defined a response function for the power spectrum, in particular the first order expansion set out in their section 3.2. The three dimensional power spectrum $\langle |\delta(\vec{k})|^2 \rangle$ under the influence of a large-scale overdensity δ and an external tidal field K_{ij} can be written as

$$P(\vec{k}) = P(k) \left(1 + R_1(k) \delta + R_K(k) \hat{k}_i \hat{k}_j K_{ij} \right), \quad (2.30)$$

where \hat{k} is a normalized k vector such that $(\sum_i \hat{k}_i^2)^{1/2} = 1$, K_{ij} is the traceless tidal tensor and R_1 , R_K are the overdensity and tidal field response functions, respectively. This expression is valid at linear order in δ and K_{ij} , and is independent of the wavelength of the large-scale perturbations, as long as it is much larger than $1/k$. Further, the response $R_K(k)$ is independent of the eigenvalues of the deformation tensor K_{ij} . This is not the power spectrum that is normally shown. The power spectrum in most works is averaged on spherical shells which erases the directional dependency and represents the one dimensional power spectrum only as function of distance $|\vec{k}|$. Since the tidal field introduces a directional dependency we can not use the standard angle averaged power spectrum but have to work with the full three dimensional power spectrum. The way we average the three dimensional power spectrum to a function of distance is described in section 2.3.1.

We can write the response function as

$$R_K(k) = G_K(k) - k \frac{P'(k)}{P(k)}, \quad (2.31)$$

where $G_K(k)$ is the growth-only tidal response and $P(k)$ is the mean power spectrum, i.e. in the absence of any tidal effects. The growth-only tidal response is obtained when the modification of the power spectrum is measured in comoving coordinates. Akitsu et al. (2017); Barreira & Schmidt (2017a) derived at leading order in perturbation theory,

$$G_K^{\text{LO}}(k) = \frac{8}{7}, \quad (2.32)$$

which is valid on large-scales as $k \rightarrow 0$. We will compare our results to this result as a consistency test of the implementation. Otherwise, higher order terms need to be taken into account and we would need to use at least the second order expansion to get an unbiased response function. In the small amplitude regime for the tidal field, the expansion above (Equation 2.30) is also valid on small scales, where the structure is nonlinear.

To avoid confusion, we refer to R_K as the first order Eulerian response in the physical frame, while G_K is the first order Lagrangian response in the comoving frame which in the linear regime is simply $G_K = 8/7$. This Lagrangian response can be calculated by applying a standard power spectrum code keeping the box cubic (i.e., calculating the power spectrum in the comoving frame). The second term in equation (2.31) is a result of the coordinate transformation and can be evaluated fully nonlinearly, given a measurement (or fitting function) of the nonlinear isotropic matter power spectrum, and thus does not require anisotropic N-body simulations.

Our simulations use a tidal tensor defined through the eigenvalues at $z = 0$

$$(\lambda_x, \lambda_y, \lambda_z) = \left(-\frac{1}{2}, -\frac{1}{2}, 1 \right) \lambda_z. \quad (2.33)$$

We thus obtain

$$\begin{aligned}
\hat{k}^i \hat{k}^j K_{ij} &= D(t) \left(\lambda_z \hat{k}_z^2 - \frac{\lambda_z}{2} \hat{k}_y^2 - \frac{\lambda_z}{2} \hat{k}_x^2 \right) \\
&= \frac{D(t) \lambda_z}{2} \left(3 \hat{k}_z^2 - 1 \right) \\
&= \lambda_z D(t) Y_2(\mu),
\end{aligned} \tag{2.34}$$

where Y_2 is the second-order Legendre polynomial and $\vec{\hat{k}} \cdot \vec{\hat{z}} = \mu = \hat{k}_z$ is the cosine of the angle between the \mathbf{k} vector and the z axis.

2.3.1 Measuring the response function

We measure the response by computing the 3D power spectrum in the standard simulation without tidal field ($\lambda_i = 0 \forall i$) and in two runs with symmetric eigenvalues $\lambda_{i,A} = -\lambda_{i,B}$ where the second index represents the simulation. Those three runs all originate from the same initial conditions. For the PM-only runs, we use a Fourier grid for the power spectrum calculation of 1024 per axis which gives us a Nyquist frequency of $k_{Nyquist} = 6.43 \text{ h Mpc}^{-1}$. The TreePM runs are analysed slightly differently, as we resolve smaller scales in the gravity calculation due to the Tree part. Therefore, we use the folded powerspectra to increase the range towards smaller scales while keeping the mesh constant with 1024^3 cells.

To minimize effects from the initial conditions, we take the difference of simulations A and B and divide by the run without a tidal field. Using this in equation (2.30), and taking into account the angular dependence by multiplying both sides with the second order Legendre polynomial $Y_2(\mu)$, we find

$$G_K(a) = \frac{\left\langle \left(P(\vec{k}|\lambda_{z,A}) - P(\vec{k}|\lambda_{z,B}) \right) Y_2(\mu) \right\rangle}{\left\langle P(\vec{k}|\lambda_z = 0) Y_2^2(\mu) \cdot \underbrace{D(a) (\lambda_{z,A} - \lambda_{z,B})}_{\approx 2\lambda_z} \right\rangle}, \tag{2.35}$$

where the $\langle \dots \rangle$ denote angle-averaging, and $\lambda_{z,A} = -\lambda_{z,B}$. Here, we weight both sides with $Y_2(\mu)$, as this optimally extracts the tidal response signal following equation (2.34). The final step is to average the response equation (2.35) over the 16 realizations. Equation (2.35) is unbiased up to corrections of order $(K_{ij})^2$, which, for our choice of λ_z , are on the order of 1 percent.

2.3.2 Response predictions

In the following section we will describe predictions for the response in the nonlinear regime. This is based on Section 5 in Schmidt et al. (2018) and the halo model is derived by Fabian Schmidt but is presented here as it is a substantial part of the results for the PM-only and

TreePM simulations.

We will consider two predictions for the response $G_K(k)$ on nonlinear scales. First, Barreira & Schmidt (2017a) proposed that the shape of G_K would follow that of the growth-only density response G_1 measured in Wagner et al. (2015a), with a normalization chosen so that the correct low- k asymptote is obtained:

$$G_K(k) = \frac{12}{13} G_1(k). \quad (2.36)$$

This was merely a simple ansatz to obtain numerical results for R_K (and six further second-order response functions).

Second, we derive the prediction for the nonlinear tidal response $G_K(k)$ in the halo model (see Cooray & Sheth (2002) for a review), paralleling the derivation of the density response in Takada & Hu (2013), Chiang et al. (2014), and Wagner et al. (2015a). Adopting the notation of Takada & Hu (2013), the halo model power spectrum, $P_{\text{HM}}(k)$, is given by

$$\begin{aligned} P_{\text{HM}}(k) &= P^{2\text{h}}(k) + P^{1\text{h}}(k), \\ P^{2\text{h}}(k) &= [I_1^1(k)]^2 P_{\text{lin}}(k), \\ P^{1\text{h}}(k) &= I_2^0(k, k), \end{aligned} \quad (2.37)$$

where $P^{n\text{h}}(k)$ denotes the n -halo term,

$$\begin{aligned} I_m^n(k_1, \dots, k_m) &\equiv \int d \ln M n(\ln M) \left(\frac{M}{\bar{\rho}} \right)^m b_n(M) \\ &\quad \times u(M|k_1) \cdots u(M|k_m), \end{aligned} \quad (2.38)$$

and $n(\ln M)$ is the mass function (comoving number density per interval in log mass), M is the halo mass, $b_n(M)$ is the n -th order local bias parameter, $u(M|k)$ is the dimensionless Fourier transform of the halo density profile, for which we use the NFW profile (Navarro et al., 1997) and P_{lin} is the linear power spectrum. We normalize u so that $u(M|k \rightarrow 0) = 1$. The notation given in equation (2.38) assumes $b_0 \equiv 1$. $u(M|k)$ depends on M through the scale radius r_s , which in turn is given through the mass-concentration relation. All functions of M in equation (2.38), along with P_{lin} , are also functions of z although we have not shown this for clarity. In the following, we adopt the Sheth-Tormen mass function (Sheth & Tormen, 1999) with the corresponding peak-background split bias, and the mass-concentration relation of Bullock et al. (2001). The exact choice of the latter only has a small impact on the predictions which does not affect our conclusions.

An assumption that goes into the analysis is that the density profile averaged over all halos in the 1-halo term are spherical symmetric. This however is not true as shown in the top panel of Figure 2.1. In the image above (Figure 2.1) we also see that the major axis is not randomly orientated with respect to the z -axis of the box but rather aligned vertically in the x - z projection. It should be noted that the image was produced using large eigenvalues of the tidal field. Therefore using small eigenvalues of the tidal tensor the

simple halo model could still agree with the measured response. If this is not the case we see that even the weak tidal field has an effect on the shape and alignment of halos. We will see this effect later in Figure 5.2 where the halo model is shifted in k compared to the measured response function.

Now consider the tidal response. First, the linear power spectrum changes according to

$$P_{lin}(k) \rightarrow \left[1 + \frac{8}{7} \hat{k}^i \hat{k}^j K_{ij} \right] P_{lin}(k). \quad (2.39)$$

Unlike the case of the response to a long-wavelength density perturbation, the halo number density is unchanged by a tidal field at linear order, since it is a scalar (McDonald & Roy, 2009; Mirbabayi et al., 2015; Desjacques et al., 2016). Thus, the only remaining effect to consider is a possible change in the halo profiles.

A zeroth-order assumption we make is that the inner regions of halos are unaffected by the large-scale tidal field, if they virialize and decouple from large-scale perturbations at early times. Thus, the halo profiles are unchanged in *physical* coordinates that implies in terms of our comoving coordinates

$$u(M|\vec{k}) \Big|_{K_{ij}} = u \left(M \left[1 + K_{ij} \hat{k}^i \hat{k}^j \right] k \right), \quad (2.40)$$

where we have expanded to linear order in K_{ij} and used equation (2.29). Equivalently, since the NFW profile $u(M|k)$ is a function of kr_s , where $r_s = R_{vir}(M)/c(M)$ is the scale radius and c is the concentration, we can rephrase this rescaling in terms of the concentration:

$$c(M) \Big|_{K_{ij}} = \left[1 + C_K K_{ij} \hat{k}^i \hat{k}^j \right] c(M), \quad (2.41)$$

where we have introduced a constant C_K to allow for a more general behavior. An unchanged halo profile in physical coordinates corresponds to $C_K = 1$, since $c \propto 1/r_s$ is the inverse of a physical length. Clearly, we expect C_K to be in the approximate range of $0 \lesssim C_K \lesssim 1$.

Putting everything together, we obtain

$$\begin{aligned} G_K^{\text{HM}}(k) P_{\text{HM}}(k) &= \frac{8}{7} [I_1^1(k)]^2 P_{lin}(k) \\ &+ C_K \left[2 (I_1^1)_{,\ln c}(k) I_1^1(k) P_L(k) + (I_2^0)_{,\ln c}(k, k) \right], \end{aligned} \quad (2.42)$$

where

$$\begin{aligned} (I_1^1)_{,\ln c}(k) &= \int d \ln M n(\ln M) \left(\frac{M}{\bar{\rho}} \right) b_1(M) \left[\frac{\partial u(M|k)}{\partial \ln c} \right], \text{ and} \\ (I_2^0)_{,\ln c}(k, k) &= 2 \int d \ln M n(\ln M) \left(\frac{M}{\bar{\rho}} \right)^2 u(M|k) \\ &\quad \times \left[\frac{\partial u(M|k)}{\partial \ln c} \right], \end{aligned} \quad (2.43)$$

are the derivatives of the relevant mass integrals with respect to the halo concentration. Note that both of these integrals scale as k^2 in the large-scale limit, so that the effect of the tidal field on halo profiles (in comoving units) is only relevant on small scales, as expected.

If the inner regions of halos indeed do not respond to the tidal field in physical space (corresponding to $C_K = 1$), then we expect the Eulerian response to be asymptotic to zero at large k . Via equation (2.31), this implies

$$G_K(k) \xrightarrow{k \rightarrow \infty} \frac{d \ln P(k)}{d \ln k}, \quad (2.44)$$

which is roughly -2 . We will indeed see a change of sign in the simulation measurements of $G_K(k)$ on small scales.

2.4 Halo shapes and alignments

The shape of dark matter halos is widely studied in cosmological simulations, and those showed that a triaxial model does describe it reasonable well (e.g. Frenk et al., 1988; Dubinski & Carlberg, 1991; Warren et al., 1992; Bailin & Steinmetz, 2005; Hopkins et al., 2005; Gao et al., 2012). So in order to see if the large-scale tidal field influences the shape and alignment with respect to the simulation box, we identify halos and subhalos for which we compute the axes ratios:

$$q = b/a, \quad (2.45)$$

$$s = c/a, \quad (2.46)$$

with a being the semi-major axis of the ellipsoid, c being its semi-minor axis. These ratios are one way to compare the simulations with and without tidal field. To arrive at the axis values, we use the most common method for computing the length of the principal semi-axes which uses the reduced inertia tensor using all N particles within the ellipsoid/sphere²

$$I_{ij} = \frac{1}{N} \sum_n \frac{x_{i,n} x_{j,n}}{r_n^2}, \quad (2.47)$$

with the elliptical distance in the eigenvector system $r_n^2 = x_n^2 + y_n^2/q^2 + z_n^2/s^2$ for particle n relative to the center of the halo. In the first step we have $q = 1$ and $s = 1$ as we start with a sphere. This is done for all particles within the sphere of radius r_{cut} which defines our cut off radius. The principal axes $e_i = \{a \geq b \geq c\}$ are given by the eigenvalues λ_I from the inertia tensor $\underline{\underline{I}}$ by

$$e_i = \sqrt{\lambda_{I,i}}, \quad (2.48)$$

while the normalized eigenvectors \hat{i} describe the direction of each corresponding eigenvalue/axis. Knowing both allows us to determine the axis ratio, and orientation relative to the box. In contrast to the iterative approach as described in e.g. Schneider et al. (2012),

²Note that all particles have the same mass.

which starts by using a sphere with radius r_s which is then deformed according to the eigenvalues and eigenvectors while keeping the volume within the ellipsoid constant, we only use the first step.

Normally one uses an iterative approach to converge to the true ellipsoid and ignoring this iterative process biases the axes ratios, especially s , towards higher values (Tenneti et al., 2015), but comparing two distributions is still possible. In our case, we are only interested in the difference between the simulations with and without tidal field; therefore we only calculate the inertia tensor for all particles within the initial sphere of radius $r = R_{vir,m} = r_{cut}$. This includes also particles that are not part of the main subhalo but has the least influence from the used subhalo finder. Strictly speaking this does not directly translate the eigenvalue to the length of the principle axes of the ellipsoid, but we will label the ratio of the largest ($\lambda_{I,0}$) to smallest ($\lambda_{I,2}$) eigenvalue as $s = c/a = \sqrt{\lambda_{I,2}/\lambda_{I,0}}$.

Next to directly comparing the axes ratios we have another property that shows the influence of the tidal field: the average ratio for the inertia tensor components, given by

$$R = \left\langle \frac{I_{zz}}{I_{xx} + I_{yy}} \right\rangle, \text{ or} \quad (2.49)$$

$$R_{tr} = \frac{\langle I_{zz} \rangle}{\langle tr(I) \rangle} - \frac{1}{3}, \quad (2.50)$$

which is written with the eigenvalues of the used tidal field in mind. There, the z eigenvalue is the largest, while x and y are the opposite sign and half the value of that in the z direction (see equation (2.33)). The first ratio (equation 2.49) should be 1/2 for a random uniform distribution, as is the case for the standard simulations without tidal field, while the second ratio (equation 2.50) should be 0. For the runs that include a tidal field, we expect to see a non-uniform distribution of alignment angles, and therefore the ratios given by equations (2.49)–(2.50) should be different from zero. Additionally we compute the angles between the eigenvector for the major axis and the different principal axes of the box. In the case of the tidal field we should see an enhancement towards $\cos(\angle ax_i) = 0(1)$ depending on the sign of the eigenvalue for the given axis. For the negative eigenvalues we expect to see a bias towards the preferred axis of the tidal field and therefore more halos with $\cos(\angle ax_i) = 1$. For the opposite sign more halos should show an cosine close to zero.

Measuring the probability density distribution (PDF) $p(x)$ for the cosine of the angle between the major axis and the strongest eigenvalue direction, in our case the z-direction, we can also estimate the distributions for the x or y direction. This can be done as the other directions are not independent from the z direction. The angle between the major axis and the three axes of the tidal field can be described by the direction cosines with respect to the system of the tidal field \hat{u}_i . For the isotropic case the PDF has the condition to be unity $p(\hat{u}_i) = 1 \forall i \in x, y, z$. Here we assume that the distribution for x and y are identical and only that of z is different. We start with the joint PDF for the directional

cosine of the z and x direction:

$$p(\hat{u}_x, \hat{u}_z) = p(\hat{u}_x|\hat{u}_z)p(\hat{u}_z). \quad (2.51)$$

From here we can find the PDF for the x cosine as

$$p(\hat{u}_x) = \int d\hat{u}_z p(\hat{u}_x|\hat{u}_z)p(\hat{u}_z) = \int d\hat{u}_z \frac{1}{\sqrt{1 - \hat{u}_x^2 - \hat{u}_z^2}} p(\hat{u}_z), \quad (2.52)$$

where the last step uses that the distribution is uniform on a unit circle in the x-y plane. Now to simplify this equation we change the variable using $\hat{u}_z = y\sqrt{1 - \hat{u}_x^2}$ which gives

$$p(\hat{u}_x) = \int_0^1 dy \frac{\sqrt{1 - \hat{u}_x^2}}{\sqrt{(1 - \hat{u}_x^2)(1 - y^2)}} p(y\sqrt{1 - \hat{u}_x^2}) = \int_0^1 dy \frac{1}{\sqrt{(1 - y^2)}} p(y\sqrt{1 - \hat{u}_x^2}). \quad (2.53)$$

Now integrating this for the isotropic case we get the normalization as we need to satisfy $p(\hat{u}_x) = p(\hat{u}_y) = p(\hat{u}_z) = 1$ and find

$$p(\hat{u}_x) = \frac{2}{\pi} \int_0^1 dy \frac{1}{\sqrt{(1 - y^2)}} p(y\sqrt{1 - \hat{u}_x^2}). \quad (2.54)$$

For this we only need to measure the distribution for the z direction and can then estimate that of the x or y direction. As example this can be used to check the output from the simulation.

Chapter 3

Code modifications

In the following part of this thesis, the modifications to the SPH/N-Body code `GADGET4` are described in detail. In `GADGET4`, the gravitational force is calculated using the TreePM algorithm which splits the force into a long- and a short-range component. The details for this method are described in 1.3.1. While the long-range force is calculated on the Particle-Mesh using Fourier techniques, the short-range is done using the Tree. To allow for an anisotropic expansion factor, both parts have to be modified. For `GADGET4`, the potential, and therefore the force, is split in Fourier space using a Gaussian cut-off as described in section 1.3.2 equations (1.31)–(1.33).

3.1 Modified particle mesh in Gadget4

For the long range part, the modifications are quite simple and are published in Schmidt et al. (2018).

We start with the Equations of Motion (EoM) which are described by the Hamiltonian in the anisotropic expanding case

$$H = \sum_i \left(\frac{1}{2m_i} \sum_k \frac{p_{i,k}^2}{a_k(t)^2} \right) + \frac{1}{2} \sum_i \frac{m_i \phi(\vec{x}_i)}{a(t)(\alpha_x \alpha_y \alpha_z)}, \quad (3.1)$$

with the canonical momentum $p_{i,k} = a_k^2 m_i \dot{x}_{i,k}$, where the index $k \in [x, y, z]$ defines the axis. From the Hamiltonian equation (3.1) we obtain the equations for the change in momentum

$$\dot{p}_i = -\frac{m_i}{2} \frac{\partial_i \phi}{a_{\text{bg}} \alpha_x \alpha_y \alpha_z}, \quad (3.2)$$

and the potential can be calculated by solving the Poisson equation, which in the anisotropic case is given as

$$\underbrace{\sum_i \alpha_i^{-2} \partial_i^2}_{\equiv \nabla'^2} \phi = 4\pi G \rho_{0,*} \delta a_{\text{bg}}^2, \quad (3.3)$$

where the derivative $\nabla'^2\phi$ is with respect to the new rescaled comoving coordinate, $\rho_{0,*} = \bar{\rho}/(a_x a_y a_z)$ is the mean density of the box, $\bar{\rho}$ is the mean density of the universe without the imposed tidal field and δ describes the overdensity.

The first step to compute the forces is to calculate the potential on the mesh. On the particle mesh, the Poisson equation can be simply solved by Fourier-transforming equation (3.3)m which leads to

$$\sum \alpha_i^{-2} k_i^2 \hat{\phi} = -4\pi G \rho_{0,*} \hat{\delta} a_{\text{bg}}^2, \quad (3.4)$$

$$\hat{\phi} = -4\pi G \frac{\bar{\rho}_0}{a_{\text{bg}} \alpha_x \alpha_y \alpha_z} \frac{\hat{\delta}}{\sum \alpha_i^{-2} k_i^2} \quad (3.5)$$

$$=: 4\pi G \frac{\bar{\rho}_0}{a_{\text{bg}}} \frac{\hat{\delta}}{\alpha_x \alpha_y \alpha_z} \hat{G}_*(\vec{k}), \quad (3.6)$$

where G_* denotes the Green's function. In practice, the potential calculation on the particle mesh has to be modified by replacing the isotropic Green's function $\hat{G}(\vec{k}) = -1/(\sum k_i^2)$ by the anisotropic one $\hat{G}_*(\vec{k}) = -1/(\sum \alpha_i^{-2} k_i^2)$. Using the standard definition of the overdensity in the code, there is also a rescaling of the overdensity $\hat{\delta} \rightarrow \hat{\delta}/(\alpha_x \alpha_y \alpha_z)$ which accounts for the different box lengths per axis.¹ The final step to calculate the force is to take the finite difference between neighboring cells which then gives the acceleration.

3.2 Modified tree in Gadget4

To compute the real space short range component, using $\phi_S = \phi - \phi_L$, we need to estimate the long range potential in real space. The following section describes the changes done on the Tree in GADGET4 which allow for the computation of the new TreePM potential.

3.2.1 Elliptical potential

To find the real space short range potential we have to evaluate $\phi_L = \rho * (G_* * f)$ as a convolution of the density ρ , the Green's function G_* and a cut-off function f which in the case of GADGET4 is a Gaussian $f(r) = \exp(-u^2(\vec{r})/(2\sigma^2))$ with the cut off radius σ and $u^2(\vec{r}) = r^2$ in the standard case. The basic idea is to see the long range potential equation (1.32) as the potential of a density distribution convolved with an elliptical Gaussian kernel. So we change the long range Green's function $G_{*,L} = G_* * f$ by changing the Gaussian from a spherical to an elliptical kernel. For this, our Gaussian has a new function

$$u^2(\vec{r}) = \frac{x^2}{a^2} + \frac{y^2}{b^2} + \frac{z^2}{c^2},$$

¹In the traceless case for the tidal field the product of the α_i 's is actually exactly one and has no influence on the calculations.

where a, b, c are the half axes of the ellipse and x, y, z are the three components of the vector \vec{r} . Therefore, following e.g. Chandrasekhar (1969), one can write the long range potential for an ellipsoid as

$$\phi_L = 2\pi abc \int_0^\infty \frac{G(\infty) - G(u(v, x, y, z))}{\sqrt{(a^2 + v)(b^2 + v)(c^2 + v)}} dv, \quad (3.7)$$

with

$$G(u) = \int_0^u u' \rho(u') du',$$

and

$$u = \sqrt{\frac{x^2}{a^2 + v} + \frac{y^2}{b^2 + v} + \frac{z^2}{c^2 + v}}.$$

In this specific case, we have for the kernel $\rho(u) = \rho_0 \exp(-u^2/(2\sigma^2))$. With that $G(u), G(\infty)$ can be calculated by

$$\begin{aligned} G(u) &= \rho_0 \int_0^u u' \exp\left(-\frac{u'^2}{2\sigma^2}\right) du' = \rho_0 \sigma^2 \left[1 - \exp\left(-\frac{u^2}{2\sigma^2}\right)\right], \\ \rightarrow G(\infty) &= \rho_0 \sigma^2. \end{aligned} \quad (3.8)$$

Now, inserting equation (3.8) into equation (3.7), the equation for the potential is found as

$$\begin{aligned} \phi_L(\vec{x}) &= 2\pi a b c \rho_0 \sigma^2 \\ &\times \int_0^\infty \frac{\exp\left[-\frac{1}{2\sigma^2} \left(\left(\frac{x^2}{a^2+v}\right) + \left(\frac{y^2}{b^2+v}\right) + \left(\frac{z^2}{c^2+v}\right)\right)\right]}{((a^2 + v)(b^2 + v)(c^2 + v))^{1/2}} dv. \end{aligned} \quad (3.9)$$

This is now a function of the three axes of the ellipsoid $a, b, c = \alpha_0, \alpha_1, \alpha_2$ and an elliptical coordinate v . The long range potential equation (3.9) can not be solved analytically. In this work, we approximate the long range potential by a series expansion around a mean $\bar{\alpha} \equiv (\alpha_0 \alpha_1 \alpha_2)^{1/3}$. This results in an integral that is independent of the different directions which means the integral can be calculated once and stored in an interpolation table for different $\bar{\alpha}$. Only the additional factors from the expansion are dependent on direction and are easy and - most importantly - fast to calculate.

3.2.2 Elliptical potential approximation - Series expansion

Following the short derivation of the analytic form the approximation of the long range potential is described. Since we only expect moderate axis ratios we expand the integrand in equation (3.9)

$$\zeta = \frac{\exp\left[-\frac{1}{2\sigma^2} \left(\left(\frac{x^2}{a^2+v}\right) + \left(\frac{y^2}{b^2+v}\right) + \left(\frac{z^2}{c^2+v}\right)\right)\right]}{((\alpha_0^2 + v)(\alpha_1^2 + v)(\alpha_2^2 + v))^{1/2}}, \quad (3.10)$$

around the spherical case $\alpha_i = \bar{\alpha} \forall i \in 0, 1, 2$. In the spherical case the integrand (3.10) can be simplified to

$$\zeta|_{\bar{\alpha}=\bar{\alpha}} = L_3, \quad (3.11)$$

with

$$L_m = \frac{\exp\left[-\frac{1}{4r_s^2}\left(\frac{r^2}{\bar{\alpha}^2+v}\right)\right]}{(\bar{\alpha}^2+v)^{m/2}}, \quad (3.12)$$

where we replaced $\sigma = \sqrt{2}r_s$. The series expansion up to second order is given as

$$\zeta \approx L_3 + \sum_i \frac{\partial \zeta}{\partial \alpha_i} \Big|_{\bar{\alpha}=\bar{\alpha}} (\alpha_i - \bar{\alpha}) + \frac{1}{2} \sum_{ij} \frac{\partial^2 \zeta}{\partial \alpha_i \partial \alpha_j} \Big|_{\bar{\alpha}=\bar{\alpha}} (\alpha_i - \bar{\alpha})(\alpha_j - \bar{\alpha}) + \mathcal{O}(3). \quad (3.13)$$

The first and second order terms are given as:

$$\frac{\partial \zeta}{\partial \alpha_i} \Big|_{\bar{\alpha}=\bar{\alpha}} = L_5 \bar{\alpha} + L_7 x_i^2 \frac{\bar{\alpha}}{2r_s^2} = L_5 f_{5,I} + L_7 f_{7,I}, \quad (3.14)$$

$$\begin{aligned} \frac{\partial^2 \zeta}{\partial \alpha_i \partial \alpha_i} \Big|_{\bar{\alpha}=\bar{\alpha}} &= -L_5 + L_7 \left(3\bar{\alpha}^2 + \frac{x_i^2}{2r_s^2}\right) + \bar{\alpha}^2 \left(-L_9 \frac{3x_i^2}{r_s^2} + L_{11} \frac{x_i^4}{4r_s^2}\right) \\ &= f_{5,II} L_5 + L_7 f_{7,II,i=j} + L_9 f_{9,II,i=j} + L_{11} f_{11,II,i=j}, \end{aligned} \quad (3.15)$$

$$\begin{aligned} \frac{\partial^2 \zeta}{\partial \alpha_i \partial \alpha_j} \Big|_{\bar{\alpha}=\bar{\alpha}} &= \bar{\alpha}^2 \left(L_7 - L_9 \frac{x_i^2 + x_j^2}{2r_s^2} + L_{11} \frac{x_i^2 x_j^2}{4r_s^2}\right) \\ &= f_{7,II,i \neq j} L_7 + f_{9,II,i \neq j} L_9 + f_{11,II,i \neq j} L_{11}, \end{aligned} \quad (3.16)$$

where the factors for the different L_m are labeled $f_{m,I}$ for the first order terms while those for the second order are $f_{m,II,\dots}$ as indicated in equations (3.14)–(3.16). Integrating equation (3.12) over v we find the solution:

$$I_m = \int_0^\infty L_m dv = \left(\frac{2r_s^2}{r}\right)^{m-2} \left(\Gamma\left[\frac{m-2}{2}, 0\right] - \Gamma\left[\frac{m-2}{2}, \frac{r^2}{4\bar{\alpha}^2 r_s^2}\right]\right), \quad (3.17)$$

with the incomplete gamma function Γ . Therefore the potential (3.9) can be written as series up to first order in $\Delta\alpha_i = \alpha_i - \bar{\alpha}$:

$$\phi_L(\vec{x}) \approx 4\pi abc \rho_0 r_s^2 \left(I_3(r) + \sum_i \left(I_5(r) \bar{\alpha} + I_7 x_i^2 \frac{\bar{\alpha}}{2r_s^2} \right) \overbrace{(\alpha_i - \bar{\alpha})}^{\equiv \Delta\alpha_i} + \dots \right). \quad (3.18)$$

We give the full expansion for the potential in Appendix A.1.

3.2.3 Force equations

The next step is to derive the equation for the force given by

$$F^{\text{long}} = \nabla \Phi_L = 4\pi abc \rho_0 r_s^2 \left(\frac{\vec{x}}{r} \sum f_m \partial_r I_m(r) + \sum I_m \nabla f_m \right), \quad (3.19)$$

with the factors f_m from equations (3.14)–(3.16) and the derivative of I_m

$$I'_m := \partial_r I_m = \frac{1}{4r} \left(\frac{r_s}{r} \right)^m \left(8\bar{\alpha}^2 \exp \left(-\frac{r^2}{4\bar{\alpha}^2 r_s^2} \right) \left(\frac{r^2}{\bar{\alpha}^2 r_s^2} \right)^{m/2} - \frac{2^m(m-2)r^2 \left(\Gamma \left[\frac{m-2}{2}, 0 \right] - \Gamma \left[\frac{m-2}{2}, \frac{r^2}{4\bar{\alpha}^2 r_s^2} \right] \right)}{r_s^2} \right). \quad (3.20)$$

The derivatives for f_m with respect to x_i are:

$$\frac{\partial}{\partial x_i} f_3 = 0, \quad (3.21)$$

$$\frac{\partial}{\partial x_i} f_5 = 0, \quad (3.22)$$

$$\frac{\partial}{\partial x_i} f_{7,I} = \frac{\bar{\alpha}}{r_s^2} \Delta \alpha_i x_i, \quad (3.23)$$

$$\frac{\partial}{\partial x_i} f_{7,II,l=m} = \frac{x_i}{r_s^2}, \quad (3.24)$$

$$\frac{\partial}{\partial x_i} f_{7,III \neq m} = 0, \quad (3.25)$$

$$\frac{\partial}{\partial x_i} f_{9,II,l=m} = -\frac{6x_i}{r_s^2} \bar{\alpha}^2, \quad (3.26)$$

$$\frac{\partial}{\partial x_i} f_{9,II,l \neq m} = -\bar{\alpha}^2 \frac{x_i}{r_s^2}, \quad (3.27)$$

$$\frac{\partial}{\partial x_i} f_{11,II,l=m} = \frac{x_i^3}{r_s^4} \bar{\alpha}^2, \quad (3.28)$$

$$\frac{\partial}{\partial x_i} f_{11,II,l \neq m} = \frac{x_i x_j^2}{2r_s^4} \bar{\alpha}^2, \quad (3.29)$$

where I, II denotes the first and second order expansion, respectively.

Hence to first order the force along axis i is given as

$$\frac{\partial \Phi}{\partial x_i} = 4\pi abc \rho_0 r_s^2 \left[\frac{x_i}{r} \left(I'_3 - \bar{\alpha} I'_5 \sum_j \Delta \alpha_j + \frac{\bar{\alpha}}{2r_s^2} I'_7 \left(\sum_j (\Delta \alpha_j x_j^2) \right) \right) + \frac{\bar{\alpha}}{r_s^2} I_7 \Delta \alpha_1 x_i \right], \quad (3.30)$$

with the difference from the mean $\Delta\alpha_i = \alpha_i - \bar{\alpha}$ and the second order terms read as

$$\begin{aligned} & \frac{x_i}{2r} \left(\sum_l \sum_m (\Delta\alpha_l \Delta\alpha_m (f_5 I'_5 + f_7 I'_7 + f_9 I'_9 + f_{11} I'_{11})) \right) \\ & + \frac{1}{2} \sum_l \sum_m (\Delta\alpha_l \Delta\alpha_m (f'_5 I_5 + f'_7 I_7 + f'_9 I_9 + f'_{11} I_{11})) . \end{aligned} \quad (3.31)$$

These equations can be again simplified in order to allow better implementation into the code, and give very good approximations for the force in the anisotropic case for our used ratios of the axes. Knowing the long range force, the short range force can easily be calculated due to the force split in GADGET4.

There is still the issue with the force softening, as we have the choice between two frames, comoving and physical. The softening, in contrast to the standard case, is only spherical in one of the two frames, and we chose to use the physical frame for this. The forces are calculated in physical coordinates and as such a spherical softening in this frame reduces the code modifications and lowers the potential to introduce errors.

3.2.4 Tests

To test the new implementation, we run a test simulation, a $L = 10 \text{ Mpc } h^{-1}$ box containing 128^3 particles, to a specific point where the axes ratios can be expressed as multiples of a new boxsize $L = iL_x$ with $i \in \mathbb{Z}$ and being different for each axis. This snapshot is then evolved forward for a full time step using the standard Gadget code using the non-cubic box configuration, and the anisotropic TreePM.

In Figure 3.1, we show a projection of the particles where the color represents the difference in acceleration according to

$$\kappa \equiv \sqrt{\frac{\sum_{i=0}^2 (a_{aniso,i} - a_{std,i})^2}{\sum_{i=0}^2 a_{std,i}^2}}, \quad (3.32)$$

where in this case a_i is the acceleration and not the scale factor. To fully satisfy the non-cubic box condition we had to slightly adjust the box as the axis ratios were not given as integers. We squeezed the box a bit more but also cut off some small number of particles which naturally leads to slightly different forces, especially close to the region where the particles would be. This introduces a difference that depends on the position and is strongest at the boundary. This is what we see in Figure 3.1.

A more quantitative view is shown in Figure 3.2 with the cumulative sum as function of κ .

As we know that the standard TreePM has a force error, we repeated the simulation, but instead of using the TreePM we used the direct summation method to calculate the

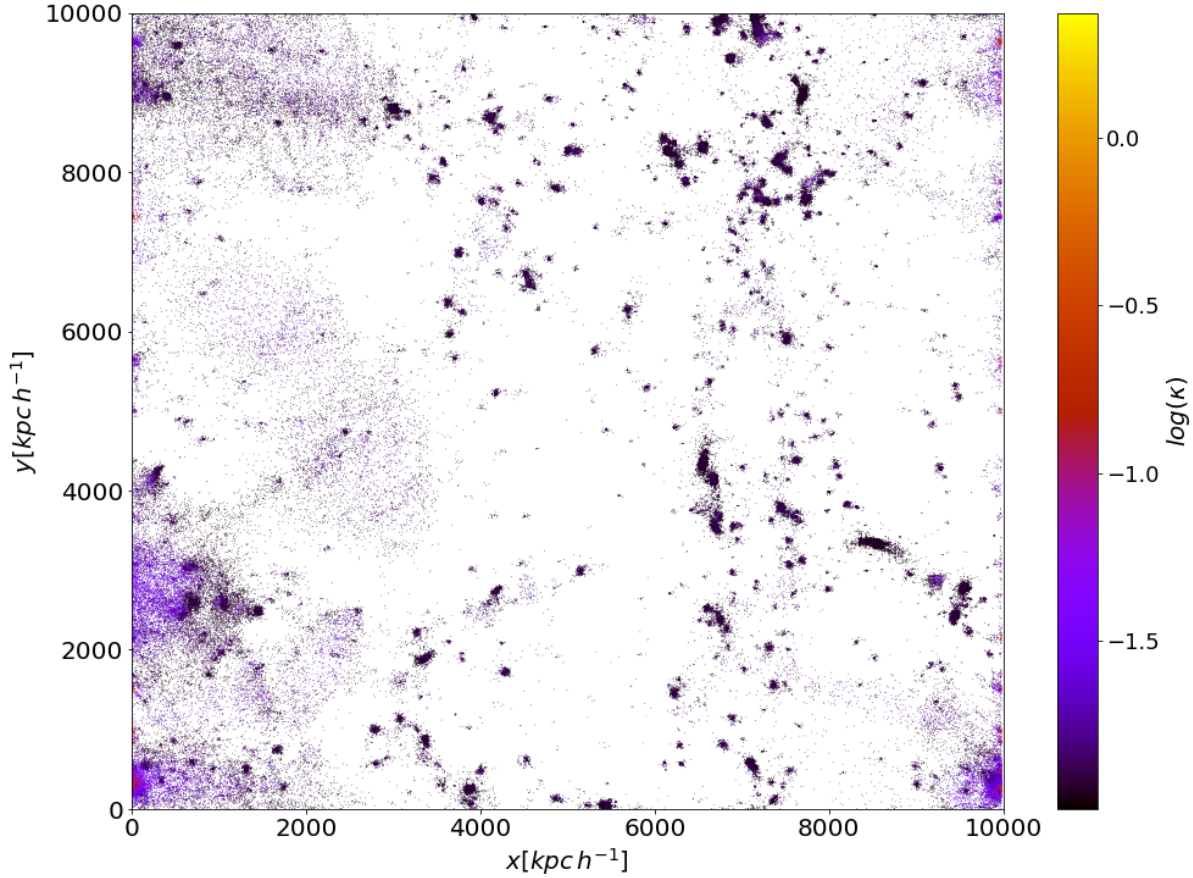


Figure 3.1: Projection for a test simulation containing only DM particles. The color shows the relative difference κ as defined in equation (3.32) for the individual particle. The range is shown on the right at the colorbar. The larger errors close to the boundary arise from the additional squeezing and cutting to fulfill the non-cubic box condition of GADGET4, $L = iL_x$, and are not due to errors in the force calculation.

accelerations. For this, we only show one axis as all three look similar. Figure 3.3 compares the accelerations of the direct summation with that of the modified TreePM. As can be seen, the bins follow the one-to-one relation which is drawn as red line. We see some scatter around the red line if all particles are plotted. The same plot (Figure 3.3) contains an inset that shows the cumulative histogram for our test value κ . In there we see that around one percent of the particles have error estimates larger than $\kappa \geq 0.5$. With this, we have a good agreement for the force calculation and are certain that we did not include errors in the implementation.

The new definitions in the TreePM for the anisotropic scale factors does however change the units of the acceleration by $\text{acc}_i^{g4} = \text{acc}_i^{\text{aniso}} \cdot \alpha_i \cdot a^2$ which has to be taken into account.

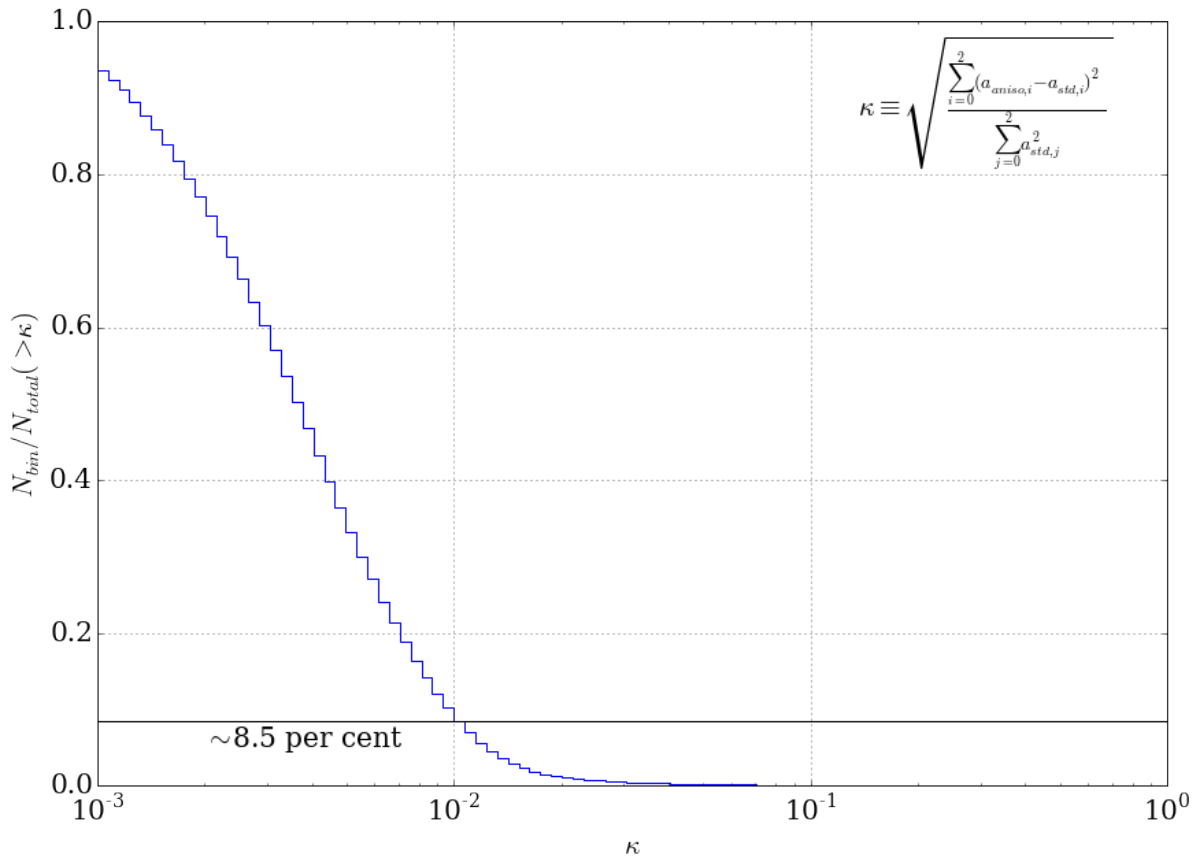


Figure 3.2: Cumulative sum histogram for the test simulation as function of κ , showing that around 8.5 per cent of the particles differ more than one per cent from the standard code. (Note that the value for the particles with a higher κ changes slightly when the bin size changes.)

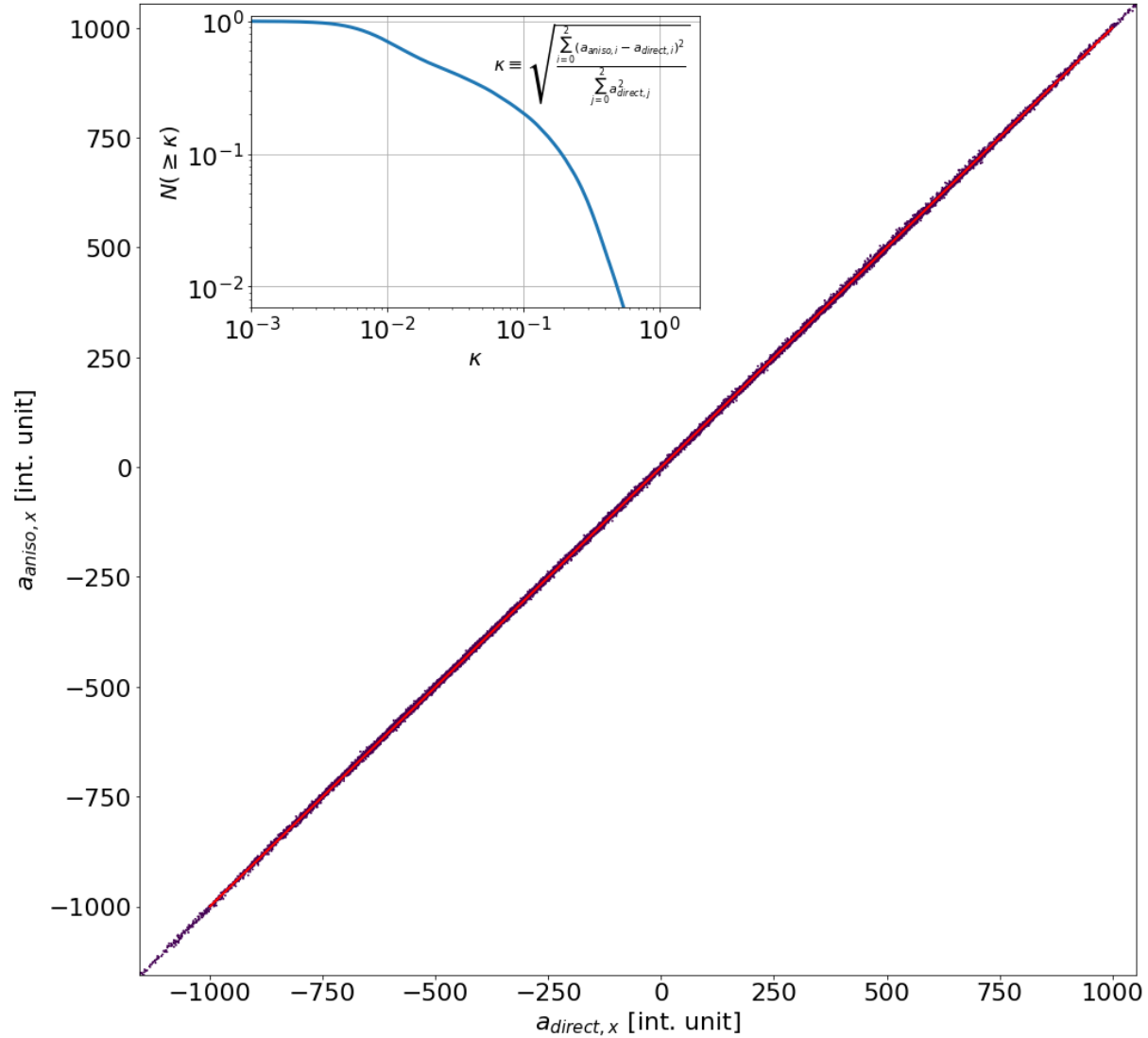


Figure 3.3: Comparison plot for the accelerations (in internal units) of the direct summation on the x-axis while the y-axis contains the acceleration of the anisotropic TreePM. The straight red line shows the one-to-one relation. For this comparison we used a run with 128^3 particles. The inlay shows the cumulative function for our test value κ , defined in equation (3.32).

3.3 Modified time stepping

In GADGET4, the particles are evolved using a standard kick-drift-kick (KDK) leapfrog algorithm where the drift (D), kick (K), and final evolution (E) operators can be derived from the EoM and are found to be (as in Springel, 2005)

$$E(\Delta t) = K \left(\frac{\Delta t}{2} \right) D(\Delta t) K \left(\frac{\Delta t}{2} \right), \quad (3.33)$$

$$D_t(\Delta t) : \begin{cases} \vec{p}_n & \rightarrow \vec{p}_n \\ \vec{x}_n & \rightarrow \vec{x}_n + \frac{\vec{p}_n}{m_n} \int_t^{t+\Delta t} \frac{dt}{a^2} \end{cases} \quad (3.34)$$

$$K_t(\Delta t) : \begin{cases} \vec{x}_n & \rightarrow \vec{x}_n \\ \vec{p}_n & \rightarrow \vec{p}_n + \vec{f}_n \int_t^{t+\Delta t} \frac{dt}{a} \end{cases} \quad (3.35)$$

with the drift and kick integrals and the force $\vec{f}_n = -\sum_j m_n m_j \nabla_n \phi(x_{nj})$. The two integrals contained in the operators have factors of a which need to be translated to the anisotropic case. The integrals transformed to the variable a used in GADGET4 are

$$I_{\text{kick}} = I_1 = \int_t^{t+\Delta t} a^{-1} dt = \int_{a(t)}^{a(t+\Delta t)} \frac{1}{a} \frac{1}{H(a)a} da, \quad (3.36)$$

$$I_{\text{drift}} = I_2 = \int_t^{t+\Delta t} a^{-2} dt = \int_{a(t)}^{a(t+\Delta t)} \frac{1}{a^2} \frac{1}{H(a)a} da, \quad (3.37)$$

which are the actual integrals solved and the index describes the power of a . Now, the scale factors can be changed to the anisotropic scale factors to find the corresponding integrals, keeping in mind that the factor $H(a)a$ is a switch from time to scale factor in the integration and is therefore unchanged. In general, the new integrals depend on the axis along which the integration is done, and the two integrals become six integrals (three for the kick and three for the drift) of the form

$$I_1 = \alpha_i^{-1} \int_{a_{\text{bg}}(t)}^{a_{\text{bg}}(t+\Delta t)} \frac{da}{H(a_{\text{bg}})a_{\text{bg}}^2}, \quad (3.38)$$

$$I_2 = \alpha_i^{-2} \int_{a_{\text{bg}}(t)}^{a_{\text{bg}}(t+\Delta t)} \frac{da}{H(a_{\text{bg}})a_{\text{bg}}^3}. \quad (3.39)$$

Under the assumption that the change in the time step for α_i is small (which is reasonable for most sensible cases of the tidal field), the α_i 's can be moved outside of the integral². By moving α from the integral, the α_i can be absorbed for the kick integral in the force calculation and we end up with the standard integral which reduces computation overhead.

²We also implemented a version where I_2 is integrated fully without that assumption, showing only a very minor difference.

3.4 Modified initial conditions

For historic reasons we used initial conditions from first order Lagrangian perturbation theory, also known as Zel'dovich approximation (Zel'dovich, 1970) in section 5.1, which are unchanged between the set of three simulations per response function measurement. This introduces an artificial evolution from $G_K = 0$ at $z = z_{\text{ini}}$ to $G_K = G_{K,\text{theory}}$ at $z = 0$, and transient effects in the evolution of the response function at high k values. To mitigate the error due to the initial conditions we calculate the corrected initial conditions of an anisotropic universe here. These are used for all simulations after 5.1. The universe expands differently from a 'standard' universe and the initial conditions need to be changed accordingly. To satisfy this, second-order Lagrangian perturbation theory (2LPT) has to be used. Following Crocce et al. (2006) and Jenkins (2010), the equations for density, displacement and velocity can be written as

$$\delta = D_1\delta^{(1)} - D_2\delta^{(2)}, \quad (3.40)$$

$$\vec{s} = -D_1\nabla_q\phi^{(1)} + D_2\nabla_q\phi^{(2)}, \quad (3.41)$$

$$\vec{v} = -D_1f_1H\nabla\phi^{(1)} + D_2f_2H\nabla\phi^{(2)}, \quad (3.42)$$

with the linear and the second order growth factors $D_1 = D$, $D_2 \approx -3D_1^2/7$, respectively, $f_1 \approx \Omega^{5/9}$, and $f_2 \approx 2\Omega^{6/11}$. The two potentials $\phi^{(1)}$, $\phi^{(2)}$ can be obtained by solving the corresponding Poisson equations

$$\nabla^2\phi^{(1)}(\vec{q}) = \delta(\vec{q})^{(1)}, \quad (3.43)$$

$$\nabla^2\phi^{(2)}(\vec{q}) = \sum_{i>j} \left(\phi_{ii}^{(1)}(\vec{q})\phi_{jj}^{(1)}(\vec{q}) - [\phi_{ij}^{(1)}(\vec{q})]^2 \right) = \delta(\vec{q})^{(2)}, \quad (3.44)$$

with $\phi_{ij}^{(1)} = \partial_i\partial_j\phi^{(1)} = H_{ij}$ the Hessian.

To account for the second order effect of the tidal field, we have to modify the Hessian H_{ij} which appears in equation (3.44):

$$\underline{\underline{H}}^*(\phi^{(1)}) = \underline{\underline{H}}(\phi^{(1)}) + \underline{\underline{\lambda}}. \quad (3.45)$$

Now, we can use the modified Hessian $\underline{\underline{H}}^*(\phi^{(1)})$ to evaluate the second order potential (equation 3.44).

$$\nabla^2\phi^{(2)}(\vec{q}) = \sum_{i>j} \left(\underline{\underline{H}}^*(\phi^{(1)})_{ii}(\vec{q})\underline{\underline{H}}^*(\phi^{(1)})_{jj}(\vec{q}) - [\underline{\underline{H}}^*(\phi^{(1)})_{ij}(\vec{q})]^2 \right), \quad (3.46)$$

The linear over-density $\delta^{(1)}$ and potential $\phi^{(1)}$ are computed using a supplied power spectrum from CAMB (Lewis & Bridle, 2002) for the given cosmology. Using the modified second order potential $\phi^{(2)}$, the displacement \vec{s} can be written as in equation (3.41) and the velocity as in equation (3.42). Further, we need to change into the correct coordinate

system by multiplying each component of \vec{s} by a factor $\alpha_i = (1 - D\lambda_i)$, so that we get the displacement field in the anisotropic frame

$$\vec{s}^* = \frac{-D_1 \nabla_q \phi^{(1)} + D_2 \nabla_q \phi^{(2)}}{1 - D\vec{\lambda}}, \quad (3.47)$$

with $\vec{\lambda} = (\lambda_x, \lambda_y, \lambda_z)$. For the velocity, the time derivative of equation (3.47) is used

$$\frac{d\vec{s}^*}{dt} = \vec{\alpha}^{-1} \frac{d\vec{s}}{dt} - \vec{s} \vec{\alpha}^{-2} \frac{d\vec{\alpha}}{dt}, \quad (3.48)$$

with

$$\frac{d\vec{s}}{dt} = -D_1 f_1 H \nabla \phi^{(1)} + D_2 f_2 H \nabla \phi^{(2)}, \quad (3.49)$$

as well as

$$\frac{d\alpha_i}{dt} = -\dot{D}\lambda_i = -f_1 D H \lambda_i. \quad (3.50)$$

Together, the velocities in the correct frame read as

$$v_i = \frac{\partial s_i}{\partial t} = \frac{-D_1 f_1 H \partial_i \phi^{(1)} + D_2 f_2 H \partial_i \phi^{(2)}}{\alpha_i} + \frac{f_1 D H \lambda_i}{\alpha_i^2} s_i. \quad (3.51)$$

The first test was to compute the response for density and position on a grid with 512^3 cells in the initial conditions. This is shown in Figure 3.4 as well as for three different choices of particle number and mesh size for the response calculation. We see a slight upturn at small scales which depends strongly on the choice of particle number (comparing the blue and magenta lines in Figure 3.4) and little on the size of the mesh cells. This should give a value that fits with that of the theoretical prediction in the linear regime. To test these new initial conditions we run them for a few time steps using the TreePM code. We choose to run a simulation with $N_p = 512^3$, particles and the box size was reduced to $100 \text{ Mpc } h^{-1}$ to increase the resolution.

The position and velocity output from the test simulation was then numerically compared to another initial condition generated with the modified IC generator at the output time of the run.

Further, we computed the response function for a subset of output time steps as shown in Figure 3.5. Here, we used a grid of 1024^3 cells for the power spectrum calculation. There, the linear regime should fit the predictions from perturbation theory at all time steps, if the velocities are correct, as otherwise the response should fall below the linear prediction (which we will see later in the PM-only results at higher redshift). The increase in G_K at small scales is an effect of the limited particle grid resolution and moves to smaller scales with more particles as shown in Figure 3.4.

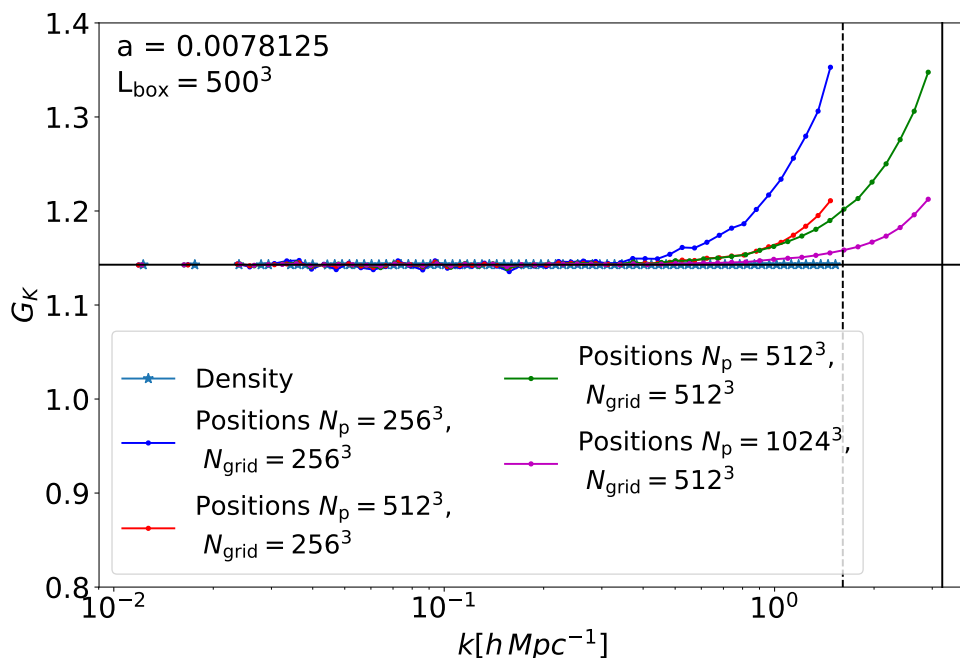


Figure 3.4: Response function calculated from the density field estimate (light blue with stars) and the positions (red, green, blue and magenta dots). The density field results in a perfect match for the response function while sampling the density field with particles introduces noise. The upturn at higher k is dependent on the particle number used as well as weakly by the number of Fourier grid cells. With a higher resolved particle grid this moves to smaller scales. This behaviour is shown by the different particle numbers. The highest particle resolution with $N_p = 1024^3$ shows the best agreement with the density for the largest range in k .

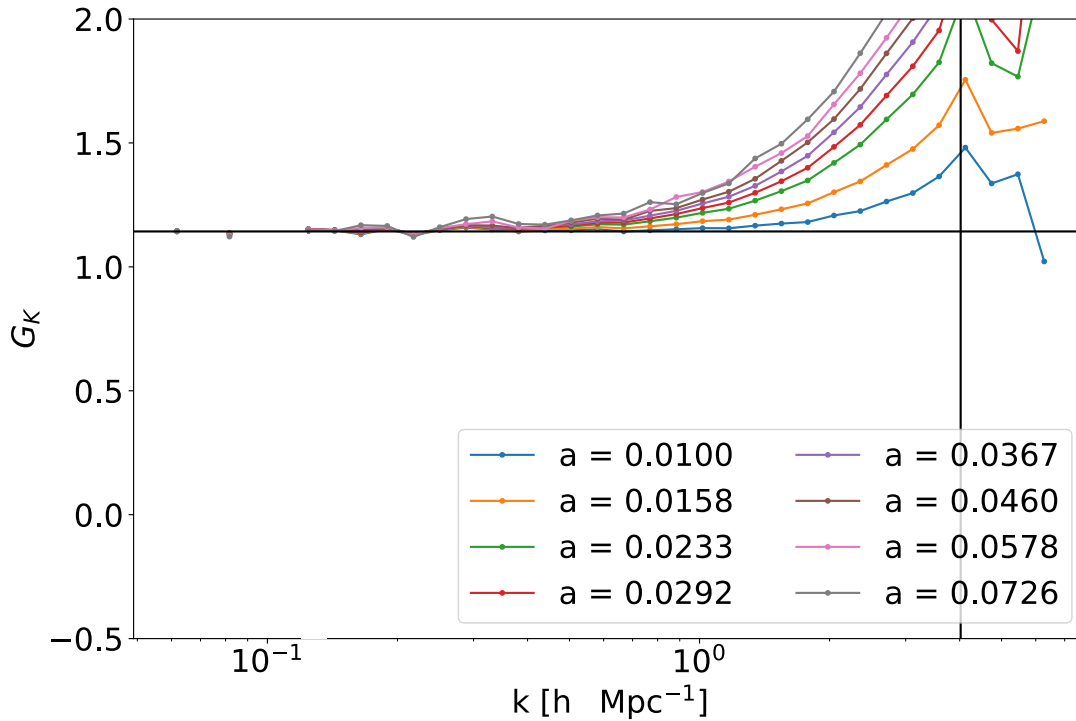


Figure 3.5: Response function for a subset of output times of our test simulation. A wrong velocity would result in response functions that stays below the linear prediction and would get closer with time. Here, we see that the response stays at the theoretical line at all sample times for sufficiently large wave numbers $k < 0.4h\text{Mpc}^{-1}$. At smaller scales, we see a bump that grows with time but is stationary in k . This increase in G_K shifts with particle number and is probably due to discreteness effects. The vertical solid black line shows the Nyquist frequency for the particle number, while the horizontal line shows the linear prediction for the response. We see two features, the first is the uprising at small scales close to the particle Nyquist frequency and secondly a bump shortly before that. We will see a bit later that this bump appears in our TreePM runs but depends on particle and force resolution. However to finalize the possible numerical origin of this feature more tests are needed.

3.5 Modified halo finder

Two interesting aspects of these “separate universe” simulations are the shapes of halos and their alignment with respect to the large-scale tidal field. For this, we first need to modify the halo finder included in GADGET4 which uses a Friend-of-Friends algorithm (FoF) (Davis et al., 1985) to identify halos. In the literature, there exist a variety of halo and subhalo finders. The interested reader is pointed to Knebe et al. (2011) for a comparison of some of the different codes available. A Friend-of-Friends halo finder looks for particles within a given distance - the linking length - and connects particles that are close enough. Those connected particles are then forming the halo and are always associated with this FoF group. However, this procedure can lead to mis-formed halos, as only the position at the specific time-step is taken into account and velocities are ignored. Hence the halo contains intruder particles that can connect the halo to other structure such as filaments. The most massive halo found in the test simulation as identified by FoF is shown in Figure 3.6. Here we see a large filament like structure instead of the usual halo that appears roughly spherical. This is one of the disadvantages of using FoF alone, which only links particles at a given separation together. To further clarify the complex structure of this group, we show a density image centered on this specific FoF group in Figure 3.7. Here we see multiple small density peaks that are also outlined by the isodensity contours. From this it becomes clear that this is not a single halo but a more complex structure that looks similar to an filament in the x-y-projection.

To avoid this a FoF is mostly used as a first step, and other methods, such as SUBFIND (Springel et al., 2001), are used to further refine the halo into substructures. An example of this is shown in Figure 3.8 that shows the FoF group from Figure 3.6 further refined into 55 subhalos. SUBFIND determines if a particle is part of a subgroup using the binding energy, the sum of potential energy and kinetic energy. If this sum of the two is larger than zero, then the particle is unbound to the subgroup but might be bound to another one. In total, this leads to three different particle types. First, the bound particles that are only associated with a single substructure; second, the particles that are not bound to any substructure; and finally the particles that are bound to at least two subhalos. Those particles then connect different substructures and are called bridging particles.

The modifications for the FoF algorithm are rather simple, as only the distance between particles has to be changed. The large-scale tidal field changes the metric of the simulation, and hence the distances that are used for linking the particles in FoF

$$\Delta x_i \rightarrow \Delta x_i \cdot \alpha_i .$$

This also includes changing the comoving linking length as the background density changes according to

$$\rho \rightarrow \frac{\rho}{\alpha_0 \alpha_1 \alpha_2} .$$

For SUBFIND, the change is similar to that of FoF. First, the distances have to be rescaled. This includes the calculation of the SPH-like density as well as the potential

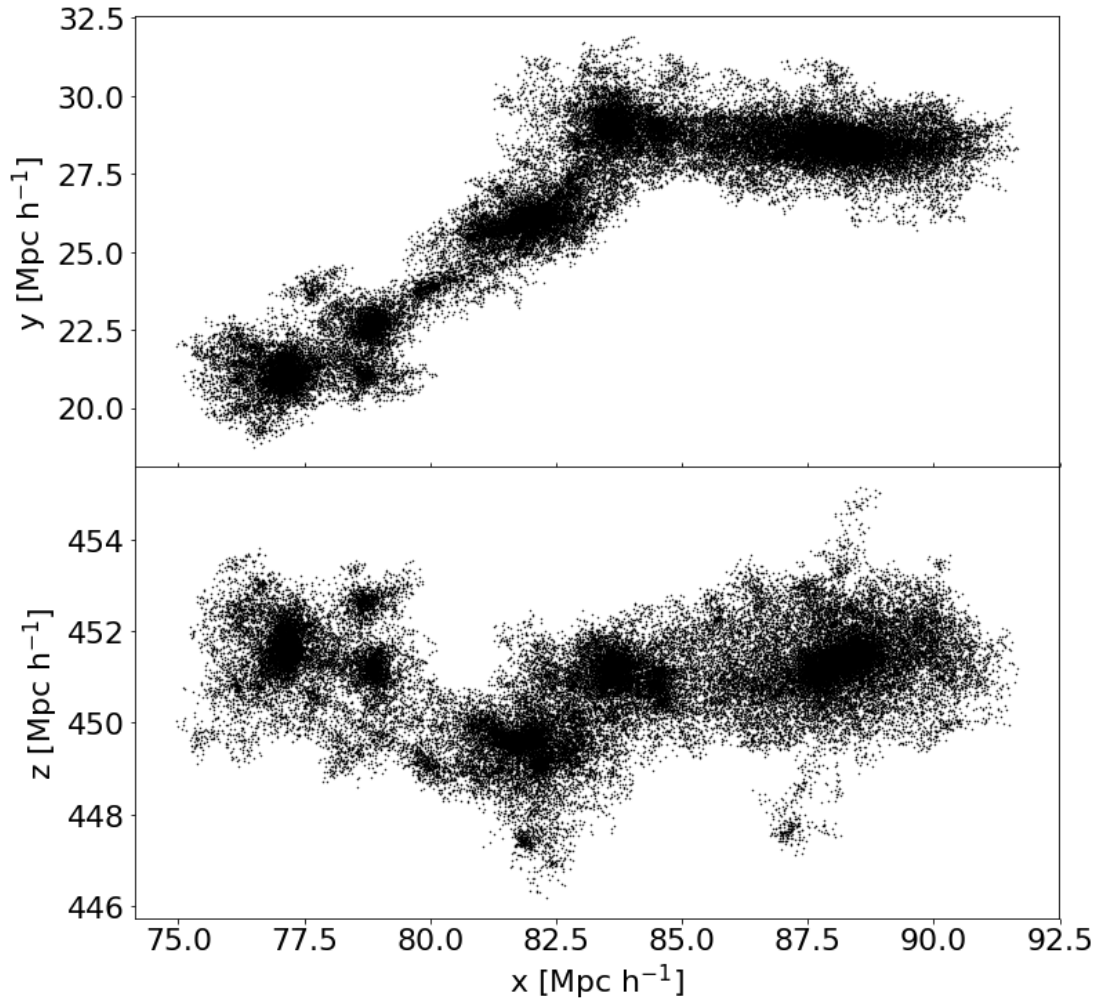


Figure 3.6: The most massive halo from a simulation that was used for testing the modified FoF and SUBFIND algorithm. The top panel shows the x-y projection, while the lower panel shows the x-z projection. In the top panel the structure resembles a filament more than a single halo. The axes show the position in the box coordinates.

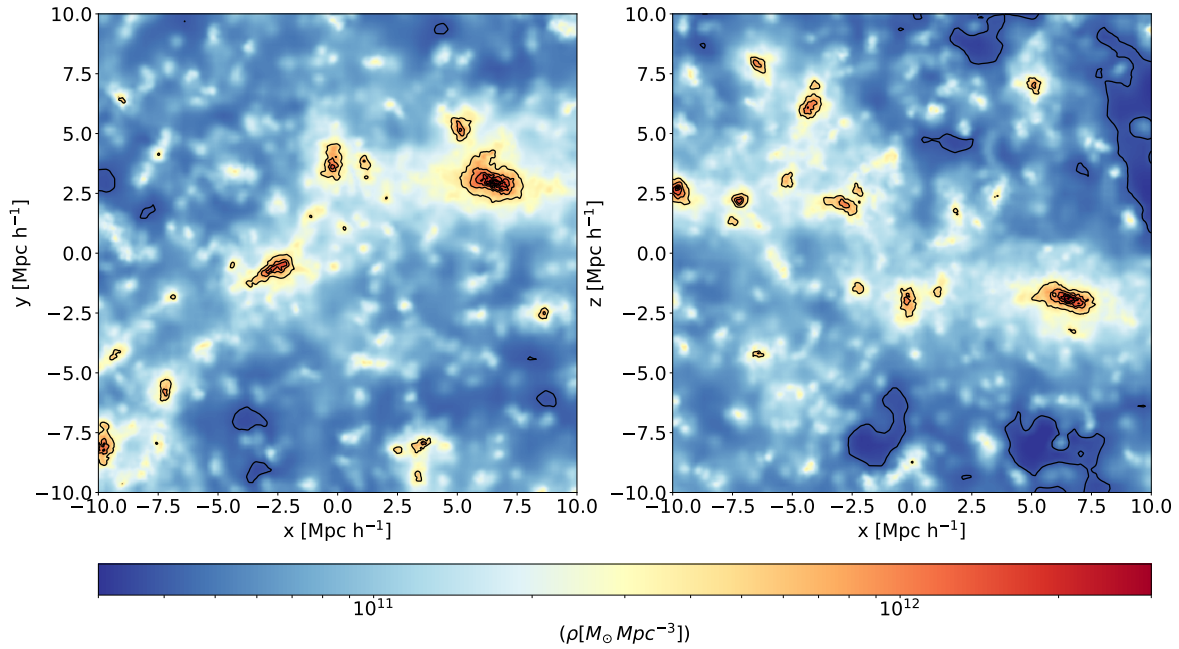


Figure 3.7: Density image of the most massive halo from a simulation that was used for testing the modified FoF and SUBFIND algorithm. Red colored regions represent high density while blue and yellow parts show the lower density structure. The density range is shown in the colorbar below the images. The x-y projection is shown on the left while the x-z projection is visualized on the right side. The contours represent density isosurfaces and are used to highlight the substructure in the group. We see that there are four to five distinguishable subhalos that are connected by lower density “filaments”. The upper right contour in the x-y projection ($x \approx 7.5$, $y \approx 2.5$) shows the most massive subhalo in this group. The axes give the distance to the center of mass of the halo.

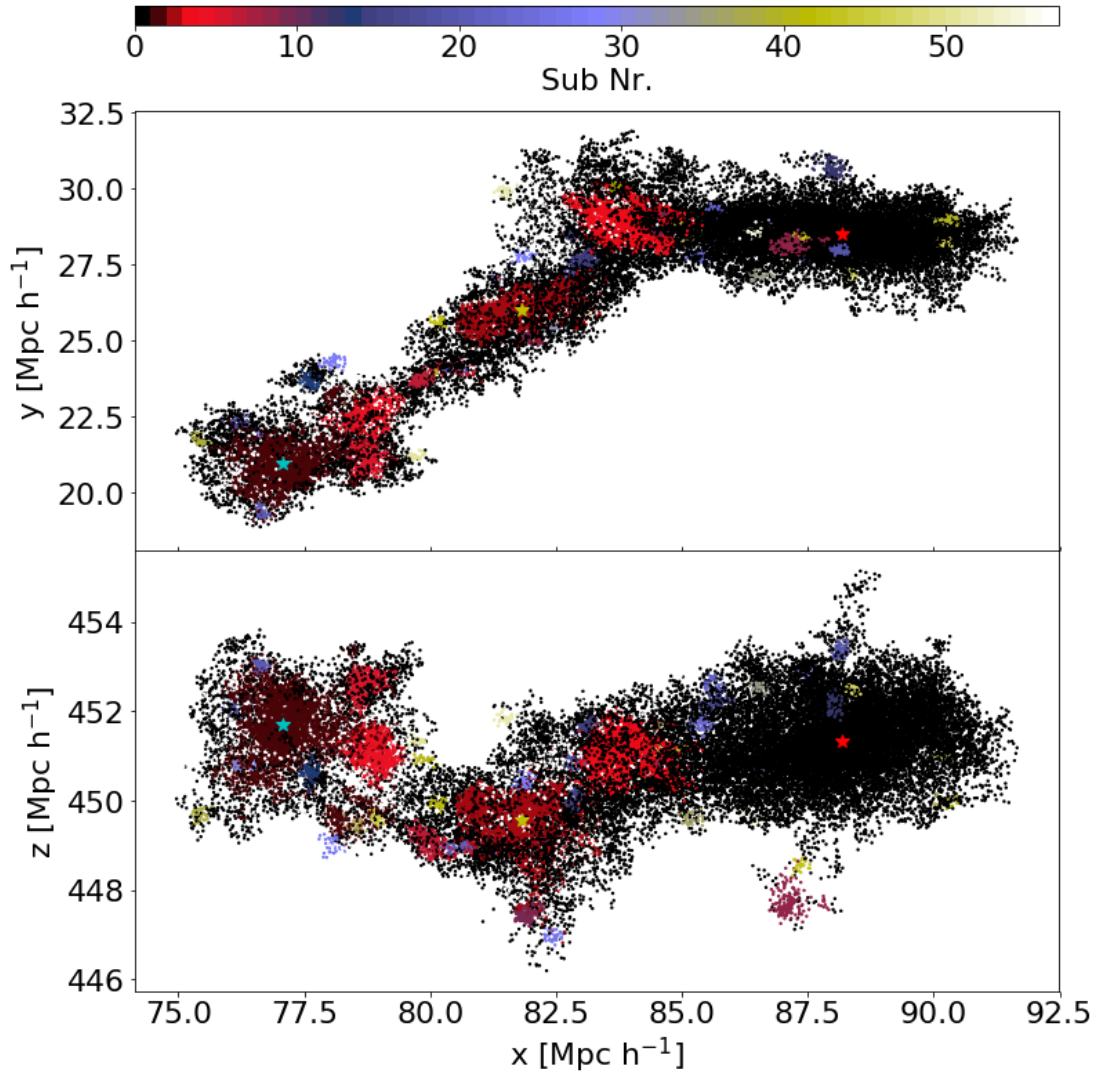


Figure 3.8: The most massive halo from a simulation that was used for testing the modified FoF and SUBFIND algorithm. The top panel shows the x-y projection, while the lower panel shows the x-z projection. The different colored points represent different substructure. In total, there are 55 subhalos. The three different colored star symbols show the position of the most bound particle for the three most massive substructures in the order red for the main subhalo, cyan and yellow for the following ones. The axes show the position in the box coordinates.

calculation. For SUBFIND, the potential is calculated using direct summation over particles found using the treewalk in a specific group. The overall background potential becomes unimportant, hence this direct summation is feasible and there is no need to include the elliptical potential equation from Section 3.2.1. Secondly, we have to change the kinetic energy, as for the unbinding of substructures the Hubble term is

$$v_{i,j,\text{Hubble}} = H(a)a(x_{i,j} - x_{i,\text{center}}),$$

for particle j , where the direction i has to be included. This term changes in the case in which we include a tidal field in our description to

$$v_{i,j,\text{Hubble}} = \left(H(a) + \frac{\dot{\alpha}_i}{\alpha_i} \right) (x_{i,j} - x_{i,\text{center}}) \cdot a_i.$$

In the case with the tidal field the distance has to be rescaled as it has been done throughout the rest of the algorithm. Further, the physical velocity relative to the center of mass is changed by

$$v_{i,j} = \frac{1}{a}(v_{i,j} - v_{i,\text{center}}) \rightarrow v_{i,j} = \frac{1}{a_i}(v_{i,j} - v_{i,\text{center}}).$$

To test the modifications a standard simulation box at $a = 1$ was used. For this box, we run FoF and SUBFIND to identify structure. The box was then copied and the second image was added to the z-axis which did extend the box in the z direction by a factor of two. This new box was then compressed along the z-axis by the factor two to again get a cubic box. The modified version of FoF and SUBFIND was used to analyze this rescaled box using the inverse scaling factor to get the original distances which then recovers the original halos. In Figure 3.9, we show the mass function of subhalos for the standard box (blue line), the first half of the rescaled box (red line) which is the original box, and the full rescaled box (green line) that contains twice the standard box. Except for some minor differences due to small errors from floating point operations while copying and compressing, the red and blue lines are identical which confirms that the modified version of SUBFIND works as intended. The green line is offset by a factor of two, as the full box contains twice the amount of halos.

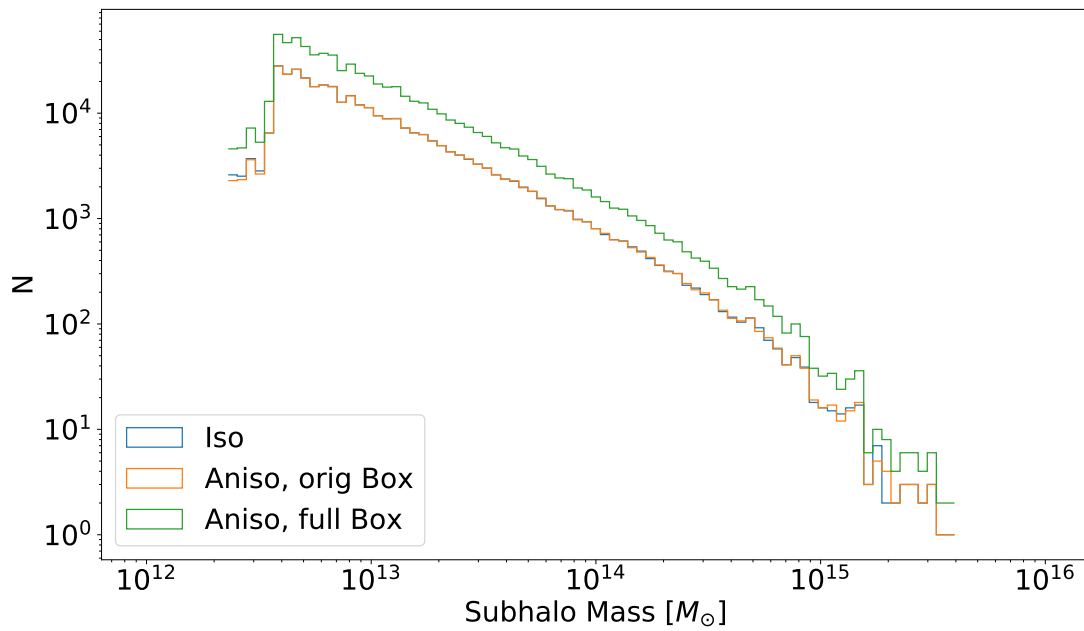


Figure 3.9: Comparison of the mass function of subhalos from the standard SUBFIND algorithm (blue) and the rescaled box using the modified algorithm (red, green). We see a slight difference that can be explained by floating point errors during the rescaling and writing of the new rescaled snapshot. The red line represents the rescaled version of the original box, while the green line that is a factor two above shows the full rescaled box. The full box contains twice the original box, hence the factor of two.

Chapter 4

Simulation setup

The following chapter describes the setup of the simulations used in this work. The first part will detail the initial conditions while the second section discusses the simulation set.

4.1 Initial conditions

The initial conditions (ICs) for the TreePM runs are constructed using the modified initial condition generator described in section 3.4. For historical reasons, the PM-only runs are using a “simpler” set of ICs which are calculated using the Zel’dovich approximation and without the influence from a large-scale tidal field. This approach leads to some transients and artifacts mainly due to the wrongly initialized velocities during the evolution which have mostly vanished at $z = 0$. For the TreePM runs, we use the second-order Lagrangian perturbation theory (2LPT) approach and take the tidal field into account by modifying the positions and velocities. This leads to a set of three ICs per response measurement where the difference would go to zero at a very high starting redshift. To overcome the issue of the cosmic variance due to the finite volume, we generate eight different realizations of the density field. In Table 4.1 we show the basic properties of the ICs used throughout this work. The first entry, where 2LPT is crossed, gives the data for the ICs of the PM-only runs. Those were generated using NGenIC (Springel et al., 2005b) adopting an initial powerspectrum from CAMB (Lewis & Bridle, 2002). The mass resolution for the simulations is given by the matter density parameter in Table 4.2, the used boxlength, and the number of particles. For the runs in the $500 \text{ Mpc } h^{-1}$ box, this leads to a mass resolution of $m_p \approx 7.96 \cdot 10^{10} M_\odot h^{-1}$, and for the smaller box to a value that is smaller by a factor of $(L_{\text{box},l}/L_{\text{box},s})^3$, namely $m_p \approx 0.0637 \cdot 10^{10} M_\odot h^{-1}$ for the $100 \text{ Mpc } h^{-1}$ box.

To separate effects coming from the tidal field from those due to large-scale density offsets, we limit ourselves to simulations with $\sum_i \lambda_i = 0 = \delta_L$ (traceless), where the λ_i are the eigenvalues of the linear deformation tensor and δ_L is the linear overdensity at $z = 0$ for the runs including a tidal field. With this choice contributions from R_1 are excluded, since this part of the response is sourced by the overdensity. Effects from a large-scale

| a_{ini} | λ_x | λ_y | λ_z | 2LPT | L_{Box} [Mpc h^{-1}] | N_{part} | N_{real} | Label |
|-----------|-------------|-------------|-------------|------|----------------------------------|-------------------|-------------------|-------|
| 0.0078125 | 0.0 | 0.0 | 0.0 | × | 500 | 512^3 | 16 | |
| 0.0078125 | 0.0 | 0.0 | 0.0 | ✓ | 500 | 512^3 | 8 | 0 |
| 0.0078125 | -0.05 | -0.05 | 0.1 | ✓ | 500 | 512^3 | 8 | A |
| 0.0078125 | 0.05 | 0.05 | -0.1 | ✓ | 500 | 512^3 | 8 | B |
| 0.0078125 | 0.0 | 0.0 | 0.0 | ✓ | 100 | 512^3 | 1 | 0 |
| 0.0078125 | -0.05 | -0.05 | 0.1 | ✓ | 100 | 512^3 | 1 | A |
| 0.0078125 | 0.05 | 0.05 | -0.1 | ✓ | 100 | 512^3 | 1 | B |
| 0.0078125 | 0.0 | 0.0 | 0.0 | ✓ | 250 | 512^3 | 1 | 0 |
| 0.0078125 | -0.05 | -0.05 | 0.1 | ✓ | 250 | 512^3 | 1 | A |
| 0.0078125 | 0.05 | 0.05 | -0.1 | ✓ | 250 | 512^3 | 1 | B |

Table 4.1: The basic properties of the initial conditions used in this work. The first column shows the initial scale factor a_{ini} at $z = 128$, followed by the eigenvalues ($\lambda_x, \lambda_y, \lambda_z$) of the deformation tensor Π_{ii} . The fifth column shows which kind of IC generation was used. The sixth and seventh column gives the boxsize in $\text{Mpc } h^{-1}$ (comoving Mpc) and the number of particles (N_{part}), respectively. The eighth entry shows the number of realizations (N_{real}) used, and the last one is a label corresponding to the one used in equation (2.35).

| Ω_m | Ω_Λ | Ω_b | σ_8 | h |
|------------|------------------|------------|------------|-------|
| 0.308 | 0.692 | 0.04694 | 0.829 | 0.678 |

Table 4.2: The important cosmological parameters used for generating the initial conditions.

overdensity were already discussed in Wagner et al. (2015a); Wagner et al. (2015b) and the interested reader should follow these publications as well as the citations within. The ICs with labels A and B are symmetric in their eigenvalues and are used to reduce the error in the measurement of the response function (equation 2.35).

For all ICs, we use a flat Λ CDM cosmology using the Planck 2015 results (Planck Collaboration et al., 2015) with a subset shown in Table 4.2. The Ω_i are the density parameters that define the density of the given component relative to the critical density $\rho_c = 3H_0^2/(8\pi G)$, h is parameterization of the Hubble constant by $H_0 = 100 h \text{ km } s^{-1} \text{ Mpc}^{-1}$, and σ_8 is the RMS linear mass fluctuation at a scale of $8\text{Mpc } h^{-1}$ extrapolated to $z = 0$. The last six simulations in Table 4.1 are smaller volume simulations, which increases the resolution of the force calculation, as well as the powerspectrum computation. This allows us to check for resolution effects for the force calculation in the runs including the tidal field and some minor issues that might arise from the folding of the power spectrum.

The simulations use the parameters defined in Table 4.3, where we list the most important ones. The parameter ‘‘ASMTH’’ controls the scale at which the force split happens, ‘‘RCUT’’ defines the maximum radius up to which the short range force is computed, where ‘‘RCUT $\gg 6$ ’’ should not yield better results in regards of treating the force matching re-

| | | | | |
|-----------|------|----------------|-------------------|--------------------------------|
| Parameter | PM | ASMTH | RCUT | ErrTolForceAcc |
| Value | 1024 | 1.5 | 6.0 | 0.01 |
| Parameter | | ErrTolThetaMax | ErrTolIntAccuracy | $\epsilon[\text{Mpc } h^{-1}]$ |
| Value | | 0.6 | 0.01 | 0.04 |

Table 4.3: Main parameters used for the simulations.

gion (Springel, 2005). The “ErrTolForceAcc” and “ErrTolThetaMax” parameter define the accuracy of the relative opening as described in section 4.2.2. “ErrTolIntAccuracy” provides the precision of the kinematic time step constraint which gives an upper limit for the time step of the particle.

4.2 Simulation set

We use a set of simulations including different realizations of the initial density field to reduce the influence of cosmic variance. To compute the response, for each initial density field realization we need a set consisting of three simulations. The standard run, which does not include a tidal field, and two runs including a tidal field with inverted sign of the eigenvalues $\lambda_{i,A} = -\lambda_{i,B}$. In the following we describe how the PM-only run is affected by different grid and hence force resolutions. This problem does not arise in the TreePM runs down to smaller scales. To test for issues that arise from force resolution in the TreePM, we also include a single realization of the initial density field in a smaller box, keeping the same number of particles.

In the following we show a set of convergence tests that allow us to understand the influence from parameters of the simulation. The first part deals with the pure PM-only simulations while the second one highlights the convergence of the TreePM runs. Here we mostly show a single realization except for the PM-only case as these are fast to compute.

4.2.1 Convergence PM-only

In order to see the convergence and the scale where resolution effects become important, we run two more sets with the same particle number and initial conditions but with different PM resolution. The first set has 512^3 cells, while the second has 1024^3 cells. The comparison can be seen in Figure 4.1 and Figure 4.2, where we show the one-dimensional power spectrum and response function, respectively, for each force resolution. The response function and power spectrum are computed using a Fourier grid of 1024^3 cells that is unchanged for all PM resolutions. We note that the power spectra and response functions of such pure PM simulations do not vary monotonically as the resolution is changed. This produces the offset in the response function for the 1024^3 cell run compared to the other two force resolutions. This is also true for the one-dimensional power spectrum (Figure 4.1), which shows that changing the force resolution (PM grid size) influences the power

spectrum. The 512^3 and 2048^3 cell runs agree well on most scales while the 1024^3 cell simulation is above both of them for scales with $k \geq 6 \cdot 10^{-2} h \text{ Mpc}^{-1}$. We see that the response function agrees for all three force resolutions up to $k \sim 1.3 h \text{ Mpc}^{-1}$ at roughly the ten percent level. However, larger departures are seen on smaller scales (higher k), most likely due to anisotropic force-softening effects.

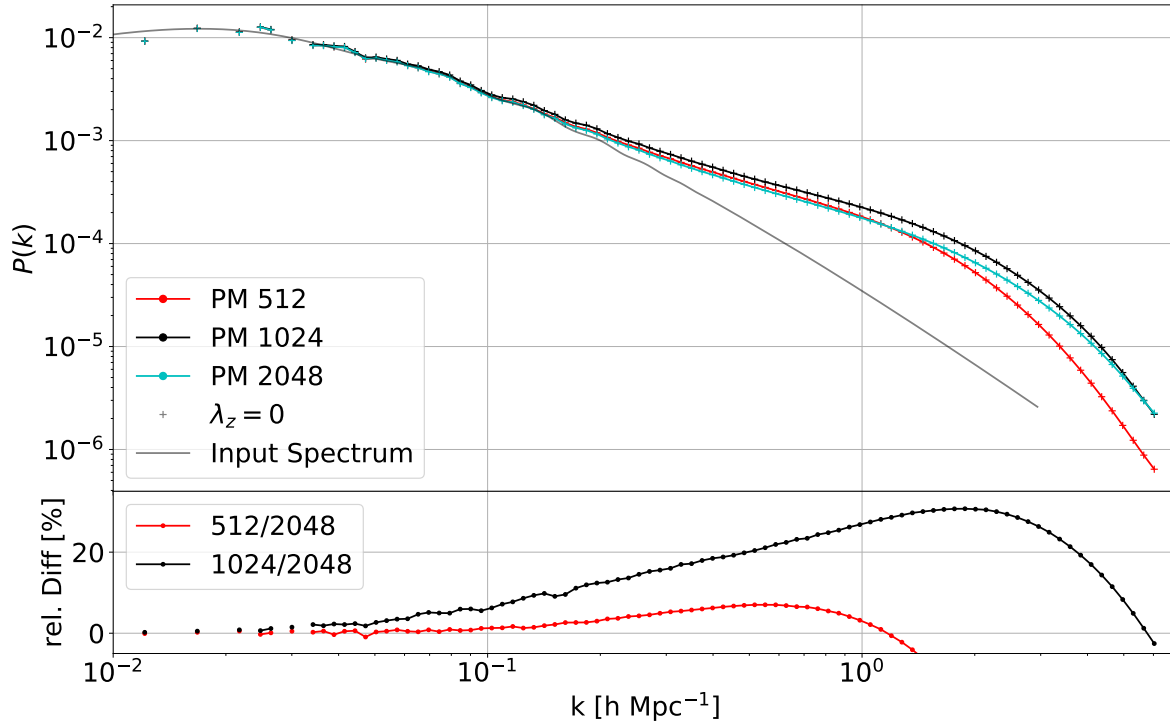


Figure 4.1: Comparison of the effect of different PM grid resolutions on the convergence for the one-dimensional power spectrum. We only show the $\lambda = 0$ case, as in the one-dimensional power spectrum all three λ cases are identical. All runs were performed using a 512^3 particle grid. In the upper plot we show the mean and rms scatter from the 16 realizations as symbols and errorbars, respectively. The fiducial PM resolution of 2048 is shown as cyan symbols, while the 512 and 1024 are shown as red and black, respectively. The grey line represents the input power spectrum for the initial conditions rescaled using the linear growth factor and is only plotted to $k \sim 3$. In the intermediate regime ($10^{-1} \leq k[h \text{ Mpc}^{-1}] \leq 1$), the highest resolution drops in power below the smallest resolution. The intermediate resolution is above both other resolutions for most of the scales and converges with the other resolutions at small k . The lower panel shows the relative difference in percent between the smaller resolutions to the fiducial 2048 one. On intermediate scales, the case of 1024 cells per axis shows a significant difference compared to both the lowest and highest resolved runs.

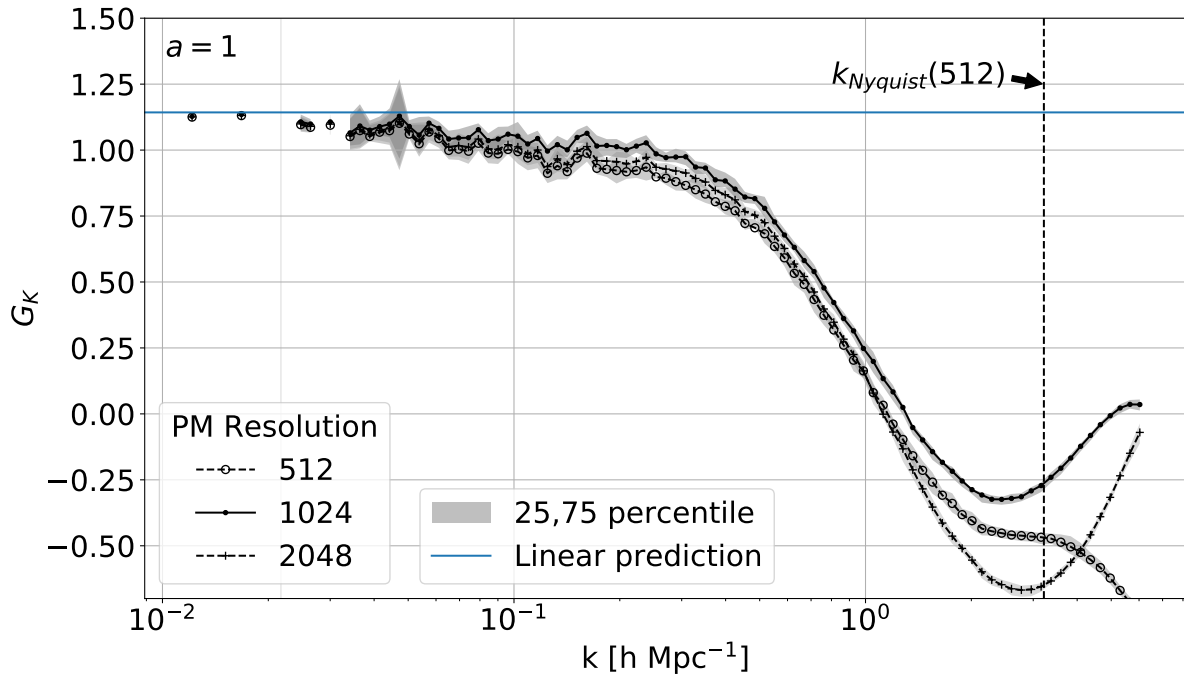


Figure 4.2: Comparison of the average from 16 realizations for three sets of simulations with varying PM grid cells. The filled and open circles represent the mean of the (1024^3) and small (512^3) grid, respectively. Furthermore, the crosses show the fiducial 2048^3 grid for the PM calculation. The shaded areas represent the 25th to 75th percentiles for each set of 16 realizations. The horizontal blue line shows the linear prediction from Akitsu et al. (2017). The vertical black dashed line ($k \sim 3.$) represents the particle Nyquist frequency, which is also the Nyquist frequency for the smaller PM grid.

| Parameter/Name | ASMTH | ErrTolForceAcc | ErrTolThetaMax | PM size |
|----------------|-------|----------------|----------------|---------|
| ASMTH15 | 1.5 | 0.01 | 0.6 | 1024 |
| ASMTH25 | 2.5 | 0.01 | 0.6 | 1024 |
| ForceAcc | 1.5 | 0.001 | 0.6 | 1024 |
| ForceTheta | 1.5 | 0.01 | 0.4 | 1024 |
| PM2048 | 1.5 | 0.01 | 0.6 | 2048 |

Table 4.4: Overview of parameters changed in the convergence test runs for the TreePM. The first column contains the name of the simulation run while the following list the corresponding parameters as defined in the first row.

4.2.2 Convergence - TreePM

As our simulations are suffering from a multitude of possible choices for parameters, we tested some of them that have an influence on the force accuracy. Those runs are not using the proper initial conditions but are meant to test the TreePM convergence. For that reason, the simulations are not run until $a = 1$, as the convergence can be tested even at an earlier time step. The parameter “ASMTH”, for which we expect a slightly larger difference, controls the scale where the force split between the PM and Tree force occurs. As we have seen in the previous section, a different PM mesh can have an impact, at least in the PM-only case, so we run a test using a twice as large grid for the PM part in the TreePM simulation. The “ErrTolForceAcc” defines the allowed error in the relative opening criteria (see also section 1.3.1) for the tree walk and “ErrTolThetaMax” limits the maximum opening angle in the relative opening criteria. The test runs also allow us to find the parameters where the simulation runs fast as well as with good precision. The result for these runs is shown in Figure 4.3, which shows that the force and angle parameters have nearly no influence on the result. Using a larger PM grid, one would normally also change the “ASMTH” parameter in order to reach a similar force cut. Here, we see that changing only the PM mesh, there is a slight shift in the response function, opposite to the increase of the “ASMTH” parameter. Overall, the runs show only minor differences and the general shape is identical.

To avoid effects of the limited resolution, we test our one-dimensional power spectrum against that measured in the Millennium (Springel et al., 2005b) and Millennium II (Boylan-Kolchin et al., 2009) simulations. In our runs, we account for the shot noise at small scales, which leads to a changing logarithmic slope at the smallest scales. The shot noise is usually modeled - for the nearest neighbor (NGB) mass assignment - as the inverse of the particle number N_p

$$P_{shot} = N_p^{-1}, \quad (4.1)$$

which is also the value the uncorrected power spectrum approaches and flattens at. Using the CIC mass assignment we correct the shot noise using the approximation (e.g Cui et al.,

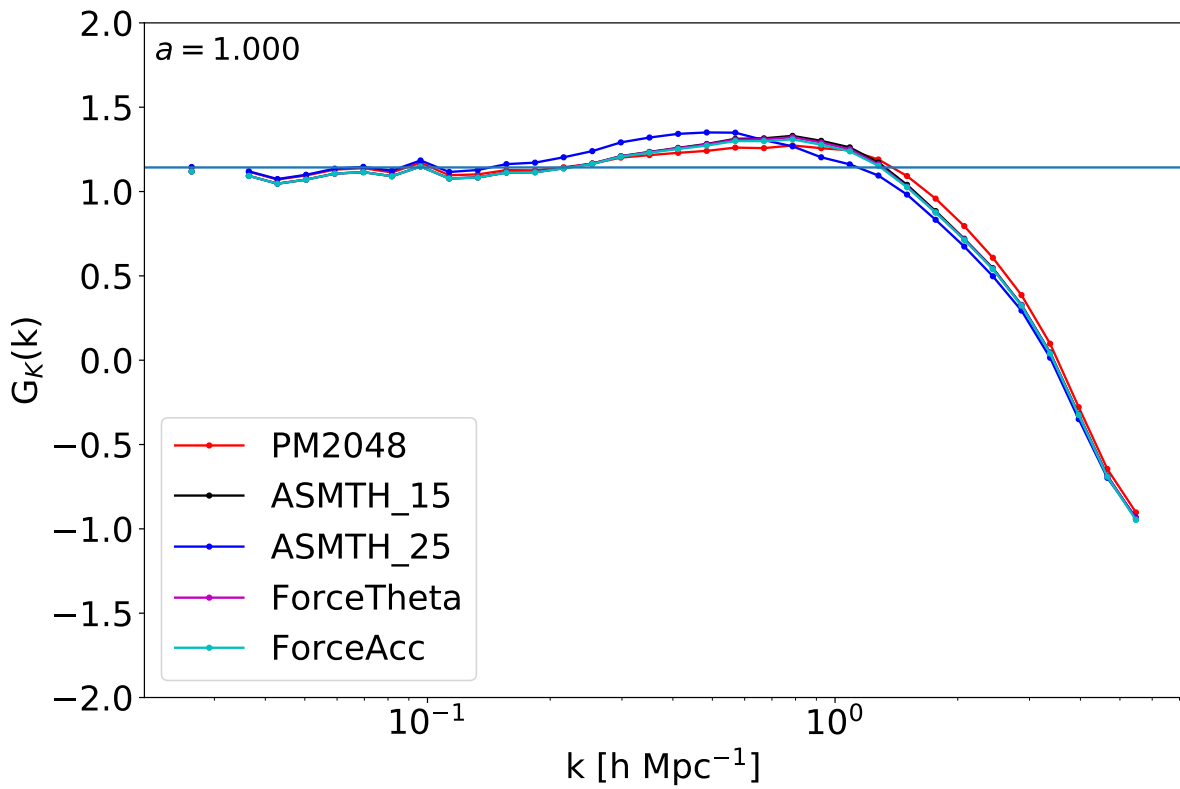


Figure 4.3: The response function for the five different models described in Table 4.4. They agree reasonably well with the small exception of $\text{ASMTH} = 2.5$, which is expected. We see minor differences but the overall trend is identical.

2008)

$$P_{shot} \approx \frac{1}{N_p} \left(1 - \frac{3}{2} \sin^2 \left(\frac{\pi k}{2k_{Nyq}} \right) \right), \quad (4.2)$$

with the Nyquist wave number k_{Nyq} . This is in contrast to the Millennium runs, where the slope stays roughly constant at $d \ln(P)/d \ln(k) \approx -2$. Correcting for the shot noise in the Millennium simulation ($P_{shot} = N_{p,MS}^{-1}$), we see the same change in the gradient. Since the simulations have a limited mass resolution, the missing power on the smaller scales is probably due to the missing modes that are not resolved and would contribute to the power on these scales. It also appears that the shot noise masks this effect for a short range in k . Comparing our simulation with the Millennium run, we can estimate the limiting scale up to which we can measure the response. This cut-off scale is estimated to be around $k \leq 15h \text{ Mpc}^{-1}$, where the one-dimensional power spectrum from the Millennium and our simulations agree. This is shown in Figure 4.4, where we see that our runs agree with the better resolved Millennium simulation up to the given scale.

It should be noted that we only accounted for the different normalization of the power spectrum, not the change in cosmology from WMAP to Planck. This would introduce an additional small shift in k and does not affect our conservative choice of the cut-off scale. In addition, we use two different mass assignments for the power spectrum calculation to get a handle on the effect of the choice. Here, we see no difference between the NGP and CIC power spectrum, after taking the de-convolution into account, also including the shot noise¹. To further test the behavior, we run two sets of simulations with a five-times smaller side length and half the side length. This increases the mass resolution by a factor of 5^3 (2^3) while the softening ϵ used is a factor of 5 (2) smaller. Due to the higher resolution, the densities are also higher, and therefore the runs became slower. For this reason, we choose to run a single realization for these boxes. This allows us to better understand the response and the convergence at large k . In this regime, the missing power on smaller scales leads to a declining one-dimensional power spectrum in our fiducial boxes, which in turn leads to a declining response. Under the, as we will see, bad assumption that the tidal field does not change the shape of the halo in physical space, we expect that the growth-only response approaches $d \ln(P)/d \ln(k)$ as the full response should approach zero. This value, however, changes in our standard box due to the missing power, as can be seen in comparison to the better resolved Millennium-II simulation.

In the following results section, we show the G_K measurements for the TreePM up to $k \leq 20h \text{ Mpc}^{-1}$. The limited resolution effect will also happen in our better resolved runs with the smaller box sizes, and we expect to see a difference at small scales with $k \gtrsim 20h \text{ Mpc}^{-1}$, which should also affect the response function. The only part where the shot noise correction is important is the denominator of equation (2.35) and therefore we expect a flattening of the decline in G_K as the power is larger at a given k .

In Figure 4.5, we show the response function at $z = 1.89$ of the small box compared

¹Note that this is not necessarily true for smaller scales.

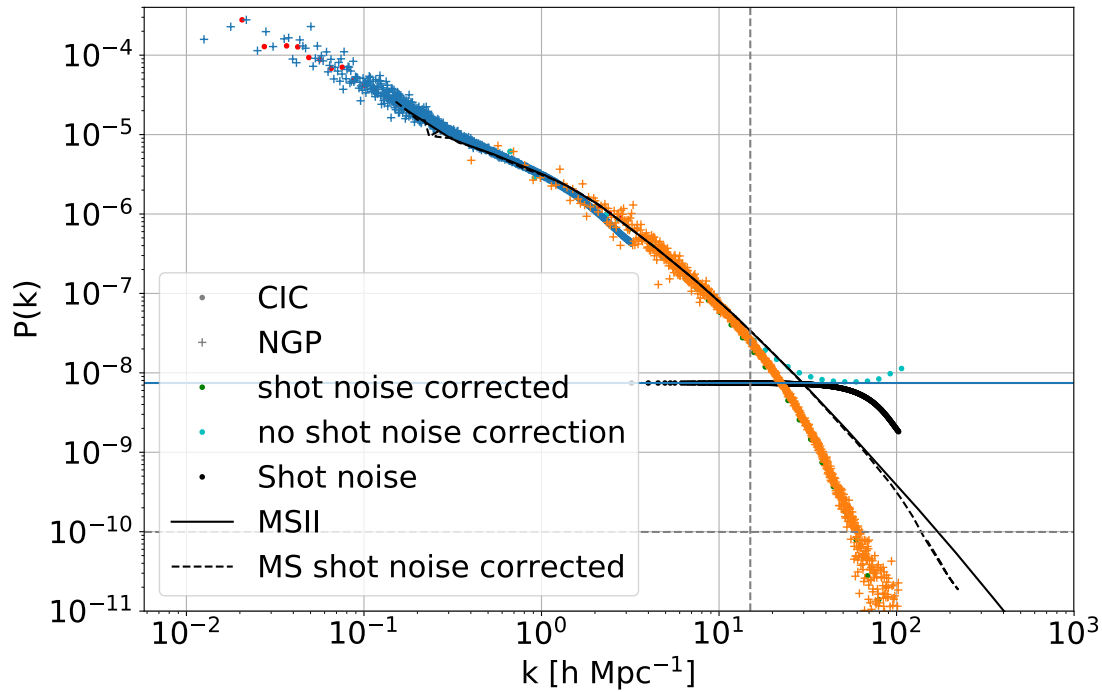


Figure 4.4: One-dimensional power spectrum compared to the one measured from the Millennium (black dashed line) and Millennium II simulations (black solid line). To account for uncertainties from the mass assignment, we additionally compare CIC (dots) and NGP (crosses), which agree in the range where the power spectrum can be reasonably measured. The solid blue horizontal line illustrates the shot noise for the NGP, while the black dots are the shot noise for the CIC for our particle number and the gray dashed horizontal line represents the shot noise for the Millennium simulation. The cyan dots display the power spectrum without the shot noise correction, which shows the level of the shot noise. In this test, the grid for the power spectrum calculation was 512^3 . The vertical dashed line shows the value of $k = 15 h \text{ Mpc}^{-1}$ as a reference point.

to our standard run. We see a clear difference between the runs on small scales ($k \gtrsim 3.7h \text{ Mpc}^{-1}$), while at large scales the noise for the smallest volume is rather large (no average over multiple initial conditions and fewer modes). We see that at large scales all three boxes agree while at smaller scales the slope of G_K changes towards a flatter decline. Probably this change comes from smaller scales coupling to larger scales and transfer power which increases the power for the power spectrum in the denominator of equation (2.35). Further we show the $a = 1$ measurement for the $250\text{Mpc}h^{-1}$ box that agrees with our larger volume at around 10 per cent difference. Here the decline of the response function is a bit slower for the smaller box and the step decline happens at smaller scales.

4.3 Halo finding

To compute the shape and alignment of halos we first need to identify these objects in our simulations. For this we use the modified halo finder from section 3.5 on a single realization taken at random from the eight simulation sets of the TreePM runs. We then identify halos with more than 32 particles that can be linked together using a linking length of 0.2 times the mean particle separation. This provides us with the backbone to refine the groups further into substructures. For the decomposition into substructure, we use the SUBFIND algorithm which identifies subgroups by computing the binding energy for each particle (see section 3.5 for details). For the substructure we set the condition that at least 20 particles have to be bound to the subhalo, otherwise it is discarded. The number of halos and subhalos can be found in Table 4.5. For the standard simulation we found 102244 halos and 106256 subhalos in total, while for the two tidal field runs with $\lambda_z = 0.1$ (-0.1) we identified 102219 (102170) halos and 106132 (106096) subhalos, respectively.

| λ_z | N_h | N_{sub} |
|-------------|--------|------------------|
| 0 | 102244 | 106256 |
| 0.1 | 102219 | 106132 |
| -0.1 | 102170 | 106096 |

Table 4.5: Number of halos N_h and subhalos N_{sub} for the three different simulations in the random set.

The numbers being close to each other also shows that, to first order, the tidal field does not change the halo numbers. SUBFIND also computes a variety of properties for the subgroups, e.g. the virial radii for different definitions, some of which are used (e.g. R_{vir}) and others that are not important to us. To fully use all subhalo properties we need to further check if these are probably modified, if needed, which has not been done in this work.

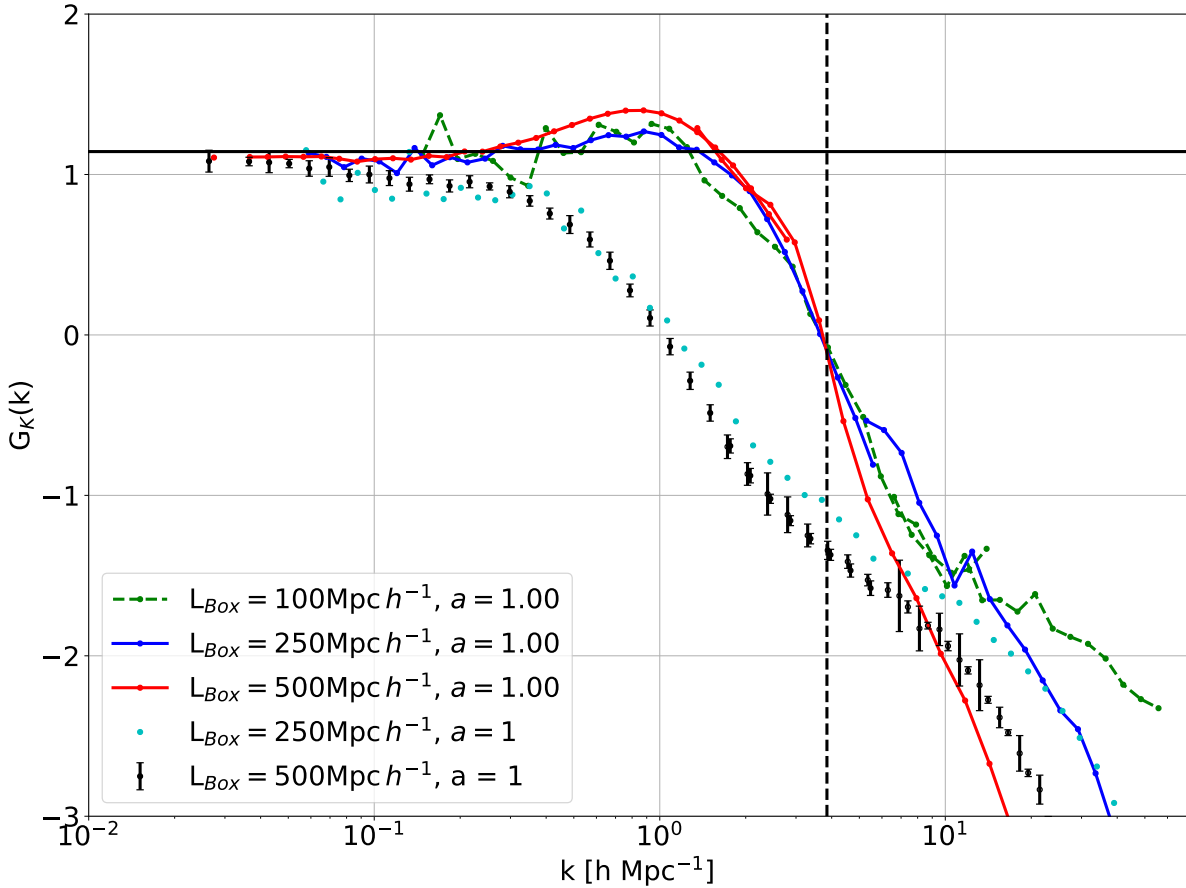


Figure 4.5: The response function for three different mass resolutions. The run shown as a blue line has a box length of $L_{box} = 250 \text{Mpc } h^{-1}$, while the red line shows the result for our standard runs with $L_{box} = 500 \text{Mpc } h^{-1}$. At large scales, the smaller volume agrees with the standard box but has slightly more noise due to the single realization. At smaller scales ($k \gtrsim 3.7 h \text{Mpc}^{-1}$, vertical dashed line) we see a clear difference which most likely comes from the better resolved small scales. The interesting bump at around $k > 1 h \text{Mpc}^{-1}$ decreases with the smaller volumes. We interpret this as being an artifact rather than a physical effect. Additionally we also show the smallest box as green dashed line which overall agrees with the intermediate box size (blue line). However, the smallest volume starts at scales around the rise to the bump and therefore is inconclusive with respect to the bump. On smaller scales, the $100 \text{Mpc } h^{-1}$ box again deviates from that with the intermediate box size. So the decline at $k \gtrsim 3.7 h \text{Mpc}^{-1}$, that can be seen in the response function at $a = 1$, which is shown as black dots with errorbars is probably due to the limited resolution. The cyan points represent the intermediate box at $a = 1$ which can be compared to the black points with errorbars. We see that the overall shape is similar and they agree with a 10 per cent difference. For scales with $k > 1 h \text{Mpc}^{-1}$ we see that the smaller box declines slower than the larger box which follows the trend observed at higher redshift.

Chapter 5

Results

In the following chapter we show the results of the full set of simulations. The first part focuses on the PM-only simulations which was published in Schmidt et al. (2018). In the previous chapter we saw some of the results from a single realization which were used to investigate the convergence. Here, in comparison, we show the results obtained by the full set of runs.

5.1 PM-only simulations

The first set of simulations was run using only the PM to compute the gravitational acceleration. There we are not able to probe the highly nonlinear regime and are limited to values of $k \leq 2h \text{ cMpc}^{-1}$ which we denote as the mildly nonlinear regime. The first check is the comparison of the one-dimensional power spectrum which should be identical for all three simulation of a given set. This is shown in Figure 5.1 where the lower panel shows the relative difference to the isotropic case. The difference is around one per cent which is the expected value for higher order terms in K_{ij} (e.g. $(K_{ij})^2$). The single point with higher difference in Figure 5.1 has a statistical origin, as fewer modes are contained in this bin compared to the surrounding bins. This explains the larger errorbar as well, which represents the standard deviation in the given bin with regard of the realizations.

5.1.1 Response Function

Since the resolution of the PM mesh does not allow for detailed information about halo structure we limit ourselves for the PM-only runs to the analysis of the response function. Figure 5.2 contains all results in a single plot. At large scales the growth-only response function G_K (black dots with errorbars) shows the expected behavior following the theoretical prediction of

$$G_{K,\text{theo}} = \frac{8}{7},$$

shown as blue line in Figure 5.2.

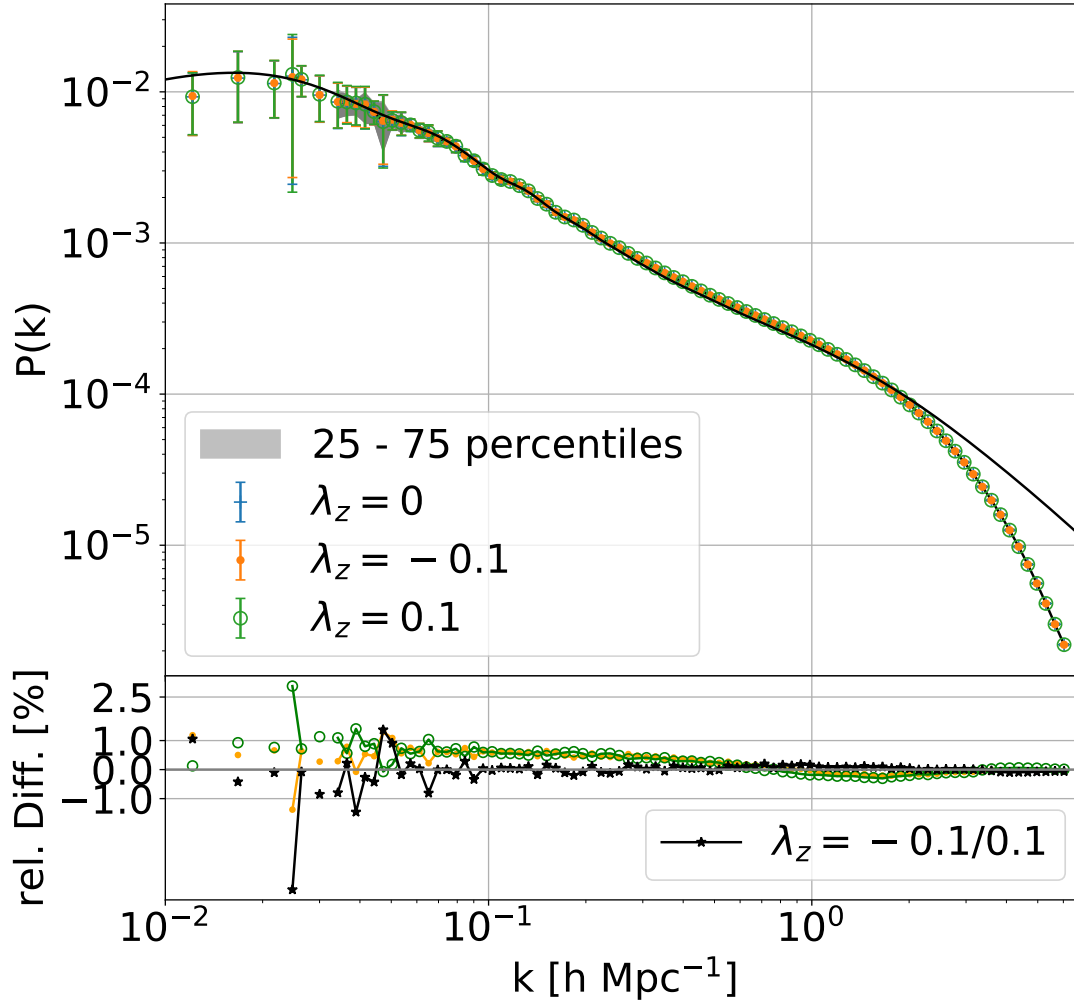


Figure 5.1: The upper panel shows a comparison of the one-dimensional (i.e., angle-averaged) power spectrum for the three simulations using different tidal fields. The symbols show the mean with errorbar giving the rms scatter among the realizations. Open circles show the case $\lambda = (-0.05, -0.05, 0.1)$, while black dots are for $\lambda = (0.05, 0.05, -0.1)$, and crosses are for runs with no tidal field. The lower panel shows the relative difference between the simulation runs including a tidal field and the isotropic run without the influence from a tidal field. The green line with open circles corresponds to the relative difference between the $\lambda_z = 0.1$ and the standard ($\lambda_z = 0$) while the orange line with dots represents the difference of the $\lambda_z = -0.1$ with the standard run. The black line in the lower panel gives the relative difference between the two tidal field runs. We see that there is a small difference that is most likely from higher order terms $(K_{ij})^2$ that are expected of the order of 1 percent. The solid black line in the upper panel shows the powerspectrum computed using CosmicEMU. There we see a difference at the smallest scales ($k > 2h\text{Mpc}^{-1}$) which is an effect from the limited resolution.

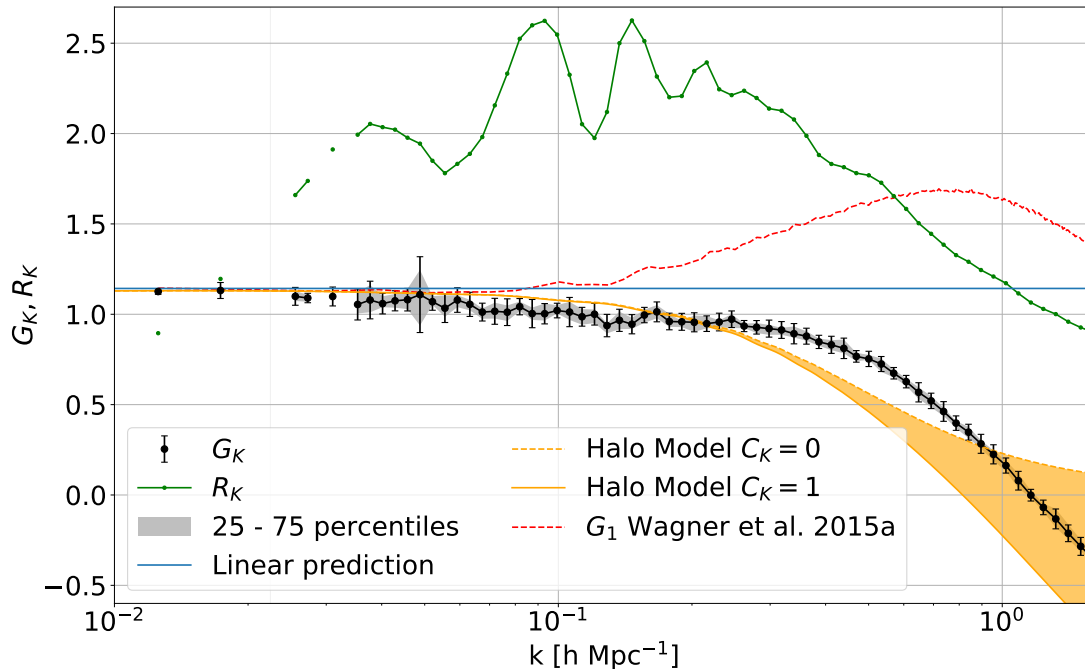


Figure 5.2: The measured growth-only (G_K) and full (R_K) tidal response from our anisotropic N-body simulations using only the PM in the force computation. The black symbols show the $z = 0$ mean of the 16 realizations for G_K , and the errorbars represent the rms scatter around the mean, where the larger errorbar around $k \sim 0.05 h \text{ Mpc}^{-1}$ is due to the substantially fewer modes compared to neighboring bins. The 25 to 75 percentiles are shown as grey band. The green line with dots shows R_K constructed via equation (2.31) from the measured G_K along with the logarithmic derivative of the power spectrum using CosmicEMU (Heitmann et al., 2016). The horizontal solid blue line shows the perturbation-theory prediction from Akitsu et al. (2017), while the red line represents the extrapolation from Barreira & Schmidt (2017a), using G_1 from Wagner et al. (2015a). Finally, the halo model prediction described in section 2.3.2 is shown as orange shaded area, where the edges show the result for $C_K = 0$ and $C_K = 1$. The decline from the linear prediction even at large scales might be a sign for higher order terms in the response approach.

On smaller scales we expect deviations from this due to nonlinear structure formation, which can be seen at $k \gtrsim 0.3 h \text{ Mpc}^{-1}$ (scales of $2\pi/k \lesssim 21 \text{ Mpc } h^{-1}$) for $z = 0$, where the response function starts to decline strongly. We also show the predictions for the extrapolated G_K in Barreira & Schmidt (2017a) which is given by $G_K = 12/13 G_1(k)$ as red line in Figure 5.2. Unlike this extrapolation, the tidal response is not enhanced on intermediate scales but rather always suppressed with respect to the large-scale limit at $a = 1$. The yellow shaded area shows the predictions of the simple halo model (section 2.3.2) depending on the choice of C_K in the range $[0, 1]$. Additionally we added the response function R_K to Figure 5.2 using the growth-only response function and the logarithmic derivative of the

power spectrum computed using CosmicEMU (Heitmann et al., 2016).

We see that the halo model describes the features of the measured response approximately. The predicted suppression in the nonlinear regime is however somewhat steeper and occurs at somewhat smaller k than seen in the N-body simulation. This is most likely a consequence of the simplistic assumptions made in the halo model, especially the assumption that all parts of the halo profile (the infall region as well as the inner core) respond equally weakly to the tidal field. Within the halo model, the key difference between G_K and the density response G_1 is that a long-wavelength tidal field does not change the number of halos (at linear order), while a long-wavelength density perturbation does.

The shift between the N-body simulation and the simple halo model suggests that the outer parts of halos as well as their environment might be affected by a large-scale tidal field. To investigate this, simulations with higher force resolution are required. Therefore we implement the TreePM scheme into GADGET4 as described in section 3.2. In fact, we will see later that the halo structure respond to the tidal field, at least through alignment of halo shapes.

Time evolution An interesting aspect of the response function is the question if it evolves with time as structure forms. For this we computed the response at different times which is shown in Figure 5.3. There appear three features. First, the decline from the linear prediction shifts to smaller k . This can be related to the scales where structure becomes nonlinear. The scale where nonlinear evolution of structure becomes important increases with time and is reflected in the point where the response function starts to deviate from the linear value of $G_K = 8/7$. Second, the large-scale value of the response seems to decline for larger redshift, which is an effect coming from the simplified initial conditions that artificially set the initial $G_K = 0$ and therefore the response appears to "grow" with time. This can be seen for example in the second bin from the left which shows a trend with redshift, even though it is well within the errorbar from the different realizations. While it does not appear obvious in the illustrated redshift range it becomes clear at even higher redshifts. The third feature is a bump at intermediate scales that declines and shifts with time, most visible in the largest redshift response shown in Figure 5.3. From the PM-only runs it is not clear whether this is a real feature or an effect from the 'wrong' velocities or other numerical effects. Therefore we can not say anything definitive about this increased response on intermediate scales that looks similar to that of the overdensity response, though not as prominent.

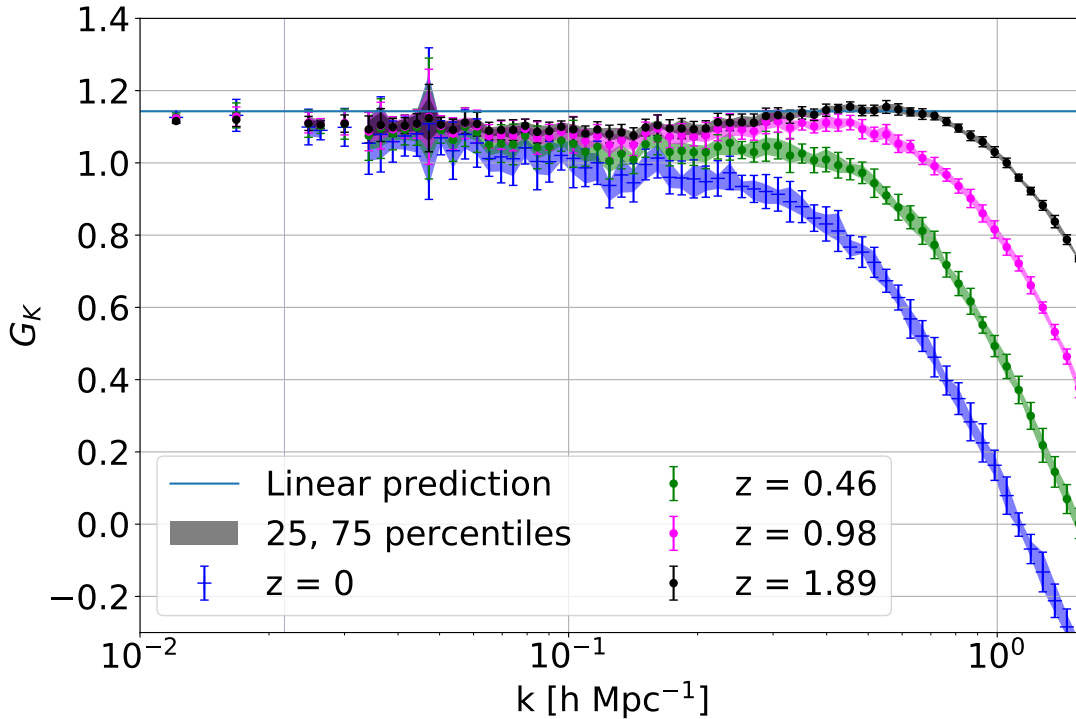


Figure 5.3: Response function for four different times computed using the PM-only simulations. Blue crosses describe the response today, while green, pink and black show the response at $z \sim 0.5$, $z \sim 1$ and $z \sim 2$ respectively. A feature that seems to appear is that at small k values (the first two bins in particular) the response seems to decline if we look further back in time. This is an effect coming from the simplified IC’s. The second effect is a small bump around $k \sim 0.7h \text{ Mpc}^{-1}$ which shifts in k and increases in amplitude while going back in time. Further the drop off from the linear prediction shifts to lower k at later times. This shows where structure formation is no longer linear and therefore the measurement deviates from the linear prediction.

5.2 TreePM simulations

Following the PM-only simulations we now turn to the TreePM runs that allow us to go to smaller scales. The main results we investigate using the TreePM simulations is the response function down to small scales up to $k \sim 20h \text{ Mpc}^{-1}$, as at higher k the decline from the “true” power spectrum becomes too large which is an effect of resolution. Further due to the higher resolution we can identify halos in the simulations and compute the shape and alignment distributions.

5.2.1 Response function

In Figure 4.2 we show the response function for the PM-only simulations over the full ranged measured which showed an upturn around $k \sim 3h \text{ Mpc}^{-1}$.

This upturn also turned up in the TreePM response function. It is introduced by shot-noise $P_{shot} \approx N_p^{-3} = 512^{-3}$ which is constant (using NGP assignment) over all k and dominates at small scales. In the numerator in equation (2.35) the shot noise cancels and it approaches zero for large k while the denominator becomes shot noise dominated at small scales. This leads to the upturn and a flattening at zero. Correcting for the shot noise in the denominator leads to a decreasing response that seem to approach the gradient of the one-dimensional power spectrum at large k for a higher resolved simulation (e.g. Millennium II simulation, $d \ln(P)/d \ln(k) \approx -2$) but then declines further as the power spectrum in our simulations is missing modes in the smaller scales which leads to an steeper decline in the one-dimensional case. For this reason we limit ourselves to k values that are smaller than $k_{limit} = 20h \text{ Mpc}^{-1}$ as described in section 4.2.2. For the TreePM simulations we use a 512^3 grid while we use power spectrum folding to increase the range in which we can measure the response function. The limit in scale is then determined by the comparison to the better resolved Millennium simulation as described before.

We show our result for the growth-only G_K and full R_K tidal response using our modified TreePM code in Figure 5.4. There we compare G_K measured from the PM-only simulations shown in grey with the eight runs using the TreePM force computation (blue). Both agree up to scales of $k < 0.7h \text{ Mpc}^{-1}$ while we see a deviation at smaller scales. This might be due to the missing shotnoise correction in the run using only the PM method for the force calculation. The response function G_K for small scales appears to approach a plateau at $G_K \sim \{-1.5; -2\}$, where the lower limit would correspond to the logarithmic slope of the one-dimensional power spectrum at the smallest scales (see e.g. the black line in Figure 5.1). This value would fit with our assumption made in the simple halo model that the tidal field does not influence the inner regions of halos. In this regime the one-halo term dominates the halo model and we expect contributions mostly from small halos and less of the inner regions of bigger halos. These might be small enough to not be affected by the tidal field which in turn would lead to an growth-only response that approaches the value of the logarithmic slope $d \ln(P)/d \ln(k)$. This in turns would mean, according to equation (2.31) (p. 31) for the full tidal response $R_K \rightarrow 0$. The black line in Figure 5.4 shows the full tidal response and we see that it does indeed approach a plateau. Nonetheless, R_K does not approach zero but rather settles at $R_K \approx 0.5$. This implies that, contrary to our assumptions in the simple halo model, there is a change for halos at small scales which was already notable in Figure 2.1 on page 26. This might be due to a change in shape or a non uniform distribution of the alignment of the halo axis, which we will discuss in more detail in section 5.2.2. We also see that at the small scales the full tidal response is constant and with a higher particle and force (smaller softening) resolution we should be able to see the asymptotic behaviour also in G_K .

Evolution One of the uncertain aspects in the PM-only runs was the apparent evolution of the response function with time. While the effect on large scales is due to the simplified initial conditions the bump on intermediate scales seemed interesting but could not be

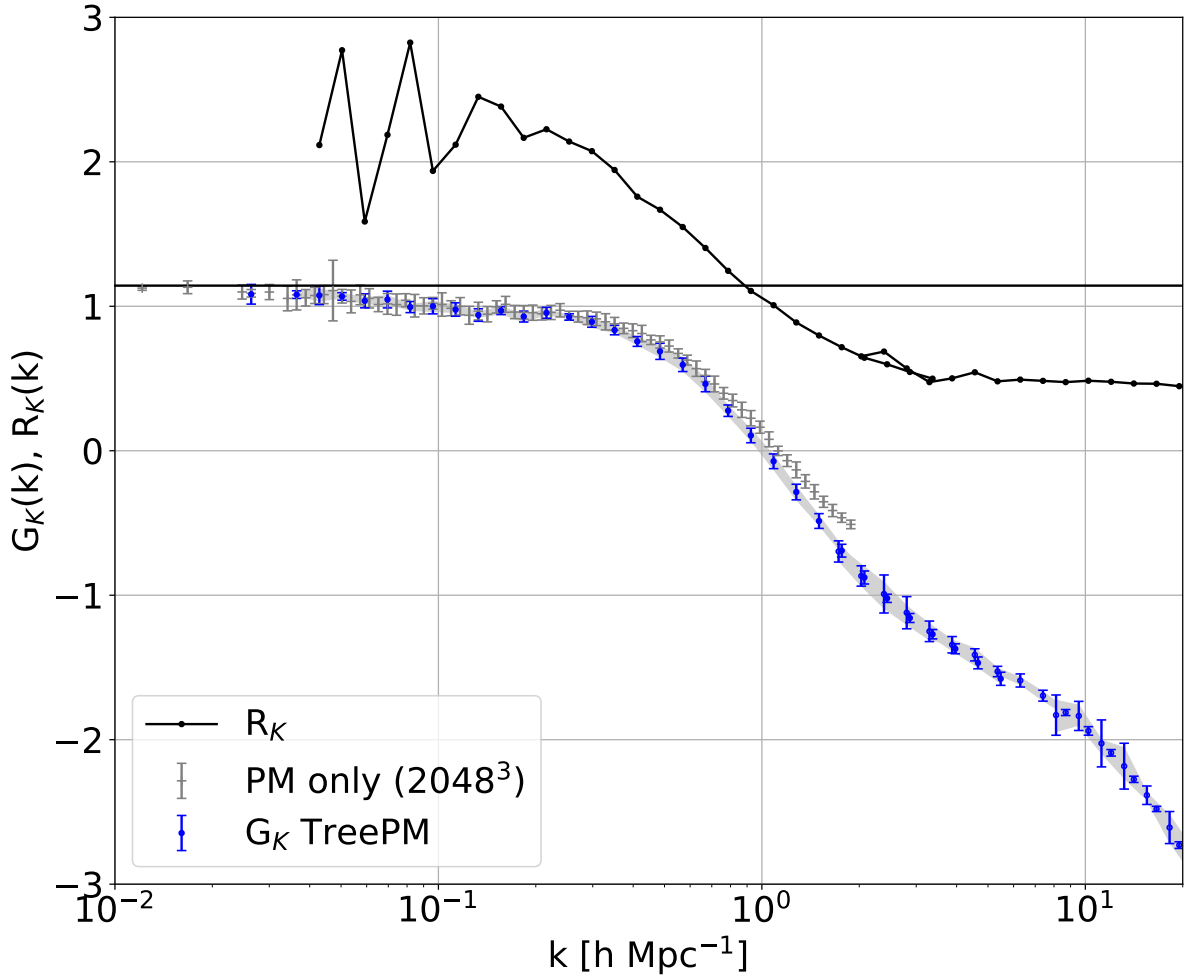


Figure 5.4: The growth-only (G_K) and full (R_K) tidal response function from our anisotropic N-Body simulations using our modified TreePM code. Here we are not interested in the full tidal response at large scales as the simulations using only the PM force calculation (grey errorbars) agrees with the full TreePM runs (blue errorbars) at scales $k < 0.7h \text{ Mpc}^{-1}$. Therefore we used less bins in the regime which seems to change the shape of R_K in comparison with Figure 5.2. The errorbars represent the standard deviation from the eight realizations, where the larger errorbar around $k \sim 0.05h \text{ Mpc}^{-1}$ is due to the substantially fewer modes compared to neighboring bins. On smaller scales the growth-only response seems to approach $G_K \approx -2$ but the curvature changes and it declines further. This is an effect coming from the decline of the power spectrum as can be seen in Figure 4.4. The full tidal response function $R_K = G_K - d \ln(P)/d \ln(k)$ shown as black line shows the same behaviour at large scale as the one measured using the PM-only runs while it flattens at small scales. From the simple halo model we expected a flattening at $R_K = 0$ as we assumed that the tidal field does not influence the structure of halos. We find that $R_K \approx 0.5$ at the small scales which hints that there is, in fact, a significant effect on halo structure.

fully trusted as it might be due to artifacts and transients. To investigate this further we compute the response function for an additional redshift $z \sim 2$, the same redshift shown as black dots in Figure 5.3. A possible explanation for the peak would be that the tidal field overall enhances the growth. Through the tidal field the first collapse of structures along one axis is faster than in the isotropic case. However after the collapse the response gets suppressed since the internal structure is (mostly) unaffected by the comparatively small large-scale tidal field. At the highest shown redshift in Figure 5.3, $z = 1.89$ the peak is at a scale of $\sim 10 \text{Mpc } h^{-1}$ ($k \sim 0.6h \text{Mpc}^{-1}$) and quite flat. In the runs including the Tree we also see a bump at a bit smaller scales ($k \sim 0.9h \text{Mpc}^{-1}$) and the bump is more pronounced (see Figure 4.5). However to trust the shape at high redshift, more tests are needed including simulations with a different initial redshift, which will show if the bump is a transient from the initial conditions or a real effect. Another possible effect that could account for this bump is discreteness due to the density field sampling using particles. This is based on the response function taken from the initial conditions at different times Figure 3.5 which hints that there could be some effect at smaller scales. The slope of the increase and the peak height is roughly equal to that seen in the initial conditions tests which hints that it might be an artifact from the limited particle number. For this we also run the smaller volumes from table 4.1 and the comparison is shown in 4.5. There the peak decreased with the higher mass and force resolution. This suggests an effect due to numerical limitations, but this test changes both the mass and force resolution. To settle this, more numerical tests (a set of different initial redshifts, higher mass and same force resolution, and higher force and same mass resolution) are needed and are not done in this thesis for lack of time.

5.2.2 Halo shapes and alignment

In the following we present the results for the halo shape and alignment measurement which is done for a single realization chosen at random from the eight runs. First we compare the subhalo mass function (Figure 5.5) between the three different runs. Here we see a bit of difference which can be traced to a few particles that link structures, but overall the mass functions agree. Calculating the inertia tensor using the single iteration starting with a sphere we arrive at a biased set of eigenvalues for the ellipsoid. Even though those are not easily related to the axes length, comparing the distribution between the three different runs with and without tidal field is still possible. Checking if the distributions for the halo shapes is different we use the cumulative distribution and perform a Kolmogorov-Smirnov (KS) test and the Anderson-Darling (AD) test (Scholz & Stephens, 1987). We do this for all halos which contain more than 100 particles which gives us around 80000 halos in each of the three different simulations for a given realization.

Further we split the sample in mass bins according to subhalo mass as shown in Figure 5.5. The mass shown here is calculated as $M_{sub} = N_{sub} \cdot m_p$ which gives us the number of particles in the subhalo, as all particles are equal in mass. Another possible mass that could be used is the virial mass of the main halo.

We only consider clusters of particles with more than 20 particles in the subgroup and 32 in the parent FoF group in our computation of the groups, which limits the low mass end of the mass function. However as described earlier we only consider the shapes and alignments for groups with more than 100 particles which is larger than the limit of SUBFIND. The halo shape and alignment angles are then measured using all particles within the virial radius defined by $\rho_{vir} = 200\rho_{mean}$.

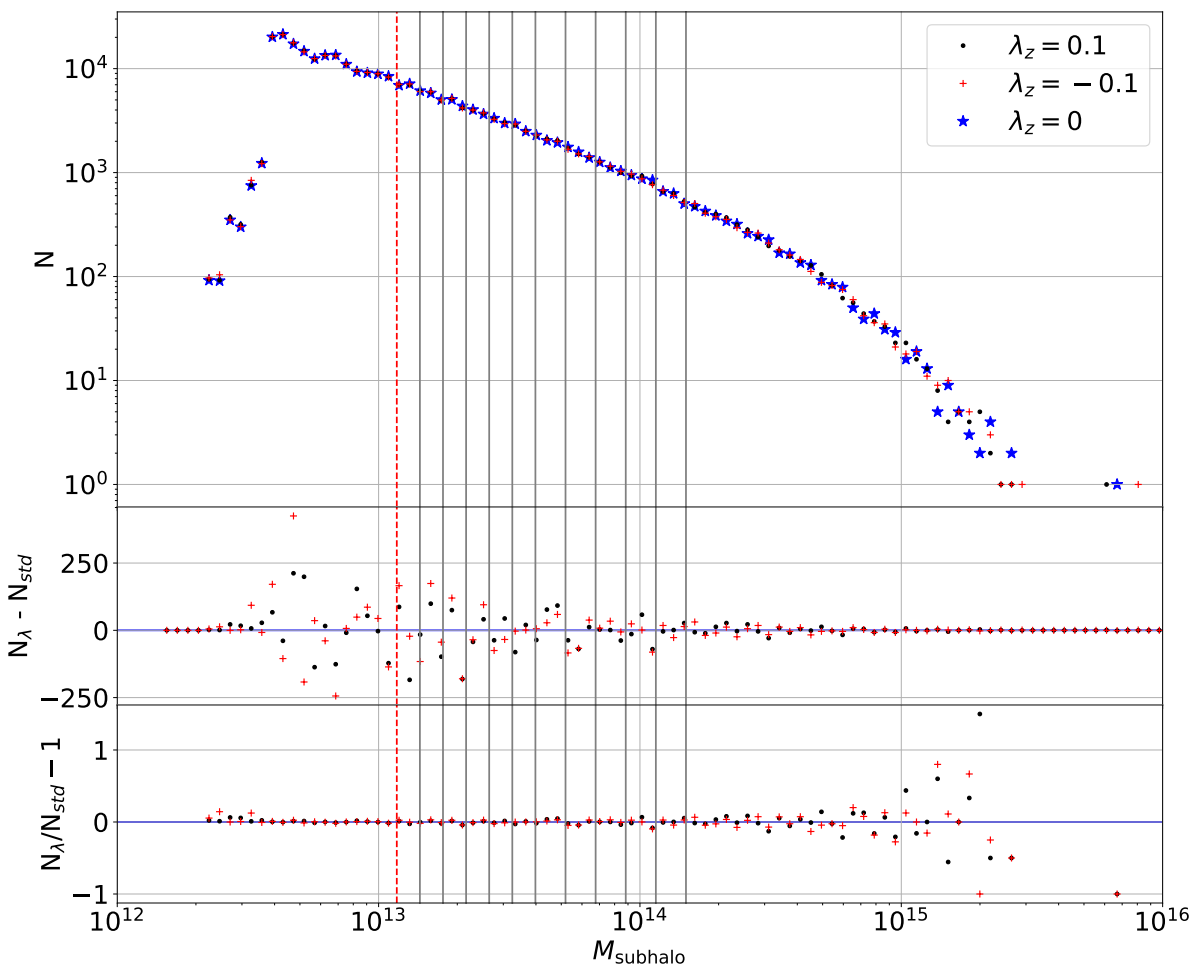


Figure 5.5: Mass function for the main subhalos, comparing the standard simulation (stars) and the runs with a tidal field (dots and crosses). The middle panel shows the difference between the ones with and without tidal field while the lower panel shows relative difference. The red crosses in the lower panels correspond to the negative z eigenvalue while the black dots to the positive eigenvalue as shown in the legend in the upper plot. The vertical lines correspond to the mass bins that are used in computing the alignment and shapes of the halos. The red dashed line corresponds to the lowest mass bin that has at least 100 particles.

From the mass function for the main subhalos we see that in the three runs with and without tidal field the subhalo distribution is roughly equal except for some scatter which can be traced to some particles that link halos and subhalos. To first order the tidal field can not change the halo number, as can be seen in the one-dimensional power spectrum (e.g. Figure 4.1) and this is what we observe here as well. The change in halo number in a given mass bin can be caused by higher order terms of the tidal field. We already see some small effects that can be attributed to higher order terms in the PM-only runs in the one-dimensional power spectrum (Figure 5.1). However the difference in halo numbers in the mass bins we see for the shape and alignment analysis is below one per cent.

The first measurements from the reduced inertia tensor are the ratios defined in equations (2.49)–(2.50) on page 36. This value contains effects from both shapes and alignments, and should be mass dependent due to the mass dependency of the shapes. In figure 5.6 we show the result of equation (2.50) for the three different diagonal elements. The value is divided by the eigenvalue of the large-scale tidal field for the given axes to normalize the value of $R_{tr} \equiv A\lambda_i$, defining the intrinsic alignment amplitude A . The result for A can be connected to a simple power law model for observations in large-scale surveys. The fitted value of the intrinsic amplitude from e.g. SDSS has a very similar value but a different sign than what we obtain from the reduced inertia tensor (e.g. Mandelbaum et al., 2006; Hirata et al., 2007). This sign change is due to the different notation for the tidal field used in this work. A stretching tidal field in our case has a negative eigenvalue while the observational definition takes that to be the largest one and therefore positive (e.g. Porciani et al., 2002). This shows qualitatively that this kind of “separate universe” simulation can be used in understanding the influence of the large-scale tidal field on the signal of intrinsic alignment that contaminates the weak lensing signal. This measurement shows a mass dependency that, as we will see, is similar to the mass dependency of the halo shape. The scatter in the different mass bins can be improved using simulations with a large volume that increases the number of halos in each mass bin. In the best case also a higher particle number should be used to increase the resolution.

Axes ratios

Using the reduced inertia tensor for each halo we can compute the eigenvalues and eigenvectors. With these eigenvalues we can estimate the principal axes in an approximate way, as we do not iterate to arrive at the “true” shape of the halo. We define the shape of the halos mainly by their ratio of the largest to smallest eigenvalue of the reduced inertia tensor, which can be interpreted as the major and minor axes, respectively. In Figure 5.7 we show all halos that have at least 100 particles associated with the subhalo. This limit corresponds to a lower mass limit of $\log(M_{\text{sub}}/M_{\odot}) = 13.07$. From the axis ratio from all halos we see that there is a small offset to higher values of c/a . To see if this effect has a mass dependency, other than the known dependency (see e.g. Schneider et al., 2012; Tenneti et al., 2015), we compute the median of the distribution for each mass bin and plot the result against the mass in Figure 5.8. The overall shape for all three runs

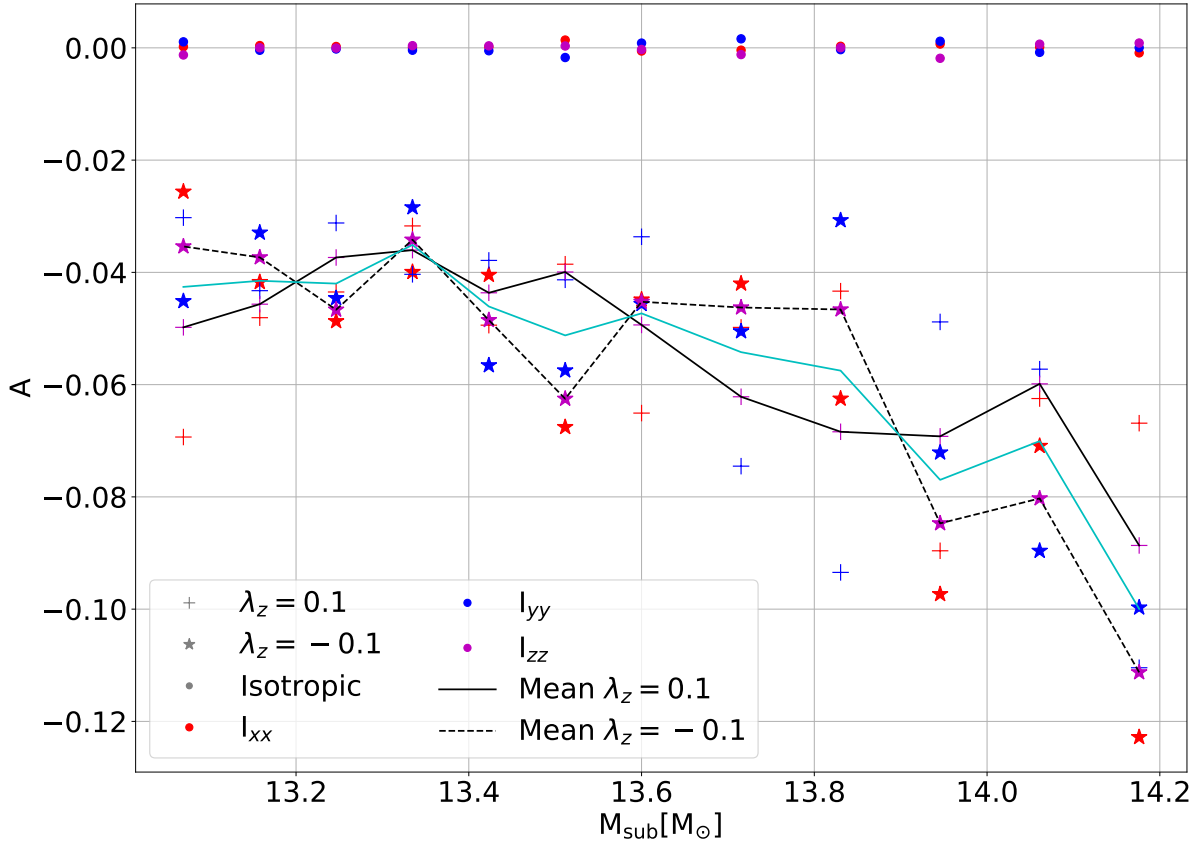


Figure 5.6: The result for the ratio of the reduced inertia tensor diagonal components normalized using the eigenvalue of the tidal field. Due to the low number of halos in each bin the scatter is rather large. The crosses show the result for the $\lambda_z = 0.1$ compressing tidal field, while the stars that for the stretching one. The different colored points that are consistent with zero are measured from the standard simulation. The three different colors show value for the different numerators of equation (2.50). Additionally the mean for both eigenvalues is shown as black line, where the solid represents that for the squeezing while the dashed line the stretching eigenvalue. The mean for both follows the value for the zz component of the reduced inertia tensor. The sign for A is explained by the different notation for the tidal field, where in our case the stretching eigenvalue is the smallest compared to the largest that is used by observers.

is identical and there is no clear difference between the runs with and without tidal field. There appears to be a minor shift towards a higher median for s in the lower mass bins. The KS and AD tests show for the smaller masses ($\log(M_{sub}[M_\odot]) \leq 13.4$) that the distributions are different as well as that at higher masses some might be different but are not conclusive. The turn over that seems to appear in Figure 5.8 is probably due to the limited particle number used for the computation of the reduced inertia tensor at the low mass end.

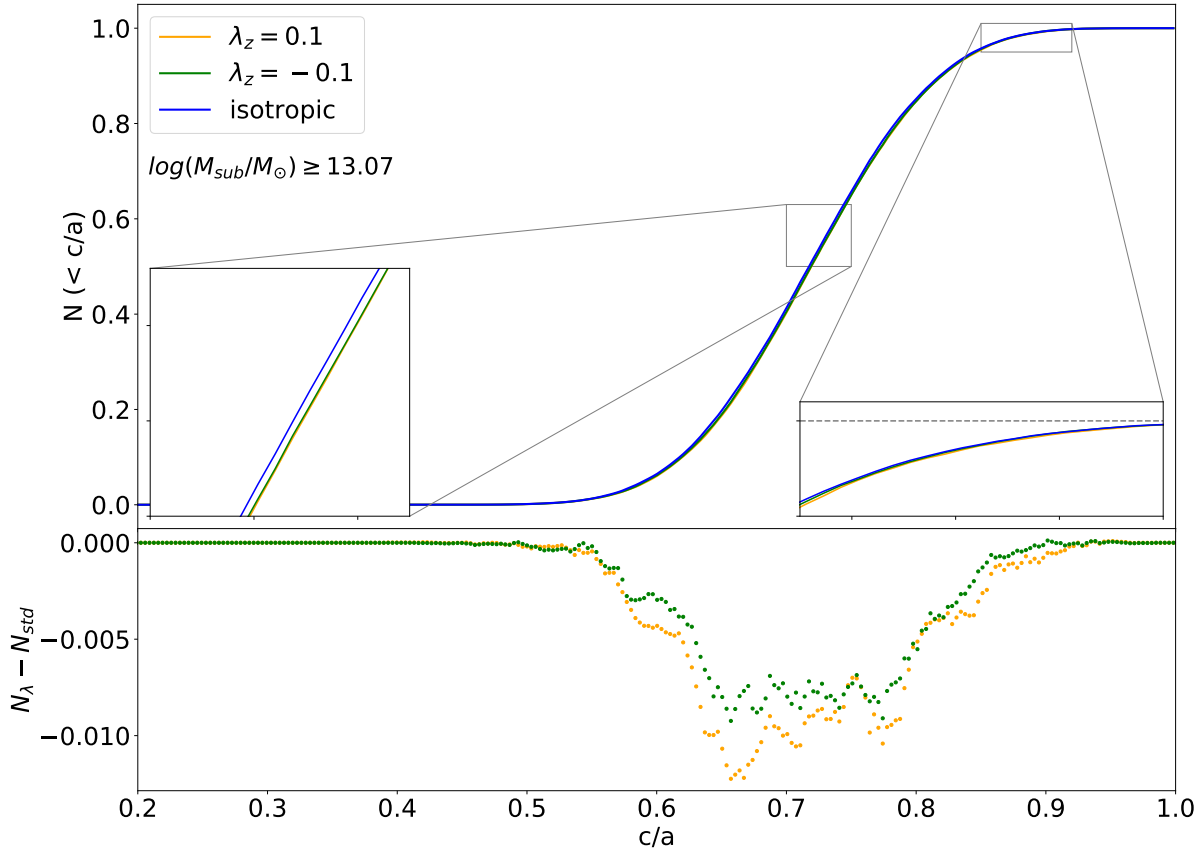


Figure 5.7: The cumulative function for the axis ratios for all main subhalos with subhalo masses $\log(M_{\text{sub}}[M_{\odot}]) \geq 13.07$ which is the lowest mass bin from Figure 3.9 is shown in the upper panel. The orange and green line represent the distribution for the case where the z-axis is compressed and stretched, respectively. The blue line represents the isotropic case. The lines for the tidal field show a small but nevertheless significant offset from that for the isotropic case. The inlays show a zoom in to the regions for $0.7 \leq c/a \leq 0.75$ and $0.85 \leq c/a \leq 0.92$ to better visualize the offset. The lower panel shows the difference between the distributions with large-scale tidal field to the one without. All halos in the standard simulation have axis ratios that are larger than $c/a = 0.4$.

Overall there seems to be a small effect on the shapes of halos from the large-scale tidal field. The more prominent feature however is the alignment with the principal axes of the tidal field that was already visible in the density image comparing a standard volume with one that is affected by a large-scale tidal field (Figure 2.1 on page 26). This will be discussed in the following.

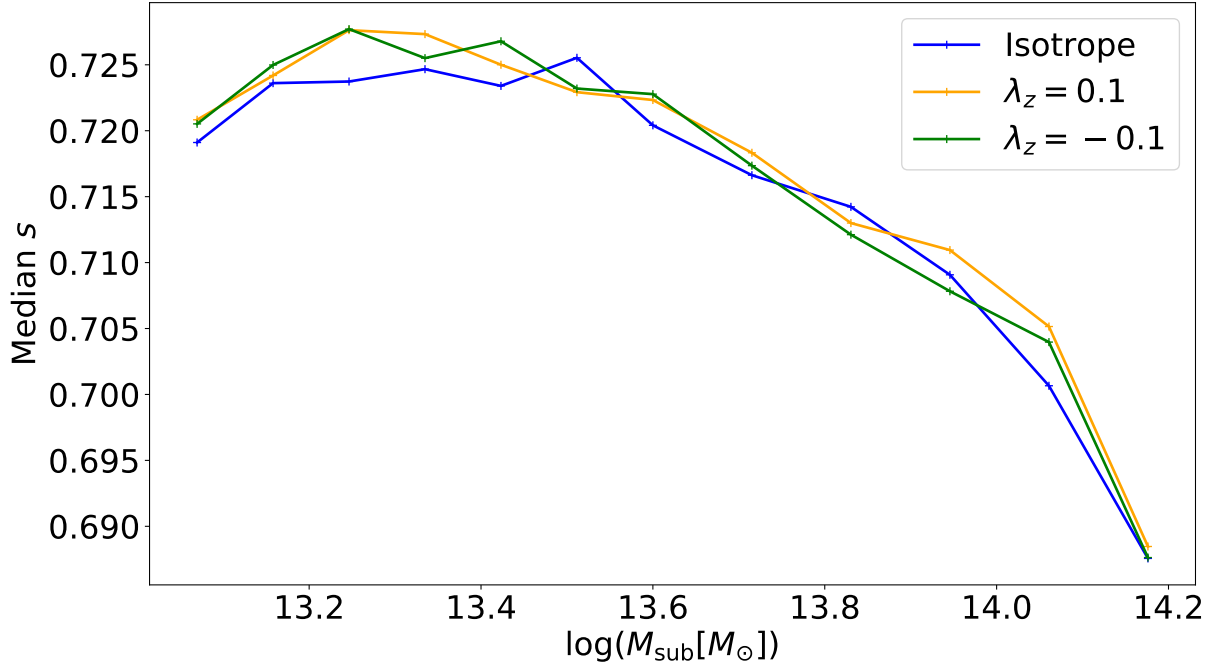


Figure 5.8: The median axis ratio for the distribution of $s = c/a$ for the twelve mass bins shown in Figure 5.5. It is not clear if the tidal effect changes the distribution or not. It appears that at low masses ($M_{\text{sub}} < 13.5M_{\odot}$) the median for the runs including a tidal field may be larger while at higher masses there seems to be no difference. However this is a minor change and should not be understood as significant evidence but only as a hint that there might be an effect. The turn over at smaller masses is most likely an effect from the limited particle number we used to compute the reduced inertia tensor.

Angle distribution

For upcoming weak lensing surveys the intrinsic alignment is an important contamination that can be further understood using simulations including large-scale tidal fields. In this section we study the difference in the distribution of the angle between the major axis of the halos and the main axis of the tidal field. In our case this is the angle between the eigenvector of the reduced inertia tensor for the major axis \hat{i}_a and the z-direction of the tidal field $\hat{t}_z = (0, 0, 1)^T$ as

$$\cos(\Theta) = \left| \frac{\hat{i}_a \cdot \hat{t}_z}{|\hat{i}_a| |\hat{t}_z|} \right| \in [0, 1]. \quad (5.1)$$

First we compute the cumulative distribution for the different mass bins, where we show a subset in Figure 5.9 (see Figure B.1 for additional mass bins). Here we see that the runs including a tidal field show a clear difference with respect to the isotropic case. Further the distributions for the two tidal fields with switched signs appear to be symmetric around the isotropic one. This can be seen further in the difference of the cumulative function

from the one-to-one relation shown in Figure B.2. To quantify this we compute the mean and median of the angle distributions for the three cases and in the twelve mass bins. The mean is shown in Figure 5.10 while the median is presented in Figure 5.11.

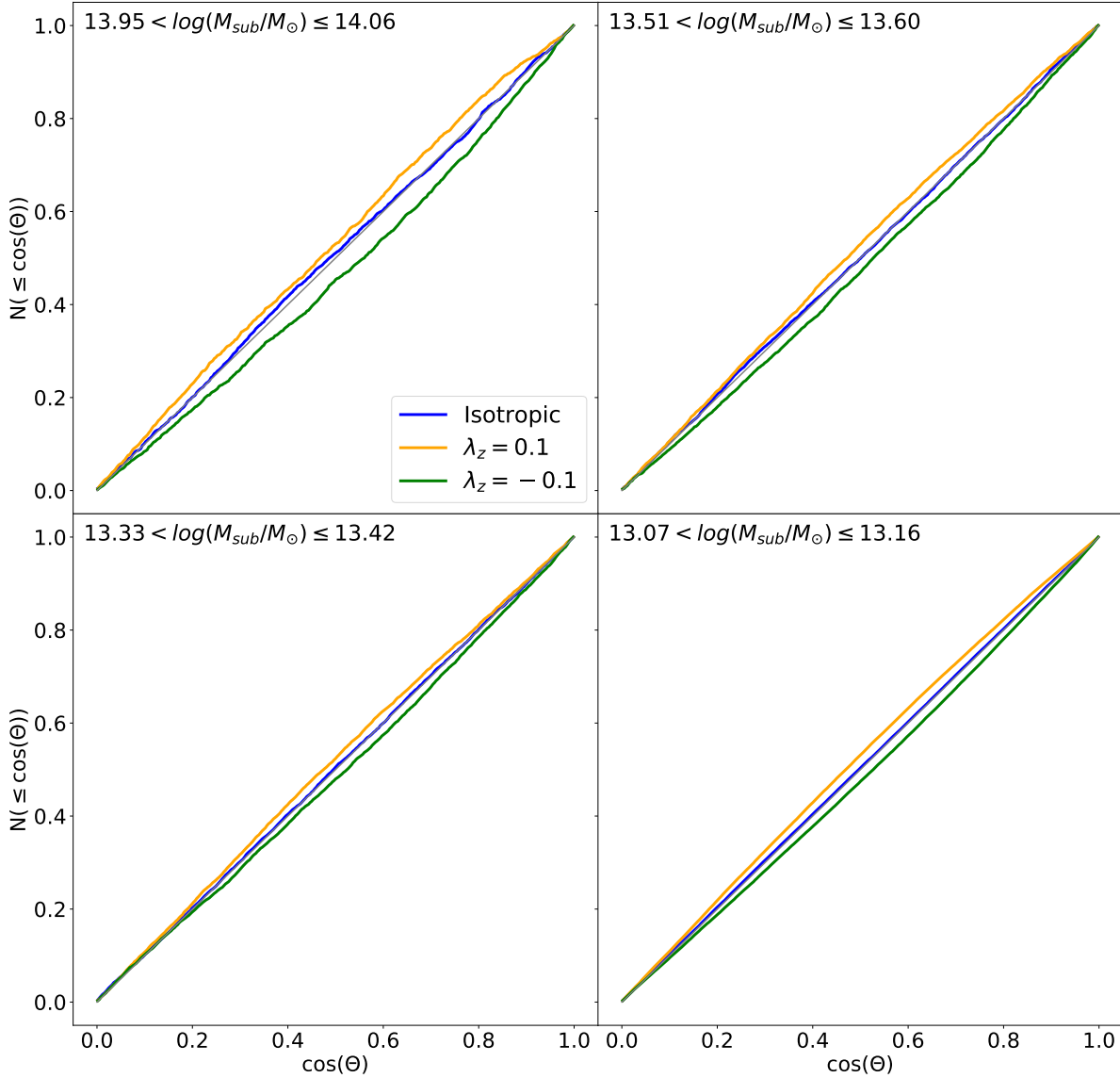


Figure 5.9: The cumulative distribution of $\cos(\Theta)$ for four mass bins. The isotropic case ($\lambda = \{0, 0, 0\}$, blue line) follows the one-to-one relation shown as black diagonal except for some noise. Here we see that the two tidal field cases (orange and green lines) show clear differences and appear symmetric around the diagonal. Six additional mass bins are shown in Figure B.1.

As expected we find that the mean for the standard simulation scatters around $\cos(\Theta) = 0.5$ with some noise.

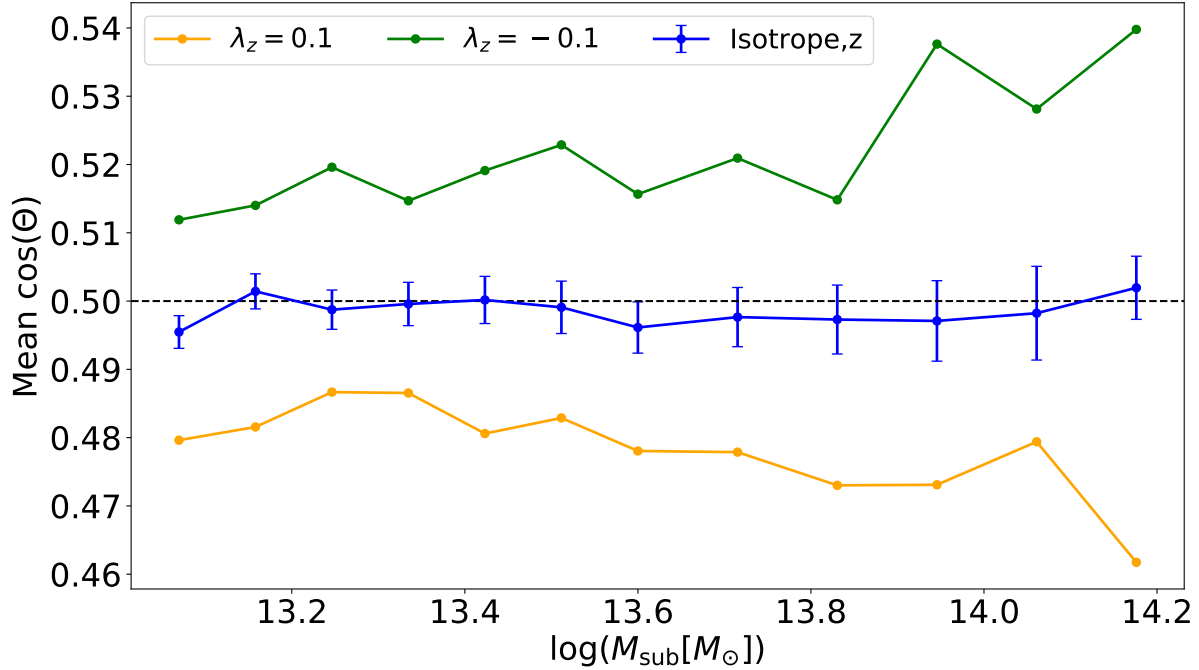


Figure 5.10: The mean for the angle $\cos(\Theta)$ in the twelve mass bins. The standard run (blue line) scatters around the value of 0.5 as expected for a random uniform distribution while the two runs including a tidal field appear symmetric around this value. The $\lambda_z = -0.1$ eigenvalue (green line), which stretches the box along the z-direction has a higher mean. The eigenvalue with the opposite sign (orange line) shows the opposite behaviour and has a smaller mean than the isotropic run. There seems to be a mass dependency in the mean for the runs with tidal field where the difference to 0.5 grows larger for higher masses. The errorbars show the 1-sigma variance of the direction cosine.

For the two runs including a large-scale tidal field we find that depending on the sign of the z eigenvalue of the tidal field we have a lower or higher mean as can be seen in Figure 5.10. We find that stretching the box in the z-direction ($\lambda_z < 0$) we find a larger mean (corresponding to halos being systematically elongated in the z-direction) while compressing along that axis reduces the mean for the cosine of the angle between the major axis of the halos and the z-direction of the tidal field. We also show 1-sigma errorbars computed as $\text{var}(\cos(\Theta)) = (12 N_{\text{halo}})^{-1}$.

This means that the large-scale tidal field leads to an alignment of structure with the axes where the volume is stretched. The effect is dependent on the strength of the tidal field as can be seen in Figure 5.11, showing the median of the distribution for all three axes. There we show the cosine of the angle between the major axis to the three axes of the tidal field. For the x and y axis the eigenvalue is half the value of the z eigenvalue and the opposite sign. This is reflected in the median of the angle between the halos and

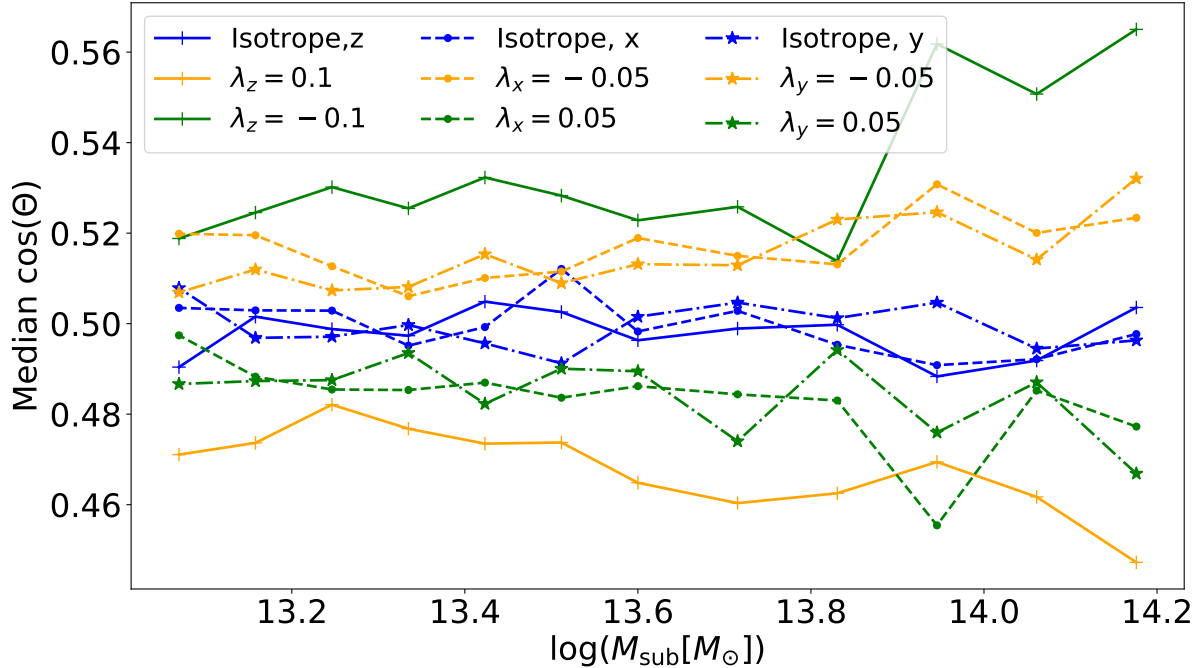


Figure 5.11: The median angle with respect to all three axes of the tidal field similar to Figure 5.10. Here we see that the effect becomes less obvious for the smaller eigenvalues as well as having the opposite direction of change in the median. The solid line shows the direction cosine with respect to the z axis, while the dashed and dash dotted lines represent the x and y axis of the tidal field, respectively. Additionally these axes also show a slight tendency for higher differences from the median expected for a uniform distribution for more massive halos.

the principal axes of the tidal field. Further we can see a mass dependency of the median where the difference from the isotropic case gets larger with higher subhalo mass.

We use the PDF from equation (2.54) on page 37 to compare to our measured angle distribution for the x-direction cosine and find a good agreement as expected. From the angle distribution we see that the alignment of the halos using all particles within the virial radius $R_{\text{vir},m}$ is influenced by the large-scale tidal field. Further the direction that is stretched by the tidal field is also the direction where halos are aligning with. This was also what we observe in Figure 2.1 on page 26.

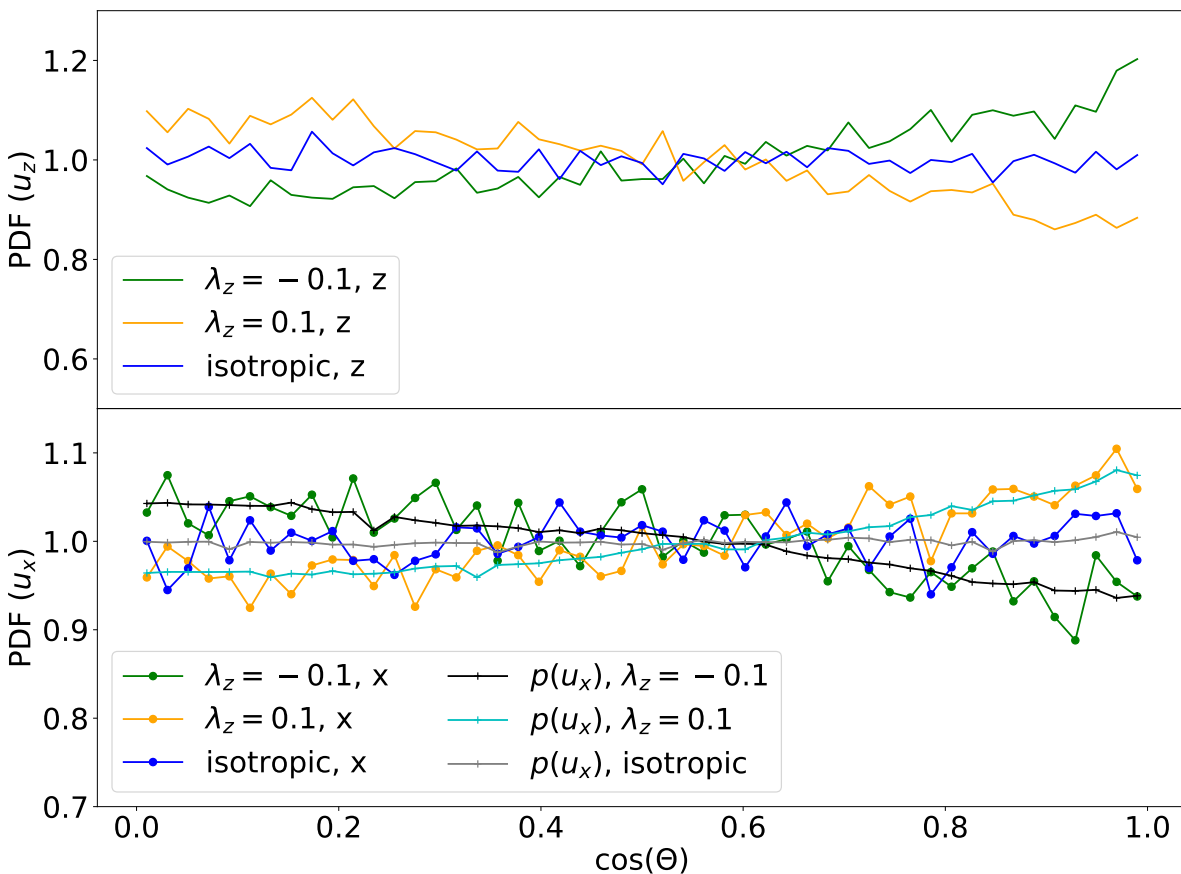


Figure 5.12: The probability density function for the cosine between the major axis of all halos with more than 100 particles and the z and x -direction of the tidal field. The top panel shows the PDF for the z -direction cosine which corresponds to the main axis of the tidal field where we see a clear signal at zero or one for $\lambda_z = 0.1$ and $\lambda_z = -0.1$, respectively. The lower panel shows the PDF for the angle with the x -direction. For both the isotropic PDF's we find them to be unity as expected. There we also show the result of equation (2.54) as black, cyan and grey line for the $\lambda_z = -0.1$, $\lambda_z = 0.1$, and isotropic case respectively. We see a very good agreement of the measured PDF to that computed from that obtained from the z -direction cosine.

Summary

In this work we have shown by numerical experiments that a large-scale tidal field has an effect on structure formation in a Λ CDM background cosmology. For this we use a modified version of GADGET4 with a PM and tree force calculation adapted to an anisotropic background metric (equation 2.15). This effect is quantified by the response function, measuring the difference of the power spectrum to that of a standard box without large scale tidal field.

As a first application, we computed the first order growth-only tidal response function G_K induced by this tidal field in the power spectrum, up to $k \simeq 2 \text{ h/cMpc}$, using runs with opposite signs for the tidal field ($\lambda_{i,1} = -\lambda_{i,2}$), and recovered the predictions from perturbation theory on large scales. Going to smaller scales, the extrapolation using the growth only response function G_1 for overdensities from Wagner et al. (2015a) does not fit our measurement of the response function. In contrast to this solution, we find a suppression of the response on small scales compared to the large-scale value, which can be described approximately by the simple halo model in section 2.3.2. However, the agreement with the simple halo model prediction is far from perfect, which is due to the fact that the model does not take into account the alignment we find for the halos. We also show the first order Eulerian response R_K in Fig. 5.2 which was computed through the sum of G_K and the logarithmic derivative of the isotropic power spectrum from CosmicEMU using the same background cosmology parameters as our simulations. This can now be used, for instance, in calculations of the covariance of the nonlinear matter and weak lensing shear power spectra.

After the first measurement of the response on large scales using the PM-only simulations we performed the same calculations using simulations run with a modified TreePM in GADGET4. This allows us to measure smaller scales as with the PM-only runs. For the smaller scales we find that, contrary to our first guess, the response does not approach the value expected from the simple halo model ($R_K \xrightarrow{k \gg 1} 0$) but asymptotically closes to $R_K \sim 0.5$. This must be, at least in parts, an effect of the alignment of halos with the large-scale tidal field.

To see the effect of the large-scale tidal field on structure, we modified the group finder which allowed us to find halos and subhalos in the simulations with the large-scale tidal field. From there we compute halo shape and the alignment angle with respect to the

largest principal axis of the tidal field for simulations with and without tidal fields to compare them to each other. We compare the semi-major axis of the halos with the z-direction of the tidal field which is the direction of the strongest effect. We find that the tidal field has a very small effect on the shapes of the halos. The overall mass dependence follows that from the isotropic case while there also seems to be a small additional effect on small subhalo masses M_{sub} (see Figure 5.8). Using all halos we find that the tidal field seems to produce slightly more halos with larger ratios of minor to major axis. Measuring the direction cosine of the major axis \hat{i}_a of halos and the principal large-scale tidal field axis \hat{t}_z on the other hand, we find a clear signal from the tidal field in the alignment angle probability density function and its cumulative distribution. From the direction cosine, measured for all particles within the virial radius we see that, if the z-direction is stretched ($\lambda_z < 0$) the halos align with this axis in eulerian/physical space. This is also reflected in the median of the $\cos \Theta$ which has a higher or lower value compared to the isotropic case for the stretching and compressing eigenvalue, respectively. Using different mass bins in subhalo mass M_{sub} we find a slight mass dependency for the distribution of cosine of the angle between the major axis of the halos and the z-direction of the tidal field as shown in Figure 5.9 and Figure 5.10.

Appendix A

TreePM Expansion Factors

A.1 Potential Expansions Factors

Using the expansion we find for the long range potential the following expression

$$\begin{aligned}
\phi_L \approx & 4\pi abc\rho_0 r_s \left[I_3 - I_5 \bar{\alpha} (\Delta\alpha_1 + \Delta\alpha_2 + \Delta\alpha_3) + I_7 \frac{\bar{\alpha}}{2r_s^2} (\Delta\alpha_1 x_1^2 + \Delta\alpha_2 x_2^2 + \Delta\alpha_3 x_3^2) \right. \\
& + \frac{\Delta\alpha_1^2}{2} \left(-I_5 + I_7 \left(3\bar{\alpha}^2 + \frac{x_1^2}{2r_s^2} \right) - I_9 \frac{3x_1^2}{r_s^2} \bar{\alpha}^2 + I_{11} \frac{x_1^4}{4r_s^4} \bar{\alpha}^2 \right) \\
& + \frac{\Delta\alpha_2^2}{2} \left(-I_5 + I_7 \left(3\bar{\alpha}^2 + \frac{x_2^2}{2r_s^2} \right) - I_9 \frac{3x_2^2}{r_s^2} \bar{\alpha}^2 + I_{11} \frac{x_2^4}{4r_s^4} \bar{\alpha}^2 \right) \\
& + \frac{\Delta\alpha_3^2}{2} \left(-I_5 + I_7 \left(3\bar{\alpha}^2 + \frac{x_3^2}{2r_s^2} \right) - I_9 \frac{3x_3^2}{r_s^2} \bar{\alpha}^2 + I_{11} \frac{x_3^4}{4r_s^4} \bar{\alpha}^2 \right) \\
& + \frac{\Delta\alpha_1 \Delta\alpha_2}{2} \left(I_7 \bar{\alpha}^2 - I_9 \bar{\alpha}^2 \left(\frac{x_1^2 + x_2^2}{2r_s^2} \right) + I_{11} \bar{\alpha}^2 \frac{x_1^2 x_2^2}{4r_s^4} \right) \\
& + \frac{\Delta\alpha_1 \Delta\alpha_3}{2} \left(I_7 \bar{\alpha}^2 - I_9 \bar{\alpha}^2 \left(\frac{x_1^2 + x_3^2}{2r_s^2} \right) + I_{11} \bar{\alpha}^2 \frac{x_1^2 x_3^2}{4r_s^4} \right) \\
& + \frac{\Delta\alpha_2 \Delta\alpha_3}{2} \left(I_7 \bar{\alpha}^2 - I_9 \bar{\alpha}^2 \left(\frac{x_2^2 + x_3^2}{2r_s^2} \right) + I_{11} \bar{\alpha}^2 \frac{x_2^2 x_3^2}{4r_s^4} \right) \\
& + \frac{\Delta\alpha_3 \Delta\alpha_2}{2} \left(I_7 \bar{\alpha}^2 - I_9 \bar{\alpha}^2 \left(\frac{x_3^2 + x_2^2}{2r_s^2} \right) + I_{11} \bar{\alpha}^2 \frac{x_3^2 x_2^2}{4r_s^4} \right) \\
& + \frac{\Delta\alpha_2 \Delta\alpha_1}{2} \left(I_7 \bar{\alpha}^2 - I_9 \bar{\alpha}^2 \left(\frac{x_2^2 + x_1^2}{2r_s^2} \right) + I_{11} \bar{\alpha}^2 \frac{x_2^2 x_1^2}{4r_s^4} \right) \\
& \left. + \frac{\Delta\alpha_3 \Delta\alpha_1}{2} \left(I_7 \bar{\alpha}^2 - I_9 \bar{\alpha}^2 \left(\frac{x_3^2 + x_1^2}{2r_s^2} \right) + I_{11} \bar{\alpha}^2 \frac{x_3^2 x_1^2}{4r_s^4} \right) \right], \tag{A.1}
\end{aligned}$$

which can be simplified by merging terms.

Appendix B

Supplementary Plots

Following are some additional plots that help clarifying some points in the main body of this thesis.

The first plot (Figure B.1) shows more cumulative distributions for the direction cosine with respect to the z-direction of the tidal field for six more mass bins. The second plot displays the difference of the cumulative function shown in Figure 5.9 against the one-to-one relation for the run with and without tidal field. This again shows a mass dependency, and a difference from the isotropic case, for the simulations which include a large-scale tidal field.

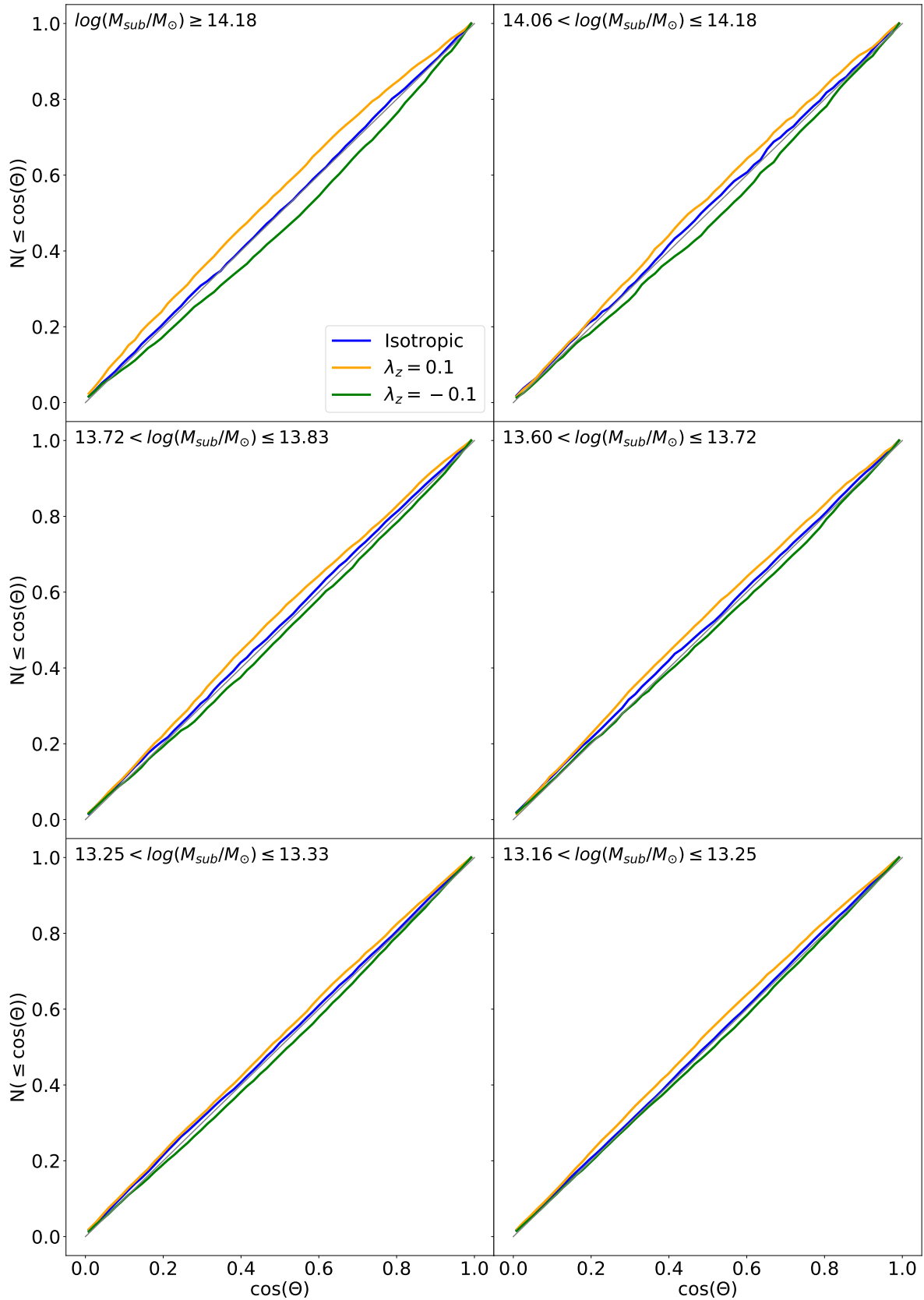


Figure B.1: Same as Figure 5.9 but for six different mass bins.

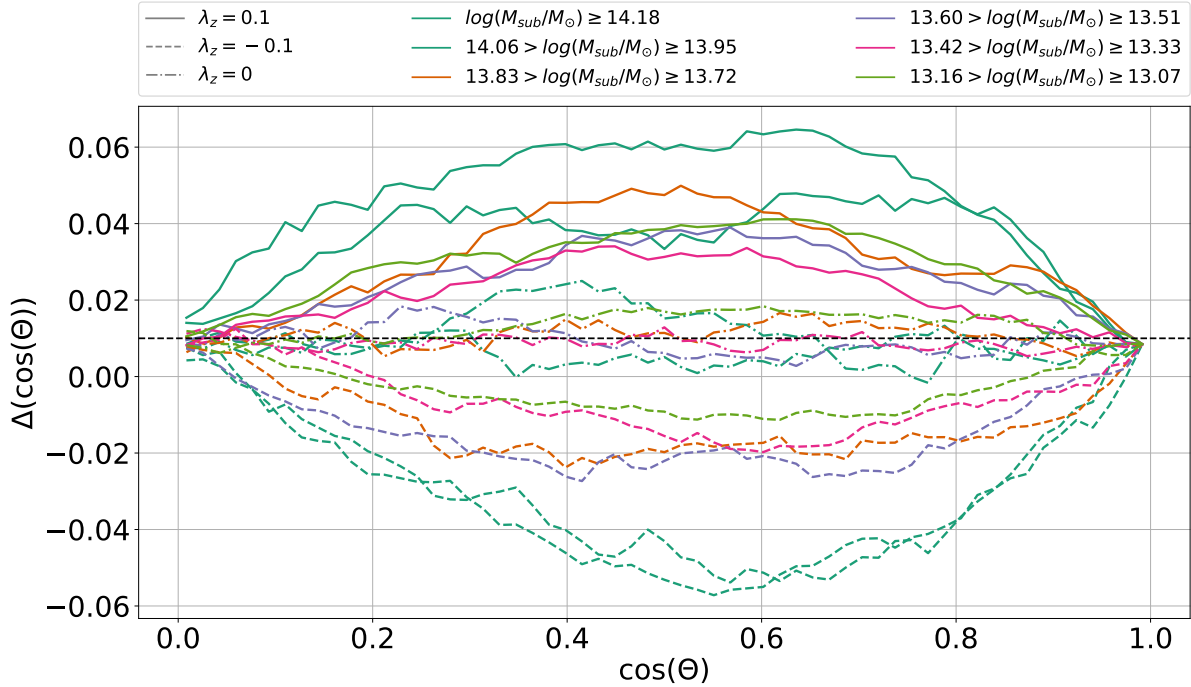


Figure B.2: The difference of the cumulative distributions of the direction cosine with respect to \hat{t}_z from the one-to-one relation measured for a subset of subhalo mass bins. We see a small offset for the standard isotropic simulation of $\Delta \cos(\Theta) \approx 0.01$, marked as black dashed line. The two runs including tidal fields have differences that appear symmetric around the isotropic value, similar as can be seen in Figure 5.9. For the stretching tidal field ($\lambda_z = -0.1$) the cosine lags behind the one-to-one relation, which translates to more halos with $\cos(\Theta)$ closer to 1.

Bibliography

- Akitsu K., Takada M., 2017, preprint, ([arXiv:1711.00012](https://arxiv.org/abs/1711.00012))
- Akitsu K., Takada M., Li Y., 2017, *Phys. Rev. D*, 95, 083522
- Bagla J. S., 2002, *Journal of Astrophysics and Astronomy*, 23, 185
- Bailin J., Steinmetz M., 2005, *ApJ*, 627, 647
- Baldauf T., Seljak U., Senatore L., Zaldarriaga M., 2011, *J. Cosmology Astropart. Phys.*, 10, 031
- Barnes J., Hut P., 1986, *Nature*, 324, 446
- Barreira A., Schmidt F., 2017a, *J. Cosmology Astropart. Phys.*, 6, 053
- Barreira A., Schmidt F., 2017b, *J. Cosmology Astropart. Phys.*, 11, 051
- Barreira A., Krause E., Schmidt F., 2017, preprint, ([arXiv:1711.07467](https://arxiv.org/abs/1711.07467))
- Baugh C., 2000, *Correlation Function and Power Spectra in Cosmology*. p. 2136, [doi:10.1888/0333750888/2136](https://doi.org/10.1888/0333750888/2136)
- Becker R. H., et al., 2001, *AJ*, 122, 2850
- Bertolini D., Solon M. P., 2016, *J. Cosmology Astropart. Phys.*, 11, 030
- Bertolini D., Schutz K., Solon M. P., Walsh J. R., Zurek K. M., 2016, *Phys. Rev. D*, 93, 123505
- Boylan-Kolchin M., Springel V., White S. D. M., Jenkins A., Lemson G., 2009, *MNRAS*, 398, 1150
- Bullock J. S., Kolatt T. S., Sigad Y., Somerville R. S., Kravtsov A. V., et al., 2001, *Mon.Not.Roy.Astron.Soc.*, 321, 559
- Byrnes C., Domènech G., Sasaki M., Takahashi T., 2016, *J. Cosmology Astropart. Phys.*, 12, 020
- Chandrasekhar S., 1969, *Ellipsoidal figures of equilibrium*

- Chiang C.-T., Wagner C., Schmidt F., Komatsu E., 2014, *J. Cosmology Astropart. Phys.*, 1405, 048
- Chiang C.-T., Li Y., Hu W., LoVerde M., 2016, *Phys. Rev. D*, 94, 123502
- Cooray A., Sheth R. K., 2002, *Phys.Rept.*, 372, 1
- Crocce M., Pueblas S., Scoccimarro R., 2006, *MNRAS*, 373, 369
- Cui W., Liu L., Yang X., Wang Y., Feng L., Springel V., 2008, *ApJ*, 687, 738
- Dai L., Pajer E., Schmidt F., 2015, *J. Cosmology Astropart. Phys.*, 10, 059
- Davis M., Efstathiou G., Frenk C. S., White S. D. M., 1985, *ApJ*, 292, 371
- Desjacques V., Jeong D., Schmidt F., 2016, *Physics Reports*
- Dubinski J., Carlberg R. G., 1991, *ApJ*, 378, 496
- Einstein A., 1915, *Sitzungsberichte der Königlich Preußischen Akademie der Wissenschaften (Berlin)*, Seite 844-847.,
- Einstein A., 1917, *Sitzungsberichte der Königlich Preußischen Akademie der Wissenschaften (Berlin)*, Seite 142-152.,
- Einstein A., de Sitter W., 1932, *Proceedings of the National Academy of Science*, 18, 213
- Eisenstein D. J., et al., 2005, *ApJ*, 633, 560
- Feeney S. M., Mortlock D. J., Dalmasso N., 2018, *MNRAS*, 476, 3861
- Frenk C. S., White S. D. M., Davis M., Efstathiou G., 1988, *ApJ*, 327, 507
- Friedmann A., 1922, *Zeitschrift fur Physik*, 10, 377
- Friedmann A., 1924, *Zeitschrift fur Physik*, 21, 326
- Gao L., Navarro J. F., Frenk C. S., Jenkins A., Springel V., White S. D. M., 2012, *MNRAS*, 425, 2169
- Gnedin N. Y., Kravtsov A. V., Rudd D. H., 2011, *ApJS*, 194, 46
- Heitmann K., et al., 2016, *ApJ*, 820, 108
- Hirata C. M., Mandelbaum R., Ishak M., Seljak U., Nichol R., Pimbblet K. A., Ross N. P., Wake D., 2007, *MNRAS*, 381, 1197
- Hockney R. W., Eastwood J. W., 1981, *Computer Simulation Using Particles*
- Hopkins P. F., Bahcall N. A., Bode P., 2005, *ApJ*, 618, 1

- Hu W., Chiang C.-T., Li Y., LoVerde M., 2016, *Phys. Rev. D*, 94, 023002
- Hubble E., 1929, *Proceedings of the National Academy of Science*, 15, 168
- Ip H. Y., Schmidt F., 2017, *J. Cosmology Astropart. Phys.*, 2, 025
- Jenkins A., 2010, *MNRAS*, 403, 1859
- Jeong D., Kamionkowski M., 2012, *Physical Review Letters*, 108, 251301
- Knebe A., et al., 2011, *MNRAS*, 415, 2293
- Lemaître G., 1927, *Annales de la Société Scientifique de Bruxelles*, 47, 49
- Lewis A., Bridle S., 2002, *Phys. Rev.*, D66, 103511
- Li Y., Hu W., Takada M., 2014, *Phys. Rev. D*, 89, 083519
- Li Y., Schmittfull M., Seljak U., 2017, preprint, ([arXiv:1711.00018](https://arxiv.org/abs/1711.00018))
- Mandelbaum R., Hirata C. M., Ishak M., Seljak U., Brinkmann J., 2006, *MNRAS*, 367, 611
- Martino M. C., Sheth R. K., 2009, *MNRAS*, 394, 2109
- McDonald P., 2003, *ApJ*, 585, 34
- McDonald P., Roy A., 2009, *J. Cosmology Astropart. Phys.*, 8, 20
- Mirbabayi M., Schmidt F., Zaldarriaga M., 2015, *J. Cosmology Astropart. Phys.*, 7, 030
- Mohammed I., Seljak U., Vlah Z., 2017, *MNRAS*, 466, 780
- Mörtsell E., Dhawan S., 2018, preprint, ([arXiv:1801.07260](https://arxiv.org/abs/1801.07260))
- Navarro J. F., Frenk C. S., White S. D. M., 1996, *ApJ*, 462, 563
- Navarro J. F., Frenk C. S., White S. D. M., 1997, *Astrophys. J.*, 490, 493
- Newton I., 1687, *Philosophiae Naturalis Principia Mathematica*. Auctore Js. Newton, doi:10.3931/e-rara-440.
- Peebles P. J. E., 1980, *The large-scale structure of the universe*
- Perlmutter S., Schmidt B. P., 2003, in Weiler K., ed., *Lecture Notes in Physics*, Berlin Springer Verlag Vol. 598, *Supernovae and Gamma-Ray Bursters*. pp 195–217 ([arXiv:astro-ph/0303428](https://arxiv.org/abs/astro-ph/0303428)), doi:10.1007/3-540-45863-8_11
- Perlmutter S., et al., 1999, *ApJ*, 517, 565

- Phillips M. M., 1993, *ApJ*, 413, L105
- Planck Collaboration et al., 2015, preprint, ([arXiv:1502.01589](https://arxiv.org/abs/1502.01589))
- Planck Collaboration et al., 2016, *A&A*, 594, A11
- Porciani C., Dekel A., Hoffman Y., 2002, *MNRAS*, 332, 339
- Pskovskii I. P., 1977, *Soviet Ast.*, 21, 675
- Riess A. G., et al., 1998, *AJ*, 116, 1009
- Riess A. G., et al., 2016, *ApJ*, 826, 56
- Rokhlin V., 1985, *J. Computational Physics*, 60, 187
- Salmon J. K., Warren M. S., 1994, *The International Journal of Supercomputer Applications and High Performance Computing*, 8, 129
- Schaye J., et al., 2015, *MNRAS*, 446, 521
- Schmidt M., 1959, *ApJ*, 129, 243
- Schmidt A. S., White S. D. M., Schmidt F., Stücker J., 2018, *MNRAS*, 479, 162
- Schneider M. D., Frenk C. S., Cole S., 2012, *J. Cosmology Astropart. Phys.*, 5, 030
- Scholz F. W., Stephens M. A., 1987, *Journal of the American Statistical Association*, 82, 918
- Sheth R. K., Tormen G., 1999, *Mon.Not.Roy.Astron.Soc.*, 308, 119
- Sirko E., 2005, *Astrophys.J.*, 634, 728
- Springel V., 2005, *MNRAS*, 364, 1105
- Springel V., White S. D. M., Tormen G., Kauffmann G., 2001, *MNRAS*, 328, 726
- Springel V., Di Matteo T., Hernquist L., 2005a, *MNRAS*, 361, 776
- Springel V., et al., 2005b, *Nature*, 435, 629
- Stücker J., Busch P., White S. D. M., 2018, *MNRAS*, 477, 3230
- Takada M., Hu W., 2013, *Phys.Rev.*, D87, 123504
- Tenneti A., Singh S., Mandelbaum R., di Matteo T., Feng Y., Khandai N., 2015, *MNRAS*, 448, 3522
- Vogelsberger M., et al., 2014, *MNRAS*, 444, 1518

Wagner C., Schmidt F., Chiang C.-T., Komatsu E., 2015a, *J. Cosmology Astropart. Phys.*, 8, 042

Wagner C., Schmidt F., Chiang C.-T., Komatsu E., 2015b, *Mon.Not.Roy.Astron.Soc.*, 448, 11

Warren M. S., Quinn P. J., Salmon J. K., Zurek W. H., 1992, *ApJ*, 399, 405

Zel'dovich Y. B., 1970, *A&A*, 5, 84

Zwicky F., 1933, *Helvetica Physica Acta*, 6, 110

Zwicky F., 1937, *ApJ*, 86, 217

Acknowledgments

First and foremost I want to thank Simon White for the possibility to work on this topic. His knowledge in the field helped me to overcome problems that had arisen during this work.

Further I want to thank the additional members of my PhD committee - Eiichiro Komatsu, Thorsten Naab and Fabian Schmidt - for their guidance and helpful advice.

I'm extremely grateful to Jens Stücker for his continued help and support throughout this work which speed up the whole project. I also want to thank Andreas Weiss for help with the computer systems at MPA as well as the occasional chat about informatics, as well as the Secretaries at the institute, Maria Depner, Sonja Gründl and Cornelia Rickl.

Additional I wish to thank Ricard Ardevol, Maximilian Eisenreich, Chia-Yu Hu, Bernhard Röttgers, Ludwig Oser, Miranda Jarvis, Matteo Frigo, Philipp Busch, Jens Stücker, Anabele Pardi, Aoife Boyle, Timo Halbesma, Francesco Rizzuto, Fabian Schmidt and all my other amazing colleagues - some of whom became my friends - for interesting, entertaining and useful discussions, some of which were not directly related to my field of astrophysics.

A special thanks goes to my girlfriend who continuously supported me throughout this work. Last but not least, I thank my family, whose support allowed me to pursue an academic career.